Wave Effects in the Gravitational Lensing of Gravitational Waves from Chirping Binaries

Ryuichi Takahashi

Department of Physics, Kyoto University, Kyoto 606-8502, Japan

January 2004

Abstract

In the gravitational lensing of gravitational waves, wave optics should be used instead of geometrical optics when the wavelength λ of the gravitational waves is larger than the Schwarzschild radius of the lens mass M_L. For example, for the wave length of the gravitational waves for the space interferometer $\lambda \sim 1$ AU, the wave effects become important for a lens mass smaller than $\sim 10^8 M_\odot$. In this thesis, we discuss the wave optics in the gravitational lensing and its application to the gravitational wave observations in the near future.

The wave optics is based on the diffraction integral which is the amplification of the wave amplitude by the lensing. We studied the asymptotic expansion of the diffraction integral in powers of the wavelength λ. The first term, arising from the short wavelength limit $\lambda \to 0$, corresponds to the geometrical optics limit. The second term, being of the order of λ / M_L, is the first correction term arising from the diffraction effect. By analyzing this correction term, we find that (i) the lensing magnification μ is modified to $\mu(1+\delta)$, where δ is of the order of $(\lambda/M_L)^2$, and (ii) if the lens has cuspy (or singular) density profile at the center $\rho(r) \propto r^{-\alpha}$ $(0 < \alpha \leq 2)$, the diffracted image is formed at the lens center with the magnification $\mu \sim (\lambda/M_L)^{3-\alpha}$.

We consider the gravitational lensing of chirp signals from the coalescense of supermassive black holes at redshift $z \sim 1$ relative to the Laser Interferometer Space Antenna. For such cases, we compute how accurately we can extract the mass of the lens and the source position from the lensed signal. We consider two simple lens models: the point mass lens and the SIS (Singular Isothermal Sphere). We find that the lens mass and the source position can be determined within $\sim 0.1\% \, [(S/N)/10^3]^{-1}$ for the lens mass larger than $10^8 M_\odot$, where (S/N) is the signal to noise ratio of the unlensed chirp signals. For the SIS model, if the source position is outside the Einstein radius, only a single image exists in the geometrical optics approximation so that the lens parameters can not be determined. While in the wave optics cases we find that the lens mass can be determined for $M_L \sim 10^8 M_\odot$. For the point mass lens, one can extract the lens parameters even if the source position is far outside the Einstein radius. As a result, the lensing cross section is an order of magnitude larger than that for the usual strong lensing of light.

Contents

Abstract **iii**

1 Introduction **1**
1.1 Wave Effects in Gravitational Lensing 1
1.1.1 Double Slit 2
1.1.2 Chirp Signal 4
1.2 Application to Gravitational Wave Observations 4
1.3 Differences between the Gravitational Lensing of Gravitational Waves and Gravitational Lensing of Light 5
1.4 Organization of this thesis 6

2 Wave Optics in Gravitational Lensing **7**
2.1 Gravitational Waves Propagating through the Curved Spacetime . . 7
2.1.1 Basic equations 7
2.1.2 Kirchhoff diffraction integral 9
2.1.3 Amplification factor 11
2.1.4 Geometrical Optics Approximation 13
2.2 Amplification Factor for Various Lens Models 14
2.2.1 Point Mass Lens 14
2.2.2 Singular Isothermal Sphere 16
2.2.3 Navarro-Frenk-White lens 17
2.2.4 Binary lens 20

3 Quasi-geometrical Optics Approximation in Gravitational Lensing **25**
3.1 Effect on the Magnifications of the Images 26
3.2 Contributions from the Non-stationary Points 28
3.3 Central Cusp of the Lens 29
3.4 Results for Specific Lens Models 32
3.4.1 Point Mass Lens 32
3.4.2 Singular Isothermal Sphere 32
3.4.3 Isothermal Sphere with a Finite Core 35
3.4.4 NFW lens 36

4 Wave Effects in the Gravitational Lensing of Gravitational Waves from Chirping Binaries 39

4.1 Gravitationally Lensed Waveform and Parameter Estimation 40

  4.1.1 Gravitational Wave Measurement with LISA 40

  4.1.2 Gravitationally Lensed Signal Measured by LISA 41

  4.1.3 Parameter Extraction 43

4.2 Results 46

  4.2.1 Lensing Effects on the Signal to Noise Ratio 46

  4.2.2 Parameter Estimation for the Lens Objects 46

  4.2.3 Lensing Effects on the Estimation Errors of the Binary Parameters 53

  4.2.4 Results for Various SMBH Masses and Redshifts 53

4.3 Lensing Event Rate 53

5 Summary 57

A Path Integral Formula for the Wave Optics 61

A.1 Basic Wave Equation 61

A.2 Path Integral 62

A.3 Application to Multi-Lens System 64

B Numerical Computation for the Amplification Factor 67

B.1 Axially Symmetric Lens Model 67

B.2 Non-axially Symmetric Lens Model 68

C Asymptotic Expansion of the Amplification Factor for Non-axially Symmetric Lens Models 69

D Estimation Errors in the Geometrical Optics Limit 73

Chapter 1

Introduction

Inspirals and mergers of compact binaries are the most promising gravitational wave sources and will be detected by the ground based as well as the space based detectors in the near future (e.g. Cutler & Thorne 2002). Laser interferometers are now coming on-line or planned on broad frequency bands: for the high frequency band $10 - 10^4$ Hz, the ground based interferometers such as TAMA300, LIGO, VIRGO and GEO600 will be operated; for the low frequency band $10^{-4} - 10^{-1}$ Hz, the Laser Interferometer Space Antenna[1] (LISA) will be in operation; for the intermediate frequency band $10^{-2} - 1$ Hz, the space based interferometers such as the Decihertz Interferometer Gravitational Wave Observatory (DECIGO; Seto, Kawamura & Nakamura 2001), and Big Bang Observer[2] (BBO) are planned. For the templates of the chirp signals from coalescing compact binaries, the post-Newtonian computations of the waveforms have been done by many authors. Using the matched filter techniques with the template, we can obtain the binary parameters such as the mass and the spatial position of the source (e.g. Cutler & Flanagan 1994). The detection rate for the compact binary mergers is also estimated for the various sources such as neutron star binaries and massive black hole binaries (see Cutler & Thorne 2002 and references therein). Thus, it is important to investigate the various possibilities that alter these theoretical calculations. One of these possibilities is the gravitational lensing which affects the template (e.g. Thorne 1987), the angular resolution of the detector (Seto 2003), and the event rate (Wang, Stebbins, & Turner 1996; Varvella, Angonin, & Tourrenc 2003). We study the gravitational lensing of gravitational waves in this thesis.

1.1 Wave Effects in Gravitational Lensing

Gravitational lensing of light is a well known phenomenon in the astrophysics. If the light from distant sources pass near the massive objects, the light ray is

---

[1] See http://lisa.jpl.nasa.gov/index.html

[2] See http://universe.gsfc.nasa.gov/be/roadmap.html.

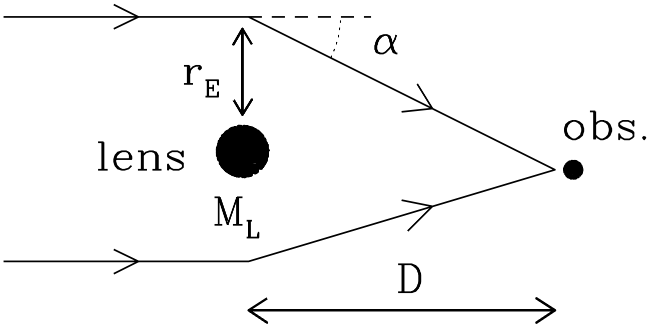

Figure 1.1: The gravitational lensing configuration. M_L is the lens mass, D is the distance to the lens, and r_E is the impact parameter.

deflected. We show the lensing configuration in Fig.1.1, the lens is located at the distance D from the observer. The deflection angle is $\alpha \sim M_L/r_E \ll 1$, where M_L is the lens mass and r_E is the impact parameter. From the deflection angle $\alpha \sim M_L/r_E$ and the geometrical relation $r_E \sim \alpha D$ in the Fig.1.1, we obtain the Einstein radius as, $r_E \sim (M_L D)^{1/2}$, which is the characteristic length of the impact parameter. The Einstein radius r_E is typically given by $r_E \sim 10$kpc $(M_L/10^{11} M_\odot)^{1/2}$, where we set $D = H_0^{-1}$ (the Hubble distance).

In the gravitational lensing of light, the lensing quantities (the deflection angle, the image positions, its brightness, the number of images, etc.) are calculated in the geometrical optics, which is valid in all observational situations (Schneider, Ehlers & Falco 1992; Nakamura & Deguchi 1999). However for the gravitational lensing of gravitational waves, the wavelength is long so that the geometrical optics approximation is not valid in some cases. For example, the wavelength λ of the gravitational waves for the space interferometer is $\sim$ 1 AU which is extremely larger than that of a visible light ($\lambda \sim 1\mu$ m).

1.1.1 Double Slit

As shown by several authors (Ohanian 1974, Bliokh & Minakov 1975, Bontz & Haugan 1981, Thorne 1983, Deguchi & Watson 1986a), if the wavelength λ is larger than the Schwarzschild radius of the lens mass M_L, the diffraction effect is important and the magnification is small. To see the reason why the ratio M_L/λ determines the significance of the diffraction, we consider a double slit with the slit width comparable to the Einstein radius $r_E \sim (M_L D)^{1/2}$ where D is the distance from the screen to the slit (Nakamura 1998). The illustration of the double slit is shown in Fig.1.2. When monochromatic waves with the wavelength λ pass through the slit, the interference pattern is produced on the screen. Denoting the

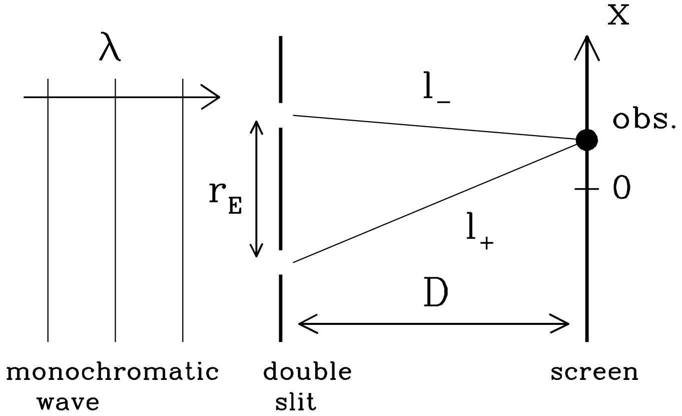

Figure 1.2: Illustration of the double slit with the slit width $r_E \sim (M_L D)^{1/2}$ (Einstein radius). λ is the wavelength of the monochromatic wave, D is the distance between the screen and the slit, and $l_\pm$ is the distance from each of the slit to the observer.

path length $l_\pm$ as the distance from each of the slit to the observer as shown in Fig.1.2, $l_\pm$ is given by,

$$l_\pm = \sqrt{(x \pm r_E/2)^2 + D^2}, \tag{1.1}$$

where x is the position of the observer on the screen. Denoting path length difference as $\Delta l \equiv |l_+ - l_-|$, we obtain from equation (1.1) as,

$$\Delta l \simeq \frac{r_E x}{D}, \tag{1.2}$$

where we assume $D \gg r_E, x$. The width Δx of the central peak of the interference pattern is obtained from equation (1.2) with setting $\Delta l \sim \lambda$ as, $\Delta x \sim (D/r_E)\lambda$. Then the maximum magnification of the wave flux is of the order $\sim r_E/\Delta x \sim M_L/\lambda$. Thus the diffraction effect is important for

$$M_L \lesssim 10^8 M_\odot \left(\frac{f}{\text{mHz}}\right)^{-1}, \tag{1.3}$$

where f is the frequency of the gravitational waves. However as suggested by Ruffa (1999), the focused region by the gravitational lensing would have a relatively large area because of the diffraction, so that the lensing probability will increase.

Since the gravitational waves from the compact binaries are coherent, the interference is also important (Mandzhos 1981, Ohanian 1983, Schneider & Schmid-Burgk 1985, Deguchi & Watson 1986b, Peterson & Falk 1991). The length of the interference pattern on the screen Δx is given by,

$$\Delta x \sim \frac{D}{r_E}\lambda,$$

$$\sim \ 0.1\mathrm{AU}\left(\frac{M_L}{10^6 M_\odot}\right)^{-1/2}\left(\frac{D}{10\mathrm{kpc}}\right)^{1/2}\left(\frac{f}{\mathrm{kHz}}\right)^{-1}. \tag{1.4}$$

Here, we assume that the lens is the suppermassive black hole of mass $M_L = 10^6 M_\odot$ at our galactic center ($D \sim 10$ kpc) and the detector is the ground-based interferometer ($f \sim$ kHz). Thus it may be possible to detect the interference pattern by the orbital motion of the earth around the Sun (Ruffa 1999).

1.1.2 Chirp Signal

We consider the inspiraling binaries as the gravitational wave sources. The inspirals of compact binaries are the most promising gravitational wave sources for the laser interferometers. As the binary system loses its energy by the gravitational radiation, the orbital separation decreases and the orbital frequency increases. Thus, the frequency of the gravitational wave increases with time ($df/dt > 0$). This is called a chirp signal. Hence we can see wave effects for different frequencies in the lensed chirp signals.

1.2 Application to Gravitational Wave Observations

The coalescence of supermassive black holes (SMBHs) of mass $10^4 - 10^7 M_\odot$ is the one of the most promising sources for LISA and will be detected with a very high signal to noise ratio $S/N \sim 10^3$ (Bender *et al.* 2000). The coalescence rate of SMBHs binaries detected by LISA is estimated to be $0.1 - 10^2$ events yr^{-1} (Haehnelt 1994,1998; Menou, Haiman, & Narayanan 2001; Jaffe & Backer 2003; Wyithe & Loeb 2003). Recently, Wyithe & Loeb (2003) suggested that the event rate was up to some hundred per year, considering the merger rate as exceedingly high redshift ($z > 5 - 10$). Since the merging SMBH events will be detected for extremely high redshift ($z > 5$), the lensing probability is relatively high (it could reach several percent, see Turner, Ostriker & Gott 1984), and hence some lensing events are expected. From the LISA frequency band ($f \sim$ mHz), the diffraction effect become important for the lens mass smaller than $\sim 10^8 M_\odot$ from equation (1.3). We will discuss the wave effects in gravitational lensing of the gravitational waves detected by LISA in §4.

Similarly, neutron star binaries are the most promising sources for the ground based interferometers (TAMA300,LIGO,VIRGO,GEO). The diffraction effect is important for the lens mass smaller than $10^3 M_\odot$ for the ground based detectors ($f \sim 10^2$ Hz). The detection rates for the neutron star mergers are at least several per year for advanced LIGO (Phinney 1991; Narayan, Piran & Shemi 1991; Kalogera *et al.* 2001,2003). But since the source redshifts are relatively small ($z < 1$) for the ground based detectors (e.g. Finn 1996), the lensing probability is small (it would be less than 0.1 percent), and hence the lensing event rate would be small (e.g. Wang, Stebbins & Turner 1996). Hence, we do not consider the gravitational lensing of gravitational waves detected by the ground based detectors.

1.3 Differences between the Gravitational Lensing of Gravitational Waves and Gravitational Lensing of Light

We discuss the differences between the gravitational lensing of gravitational waves and gravitational lensing of light. The wave effects (diffraction and interference) are some of these differences, which is discussed in the previous section. Except for the wave effects, there are some differences as follows:

- Gravitational waves propagate through surrounding matter without absorption and scattering. Hence, lens objects even in optically thick region can be detected by lensing.

- In the gravitational lensing of light, in order to detect multiple images, angular resolution θ_{min} of detector should be smaller than the image separation which is roughly equal to the Einstein angle $\theta_E = r_E/D \sim (M/D)^{1/2}$. This condition $\theta_{min} \lesssim \theta_E$ is rewritten as,

  $$M \gtrsim 10^{11} M_\odot \left(\frac{D}{\mathrm{Gpc}} \right) \left(\frac{\theta_{min}}{1\mathrm{arcsec}} \right)^2 . \tag{1.5}$$

  Thus, the lens object should be more massive than galactic mass scale. But the case of gravitational waves, the observable is time delay between the images. If the time delay $\tau \sim 10^3 \mathrm{sec}(M/10^8 M_\odot)$ is larger than than the period of the gravitational waves $1/f$, the two signals are detected. This condition $\tau \gtrsim 1/f$ is the same as the equation (1.3), and hence the lens object lighter than the galactic mass ($\sim 10^{11} M_\odot$) can be detected in the case of the gravitational waves.

- The observable for the light is the flux f of the source, while that for the gravitational waves is the amplitude A. Then, the flux is changed in proportion to the magnification μ by lensing, while the amplitude is changed in proportion to the square root $\sqrt{\mu}$.

- In the gravitational lensing of gravitational waves, the lensing cross section to extract the information on the lens object (its mass, its position, etc.) is an order of magnitude larger than that for the usual strong lensing of light (Ruffa 1999; Takahashi & Nakamura 2003).

1.4 Organization of this thesis

We outline the organization of this thesis. In §2 we review the wave optics in gravitational lensing of gravitational waves. We show the results for the various lens models: the point mass lens, the SIS model, the NFW model, and the binary lens model. In §3 we discuss the gravitational lensing in quasi-geometrical optics approximation which is the geometrical optics including corrections arising from the effects of the finite wavelength. In §4 we discuss the gravitationally lensed waveform detected by LISA and mention the parameter estimation based on the matched filtering analysis. We numerically evaluate the signal-to-noise ratio and the parameter estimation errors. We also estimate the lensing event rate. Section 5 is devoted to summary and discussions. We assume a $(\Omega_M, \Omega_\Lambda) = (0.3, 0.7)$ cosmology and a Hubble parameter $H_0 = 70 \mathrm{kms}^{-1}\mathrm{Mpc}^{-1}$ and use units of $c = G = 1$.

Chapter 2

Wave Optics in Gravitational Lensing

In this chapter, we review the wave optics in gravitational lensing of gravitational waves (Schneider, Ehlers & Falco 1992; Nakamura & Deguchi 1999). The wave optics is more fundamental than the geometrical optics, and it has been used for the gravitational lensing of gravitational waves (see Nakamura & Deguchi 1999 and reference therein).

2.1 Gravitational Waves Propagating through the Curved Spacetime

2.1.1 Basic equations

We consider gravitational waves propagating under the gravitational potential of a lens object (e.g. Misner, Thorne & Wheeler 1973). The background metric is given by,

$$ds^2 = -\left(1+2U\right)dt^2 + \left(1-2U\right)d\mathbf{r}^2 \equiv g^{(\mathrm{B})}_{\mu\nu}dx^\mu dx^\nu, \tag{2.1}$$

where $U(\mathbf{r})$ ($\ll 1$) is the gravitational potential of the lens object. Let us consider the linear perturbation $h_{\mu\nu}$ in the background metric tensor $g^{(\mathrm{B})}_{\mu\nu}$ as

$$g_{\mu\nu} = g^{(\mathrm{B})}_{\mu\nu} + h_{\mu\nu}. \tag{2.2}$$

Under the transverse traceless Lorentz gauge condition of $h^{\nu}_{\mu;\nu} = 0$ and $h^{\mu}{}_{\mu} = 0$ we have

$$h_{\mu\nu;\alpha}{}^{;\alpha} + 2R^{(\mathrm{B})}_{\alpha\mu\beta\nu}h^{\alpha\beta} = 0, \tag{2.3}$$

where the semicolon is the covariant derivative with respect to $g^{(\mathrm{B})}_{\mu\nu}$ and $R^{(\mathrm{B})}_{\alpha\mu\beta\nu}$ is the background Riemann tensor. If the wavelength λ is much smaller than the typical radius of the curvature of the background, we have

$$h_{\mu\nu;\alpha}{}^{;\alpha} = 0. \tag{2.4}$$

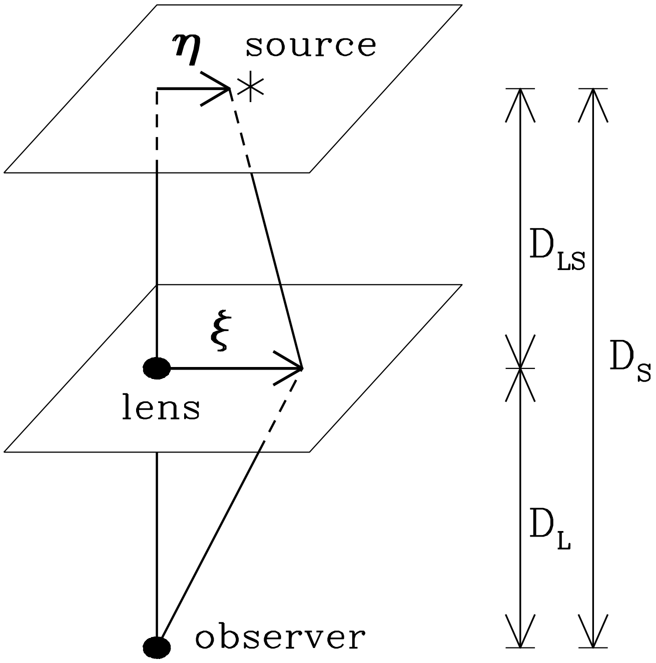

Figure 2.1: Gravitational lens geometry for the source, the lens and the observer. Here D_L, D_S and D_{LS} are the distances between them, $\boldsymbol{\eta}$ is the displacement of the source from the line of sight to the lens and $\boldsymbol{\xi}$ is an impact parameter. We use the thin lens approximation in which the gravitational waves are scattered only at the thin-lens plane.

Following the eikonal approximation to the above equation by Baraldo, Hosoya and Nakamura (1999), we express the gravitational wave as

$$h_{\mu\nu} = \phi \; e_{\mu\nu}, \tag{2.5}$$

where $e_{\mu\nu}$ is the the polarization tensor of the gravitational wave ($e^{\mu}{}_{\mu} = 0, e_{\mu\nu}e^{\mu\nu} = 2$) and ϕ is a scalar. The polarization tensor $e_{\mu\nu}$ is parallel-transported along the null geodesic ($e_{\mu\nu;\alpha}k^{\alpha} = 0$, where k^{α} is a wave vector) (Misner, Thorne & Wheeler 1973). Then, the change of the polarization tensor by gravitational lensing is of the order of U ($\ll 1$) which is very small in the present situation, and hence we can regard the polarization tensor as a constant. Thus, we treat the scalar wave ϕ, instead of the gravitational wave $h_{\mu\nu}$, propagating through the curved space-time. The propagation equation of the scalar wave is

$$\partial_{\mu}(\sqrt{-g^{(\mathrm{B})}} g^{(\mathrm{B})\mu\nu} \partial_{\nu}\phi) = 0. \tag{2.6}$$

For the scalar wave in the frequency domain $\tilde{\phi}(\omega, \mathbf{r})$, the above equation (2.6) with the metric (2.1) is rewritten as,

$$\left(\nabla^2 + \omega^2\right) \tilde{\phi} = 4\omega^2 U \tilde{\phi}. \tag{2.7}$$

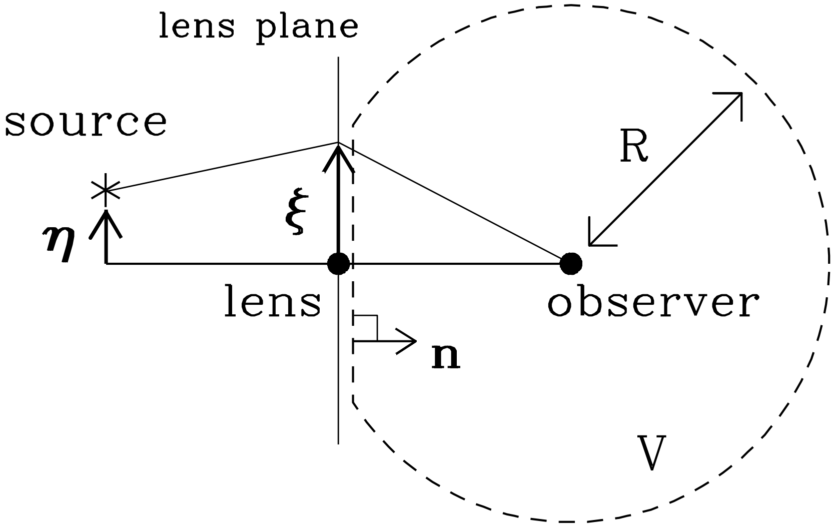

Figure 2.2: Illustration of the volume V which is inside of the dashed line. This V is enclosed with the lens plane and a sphere at the observer of radius R. Note that this V does not include the lens plane. **n** is the normal vector to the lens plane.

2.1.2 Kirchhoff diffraction integral

We derive the Kirchhoff diffraction integral in order to solve the above equation (2.7).[1] In Fig.2.1, we show the gravitational lens geometry of the source, the lens and the observer. D_L, D_S and D_{LS} are the distances to the lens, the source and from the lens to the source, respectively. $\boldsymbol{\eta}$ is a position vector of the source in the source plane while $\boldsymbol{\xi}$ is the impact parameter in the lens plane. We use the thin lens approximation in which the lens is characterized by the surface mass density $\Sigma(\boldsymbol{\xi})$ and the gravitational waves are scattered only at the thin lens plane.

We define a volume V which is inside of the dashed line in Fig.2.2. This V is enclosed by both the lens plane and sphere at the observer of radius R. Note that the boundary of V is very near the lens plane, but V does not include the lens plane (see Fig.2.2). Since we assume the thin lens approximation, $U = 0$ in V. Then the equation (2.7) is reduced to the Helmholtz equation $(\nabla^2 + \omega^2)\tilde{\phi} = 0$ in V. The Green's function for the Helmholtz equation is $e^{i\omega r}/r$ and satisfies,

$$\left(\nabla^2 + \omega^2\right) \frac{e^{i\omega r}}{r} = -4\pi\delta^3(\mathbf{r}) \tag{2.8}$$

where $\delta(\mathbf{r})$ is the delta function. With equations (2.7) and (2.8), the scalar field at

---

[1] For detailed discussions about the diffraction integral, see Born & Wolf (1997), Chapter 8.

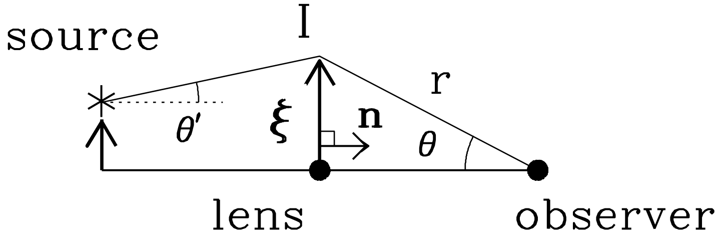

Figure 2.3: The point I is the intersection point of the ray path and the lens plane. r is the distance from I to the observer.

the observer $\tilde{\phi}^L_{obs}$ is written as,

$$\tilde{\phi}^L_{obs} = -\frac{1}{4\pi}\int_V dV \left[\tilde{\phi}\ \nabla^2 \frac{e^{i\omega r}}{r} - \frac{e^{i\omega r}}{r}\nabla^2\tilde{\phi}\right], \tag{2.9}$$

where r denotes the distance from the observer. The volume integral in the above equation is reduced to the surface integral by Green's theorem:

$$\tilde{\phi}^L_{obs} = \frac{1}{4\pi}\int_S d^2\xi \left[\tilde{\phi}\ \frac{\partial}{\partial n}\frac{e^{i\omega r}}{r} - \frac{e^{i\omega r}}{r}\frac{\partial}{\partial n}\tilde{\phi}\right], \tag{2.10}$$

where $\mathbf{n}$ is normal vector to the lens plane (see Fig.2.2). Here, we set $R \to \infty$ in Fig.2.2 and assume that $\tilde{\phi}$ and $\partial\tilde{\phi}/\partial n$ vanish at the surface of the sphere. Thus the surface integral in (2.10) is done on the lens plane.

We use the eikonal approximation to the equation (2.7) in order to obtain the field $\tilde{\phi}$ and its derivative $\partial\tilde{\phi}/\partial n$ on the boundary (the lens plane) in equation (2.10). The field is written as $\tilde{\phi} = Ae^{iS_P}$, where the amplitude A and the phase S_P satisfy the following conditions: $|\nabla A/A| \ll |\nabla S_P/S_P|$ and $|\nabla^2 S_P| \ll |\nabla S_P|^2$. Then, we have the eikonal equation from the equation (2.7): $(\nabla S_P)^2 = \omega^2(1-2U)^2$. The phase is obtained by integrating this equation along the ray path as, $S_P = \omega\int d\ell(1-2U)$. Denoting a point I which is the intersection point of the ray path and the lens plane as shown in Fig.2.3, we have the phase at I as,

$$S_P = \omega\int_{source}^{I} d\ell(1-2U) = \omega\left[\int_{source}^{obs.} d\ell - \int_{I}^{obs.} d\ell\right](1-2U). \tag{2.11}$$

Since the wave propagates along the null geodesic, we obtain $dt = d\ell(1-2U)$ from the metric (2.1). Thus, the first term of the integral in equation (2.11) is the arrival time t_d from the source to the observer. The second term is the distance r from I to the observer as shown in Fig.2.3. Then, the phase (2.11) is rewritten as,

$$S_P = \omega(t_d - r). \tag{2.12}$$

The arrival time t_d at the observer from the source position $\boldsymbol{\eta}$ through $\boldsymbol{\xi}$ is given by (Schneider, Ehlers & Falco 1992),

$$t_d(\boldsymbol{\xi},\boldsymbol{\eta}) = \frac{D_L D_S}{2D_{LS}}\left(\frac{\boldsymbol{\xi}}{D_L}-\frac{\boldsymbol{\eta}}{D_S}\right)^2 - \hat{\psi}(\boldsymbol{\xi}) + \hat{\phi}_m(\boldsymbol{\eta}), \tag{2.13}$$

where D_L, D_S and D_{LS} are the distances to the lens, the source and from the lens to the source, respectively, as shown in Fig.2.1. The first and second term in equation (2.13) is the time delay relative to the unlensed ray. The third term $\hat{\phi}_m$ is the arrival time for the unlensed ray. The deflection potential $\hat{\psi}(\boldsymbol{\xi})$ is determined by,

$$\nabla_\xi^2 \hat{\psi} = 8\pi\Sigma, \tag{2.14}$$

where ∇_ξ^2 denotes the two-dimensional Laplacian with respect to $\boldsymbol{\xi}$, and $\Sigma(\boldsymbol{\xi})$ is the surface mass density of the lens.

The derivatives in equation (2.10) are given by,

$$\frac{\partial}{\partial n}\frac{e^{i\omega r}}{r} = -i\omega\cos\theta\,\frac{e^{i\omega r}}{r}, \tag{2.15}$$

$$\frac{\partial}{\partial n}\tilde{\phi} = i\omega\cos\theta'\,\tilde{\phi}, \tag{2.16}$$

where the angles θ and θ' are shown in Fig.2.3 and $\theta, \theta' \ll 1$. Then, the lensed field at the observer $\tilde{\phi}^L_{obs}$ in equation (2.10) is finally given by,

$$\tilde{\phi}^L_{obs}(\omega,\boldsymbol{\eta}) = \frac{\omega A}{2\pi i D_L}\int d^2\xi\ \exp\left[i\omega t_d(\boldsymbol{\xi},\boldsymbol{\eta})\right], \tag{2.17}$$

where we assume $r \simeq D_L$.

We used the Kirchhoff diffraction formula to derive the lensed waveform (2.17). We discuss the path integral formula which is another method to drive the solution (2.17) in the Appendix A.

2.1.3 Amplification factor

It is convenient to define the amplification factor as

$$F(\omega,\boldsymbol{\eta}) = \frac{\tilde{\phi}^L_{obs}(\omega,\boldsymbol{\eta})}{\tilde{\phi}_{obs}(\omega,\boldsymbol{\eta})}, \tag{2.18}$$

where $\tilde{\phi}^L_{obs}$ and $\tilde{\phi}_{obs}$ are the lensed (given in equation (2.17)) and unlensed ($U = 0$ in Eq.(2.7)) gravitational wave amplitudes at the observer, respectively. Then, the amplification factor F is given by (Schneider, Ehlers & Falco 1992),

$$F(\omega,\boldsymbol{\eta}) = \frac{D_S}{D_L D_{LS}}\frac{\omega}{2\pi i}\int d^2\xi\ \exp\left[i\omega t_d(\boldsymbol{\xi},\boldsymbol{\eta})\right], \tag{2.19}$$

where F is normalized such that $|F| = 1$ in no lens limit ($U = \hat{\psi} = 0$).

Though we do not take account of the cosmological expansion in the metric, in Eq.(2.1), the results can be applied to the cosmological situation since the wavelength of the gravitational waves is much smaller than the horizon scale. What we should do is 1) take the angular diameter distances and 2) replace ω with $\omega(1+z_L)$ where z_L is the redshift of the lens (Baraldo, Hosoya and Nakamura 1999). Then, the amplification factor F in the above equation (2.19) is rewritten in the cosmological situation as,

$$F(\omega, \boldsymbol{\eta}) = \frac{D_S}{D_L D_{LS}} \frac{\omega(1+z_L)}{2\pi i} \int d^2\xi \;\; \exp\left[i\omega(1+z_L)t_d(\boldsymbol{\xi}, \boldsymbol{\eta})\right]. \tag{2.20}$$

where D_L, D_S and D_{LS} denote the angular diameter distances.

It is useful to rewrite the amplification factor F in terms of dimensionless quantities. We introduce ξ_0 as the normalization constant of the length in the lens plane. The impact parameter $\boldsymbol{\xi}$ and the source position $\boldsymbol{\eta}$ (in Fig.2.1) are rewritten in dimensionless form,

$$\mathbf{x} = \frac{\boldsymbol{\xi}}{\xi_0}; \;\; \mathbf{y} = \frac{D_L}{\xi_0 D_S}\boldsymbol{\eta}. \tag{2.21}$$

Similarly, we define dimensionless frequency w by,

$$w = \frac{D_S}{D_{LS} D_L}\xi_0^2(1+z_L)\omega. \tag{2.22}$$

Then, the dimensionless time delay is given by,

$$\begin{aligned} T(\mathbf{x}, \mathbf{y}) &= \frac{D_L D_{LS}}{D_S}\; \xi_0^{-2}\; t_d(\boldsymbol{\xi}, \boldsymbol{\eta}) && (2.23) \\ &= \frac{1}{2}\left|\mathbf{x} - \mathbf{y}\right|^2 - \psi(\mathbf{x}) + \phi_m(\mathbf{y}), && (2.24) \end{aligned}$$

where $\psi(\mathbf{x})$ and $\phi_m(\mathbf{y})$ correspond to $\hat{\psi}(\boldsymbol{\xi})$ and $\hat{\phi_m}(\boldsymbol{\eta})$ in equation (2.13): $\psi = D_L D_{LS}/(D_S \xi_0^2)\hat{\psi}$ and $\phi_m = D_L D_{LS}/(D_S \xi_0^2)\hat{\phi}_m$, respectively. We choose $\phi_m(\mathbf{y})$ so that the minimum value of the time delay is zero.[2] The dimensionless deflection potential $\psi(\mathbf{x})$ satisfies,

$$\nabla_x^2 \psi = \frac{2\Sigma}{\Sigma_{cr}}, \tag{2.25}$$

where ∇_x^2 denotes the two-dimensional Laplacian with respect to x, Σ is the surface mass density of the lens, and $\Sigma_{cr} = D_S/(4\pi D_L D_{LS})$. Using the above dimensionless quantities, the amplification factor is rewritten as,

$$F(w, \mathbf{y}) = \frac{w}{2\pi i} \int d^2x \exp\left[iwT(\mathbf{x}, \mathbf{y})\right]. \tag{2.26}$$

---

[2] $\phi_m(\mathbf{y})$ corresponds to the arrival time in the unlensed case in Eq.(2.13) originally. But, $\phi_m(\mathbf{y})$ is also the additional phase in F, which can be chosen freely (see the sentence after equation (2.19)). Hence, we choose a convenient value for later calculation.

For axially symmetric lens models, the integral of the amplification factor F in equation (2.26) becomes a relatively simple form, since the deflection potential $\psi(\mathbf{x})$ depends only on $x = |\mathbf{x}|$. F is expressed as (Nakamura & Deguchi 1999),

$$F(w, y) = -iwe^{iwy^2/2} \int_0^\infty dx \; x \; J_0(wxy) \exp\left[iw\left(\frac{1}{2}x^2 - \psi(x) + \phi_m(y)\right)\right], \quad (2.27)$$

where J_0 is the Bessel function of zeroth order. It takes a long time to calculate F numerically in equations (2.26) and (2.27), because the integrand is rapidly oscillating function especially for large w. In the Appendix B, we present a method for numerical computation to shorten the computing time.

We use the Einstein radius ($\sim \sqrt{MD}$) as a arbitrary scale length ξ_0 (except for the NFW lens), for convenience. The Einstein radius is the typical scale length of the impact parameter in gravitational lensing, and hence the dimensionless quantities $\mathbf{x}, \mathbf{y}$ become of the order of one. The dimensionless potential $\psi(\mathbf{x})$ and time delay $T(\mathbf{x}, \mathbf{y})$ are also of the order of one. Then, the dimensionless frequency is roughly $w \sim M/\lambda$ from equation (2.22).

2.1.4 Geometrical Optics Approximation

In the geometrical optics limit ($w \gg 1$), the stationary points of the $T(\mathbf{x}, \mathbf{y})$ contribute to the integral of Eq.(2.26) so that the image positions $\mathbf{x}_j$ are determined by the lens equation, $\nabla_x T(\mathbf{x}, \mathbf{y}) = 0$ or

$$\mathbf{y} = \mathbf{x} - \nabla_x \psi(\mathbf{x}). \quad (2.28)$$

This is just the Fermat's principle. We expand $T(\mathbf{x}, \mathbf{y})$ around the j-th image position $\mathbf{x}_j$ as,

$$T(\mathbf{x}, \mathbf{y}) = T(\mathbf{x}_j, \mathbf{y}) + \sum_a \partial_a T(\mathbf{x}_j, \mathbf{y})\tilde{x}_a + \frac{1}{2}\sum_{a,b} \partial_a \partial_b T(\mathbf{x}_j, \mathbf{y})\tilde{x}_a \tilde{x}_b + \mathcal{O}(\tilde{x}^3) \quad (2.29)$$

where $\tilde{\mathbf{x}} = \mathbf{x} - \mathbf{x}_j$ and the indices a,b,... run from 1 to 2. The second term in Eq.(2.29) vanishes because $\mathbf{x}_j$ is the stationary point of $T(\mathbf{x}, \mathbf{y})$. Inserting Eq.(2.29) to (2.26) with the Gaussian integral,[3] we obtain the amplification factor in geometrical optics limit as (Nakamura & Deguchi 1999),

$$F_{geo}(w, \mathbf{y}) = \sum_j |\mu_j|^{1/2} \exp\left[\, iwT_j - i\pi n_j\right], \quad (2.30)$$

where the magnification of the j-th image is $\mu_j = 1/\det(\partial \mathbf{y}/\partial \mathbf{x}_j)$, $T_j = T(\mathbf{x}_j, \mathbf{y})$ and $n_j = 0, 1/2, 1$ when $\mathbf{x}_j$ is a minimum, saddle, maximum point of $T(\mathbf{x}, \mathbf{y})$, respectively. In the time domain the lensed wave is expressed as

---

[3] $\int_{-\infty}^{\infty} dx e^{iax^2} = \sqrt{\frac{\pi}{|a|}} e^{i\pi/4 \times sign(a)}$

$$\phi^L_{geo}(t,\mathbf{r}) = \sum_j |\mu_j|^{1/2} e^{-i\pi n_j} \phi(t - t_{d,j}, \mathbf{r}), \tag{2.31}$$

where $t_{d,j}$ is the time delay of the j-th image ($t_d = D_S\xi_0^2/(D_L D_{LS}) \times T$). This shows that the oscillatory behavior of F in high frequency w is essential to obtain the time delay among the images.

2.2 Amplification Factor for Various Lens Models

In this section, we show the behavior of the amplification factor F for the various lens models. We consider the following lens models: point mass lens, singular isothermal sphere (SIS) lens, Navarro Frenk White (NFW) lens, and binary lens.

2.2.1 Point Mass Lens

The surface mass density is expressed as $\Sigma(\boldsymbol{\xi}) = M_L\delta^2(\boldsymbol{\xi})$ where M_L is the lens mass. As the normalization constant ξ_0 we adopt the Einstein radius given by $\xi_0 = (4M_L D_L D_{LS}/D_S)^{1/2}$ while the dimensionless deflection potential is given as $\psi(\mathbf{x}) = \ln x$. In this case, Eq.(2.27) is analytically integrated as (Peters 1974),

$$\begin{aligned} F(w,y) &= \exp\left[\frac{\pi w}{4} + i\frac{w}{2}\left\{\ln\left(\frac{w}{2}\right) - 2\phi_m(y)\right\}\right] \\ &\quad \times \Gamma\left(1 - \frac{i}{2}w\right) {}_1F_1\left(\frac{i}{2}w, 1; \frac{i}{2}wy^2\right), \end{aligned} \tag{2.32}$$

where $w = 4M_{Lz}\omega$; $\phi_m(y) = (x_m - y)^2/2 - \ln x_m$ with $x_m = (y + \sqrt{y^2+4})/2$; $M_{Lz} = M_L(1+z_L)$ is the redshifted lens mass and ${}_1F_1$ is the confluent hypergeometric function. Thus, the amplification factor F depends on two parameters; the (dimensionless) frequency w and the source position y. In the geometrical optics limit ($w \gg 1$) from equation (2.30) we have

$$F_{geo}(w,y) = |\mu_+|^{1/2} - i\,|\mu_-|^{1/2} e^{iw\Delta T}, \tag{2.33}$$

where the magnification of each image is $\mu_\pm = 1/2 \pm (y^2+2)/(2y\sqrt{y^2+4})$ and the time delay between the double images is $\Delta T = y\sqrt{y^2+4}/2 + \ln((\sqrt{y^2+4}+y)/(\sqrt{y^2+4}-y))$. The time delay is typically $\Delta t_d = 4M_{Lz} \times \Delta T = 2 \times 10^3$ sec $\times (M_{Lz}/10^8 M_\odot)$.

The point mass lens model has been used for lensing by compact objects such as black holes or stars. Even for the extended lens, this model can be used if the lens size is much smaller than the Einstein radius, because of Birkhoff's theorem.

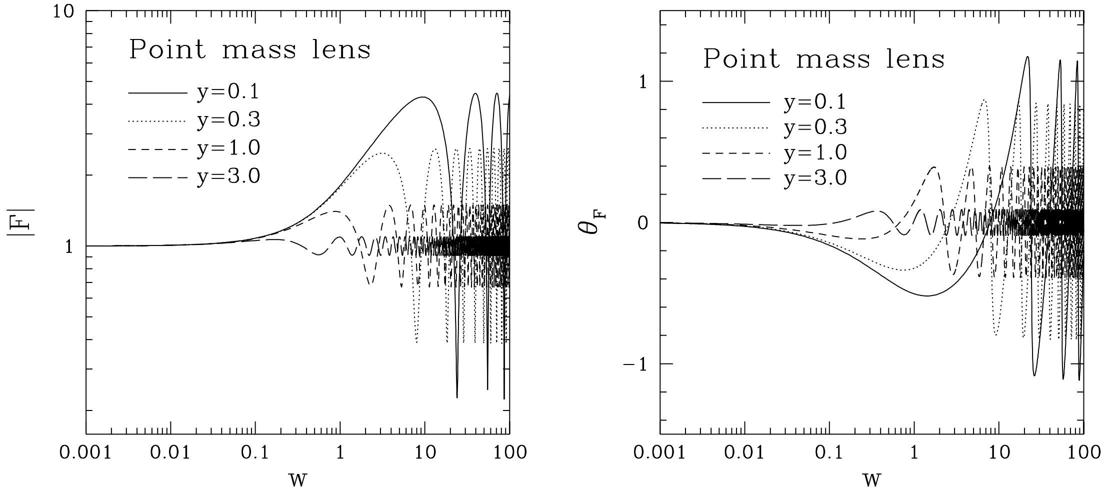

Figure 2.4: The amplification factor $|F|$ (left) and the phase $\theta_F = -i \ln[F/|F|]$ (right) for point mass lens as a function of w with the fixed source position $y = 0.1, 0.3, 1$ and 3. For $w \lesssim 1$, the amplification is very small due to the diffraction effect. For $w \gtrsim 1$, the oscillatory behavior appears due to the interference between the double images.

Hence, this model is most frequently used in wave optics in gravitational lensing of gravitational waves (Nakamura 1998; Ruffa 1999; De Paolis *et al.* 2001,2002; Zakharov & Baryshev 2002; Takahashi & Nakamura 2003). As far as we know, the analytical solution of F in Eq.(2.26) is known only for this model.

In the left panel of Fig.2.4, the amplification factor $|F|$ for the point mass lens is shown as a function of w with a fixed source position $y = 0.1, 0.3, 1$ and 3. For $w \lesssim 1$, the amplification is very small due to the diffraction effect (e.g., Bontz & Haugan 1980). Since in this case the wave length is so long that the wave does not feel the existence of the lens. For $w \gtrsim 1$, $|F|$ asymptotically converges to the geometrical optics limit (Eq.(2.33)),

$$|F_{geo}|^2 = |\mu_+| + |\mu_-| + 2\,|\mu_+\mu_-|^{1/2} \sin(w\Delta T). \tag{2.34}$$

The first and second terms in Eq.(2.34), $|\mu| = |\mu_+| + |\mu_-|$, represent the total magnification in the geometrical optics. The third term represents the interference between the double images. The oscillatory behavior (in Fig.2.4) is due to this interference. The amplitude and the period of this oscillation are approximately equal to $2|\mu_+\mu_-|^{1/2}$ and $w\Delta T$ in the third term of Eq.(2.34), respectively. As the source position y increases, the total magnification $|\mu|$ $(= |\mu_+| + |\mu_-|)$ and the amplitude of the oscillation $2|\mu_+\mu_-|^{1/2}$ decrease. This is because each magnification $|\mu_\pm(y)|$ decreases as y increases.

The right panel of Fig.2.4 is the same as the left panel, but we show the phase of the amplification factor $\theta_F = -i\ln[F/|F|]$. The behavior is similar to that of the amplitude (in left panel), and the wave effects appear in the phase θ_F as well as the amplitude $|F|$. For $w \gtrsim 1$, θ_F asymptotically converges to the geometrical optics limit (Eq.(2.33)),

$$\theta_F = \arctan\left[\frac{-|\mu_-|^{1/2}\cos(w\Delta T)}{|\mu_+|^{1/2} + |\mu_-|^{1/2}\sin(w\Delta T)}\right], \tag{2.35}$$

From the above equation (2.35), the phase θ_F oscillates between $-\arctan(|\mu_-/\mu_+|^{1/2})$ and $\arctan(|\mu_-/\mu_+|^{1/2})$ with the period of $w\Delta T$. As the source position y increases, the magnification ratio $|\mu_-/\mu_+|$ and the amplitude of the oscillation $\arctan(|\mu_-/\mu_+|^{1/2})$ decrease.

2.2.2 Singular Isothermal Sphere

The surface density of the SIS (Singular Isothermal Sphere) is characterized by the velocity dispersion v as, $\Sigma(\boldsymbol{\xi}) = v^2/(2\xi)$. As the normalization constant we adopt the Einstein radius $\xi_0 = 4\pi v^2 D_L D_{LS}/D_S$ and the dimensionless deflection potential is $\psi(\mathbf{x}) = x$. In this case F in Eq.(2.27) is expressed as,

$$F(w,y) = -iwe^{iwy^2/2}\int_0^\infty dx\ x\ J_0(wxy)\exp\left[iw\left(\frac{1}{2}x^2 - x + \phi_m(y)\right)\right], \tag{2.36}$$

where J_0 is the Bessel function of zeroth order; $\phi_m(y) = y + 1/2$ and $w = 4M_{Lz}\omega$ where M_{Lz} is defined as the mass inside the Einstein radius given by $M_{Lz} = 4\pi^2 v^4(1+z_L)D_L D_{LS}/D_S$. Then, F depends on the two parameters w and y. We computed the above integral numerically for various parameters. In the geometrical optics limit ($w \gg 1$), F is given by,

$$\begin{aligned} F_{geo}(w,y) &= |\mu_+|^{1/2} - i\,|\mu_-|^{1/2}\,e^{iw\Delta T} && \text{for } y < 1, \\ &= |\mu_+|^{1/2} && \text{for } y \geq 1, \end{aligned} \tag{2.37}$$

where $\mu_\pm = \pm 1 + 1/y$ and $\Delta T = 2y$. For $y < 1$ double images are formed, while for $y \geq 1$ single image is formed.

The SIS model is used for more realistic lens objects than the point mass lens, such as galaxies, star clusters and dark halos (Takahashi & Nakamura 2003).

Fig.2.5 is the same as Fig.2.4, but for the SIS lens. The behavior is similar to that for the point mass lens. In the left panel, for $w \gtrsim 1$, $|F|$ asymptotically converges to the geometrical optics limit (Eq.(2.37)),

$$\begin{aligned} |F_{geo}|^2 &= |\mu_+| + |\mu_-| + 2\,|\mu_+\mu_-|^{1/2}\sin(w\Delta T) && \text{for } y < 1, \\ &= |\mu_+| && \text{for } y \geq 1. \end{aligned} \tag{2.38}$$

For $y < 1$, the oscillatory behavior in the left panel of Fig.2.5 is because of the interference between the double images. The amplitude and period are given in

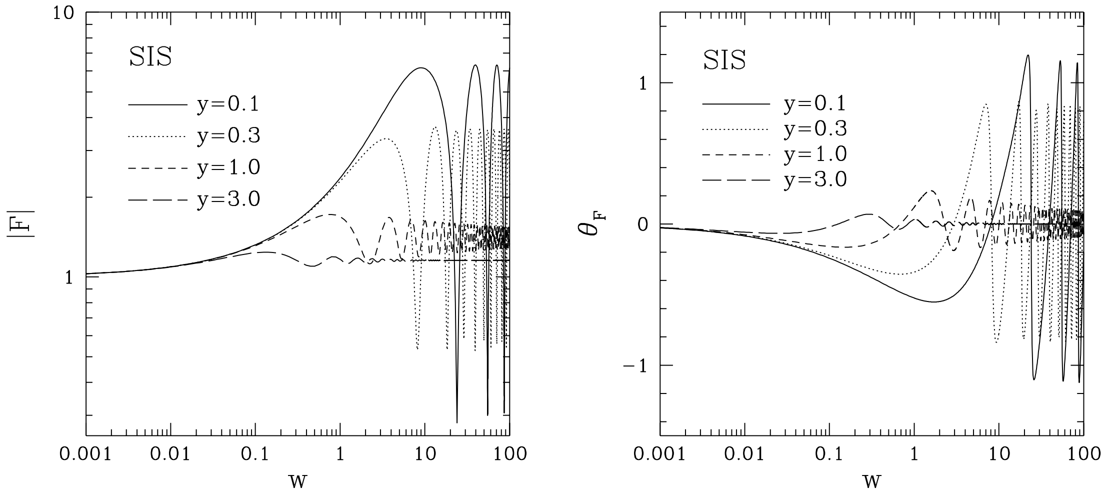

Figure 2.5: Same as Fig.2.4, but for SIS lens. We note that even if $y \geq 1$ (a single image is formed in the geometrical optics limit), the dumped oscillatory behavior appears.

the above equation (2.38) as, $2|\mu_+\mu_-|^{1/2}$ and $w\Delta T$, respectively. As y increases, the magnifications $|\mu_\pm|$ and the amplitude of the oscillation $2|\mu_+\mu_-|^{1/2}$ decrease. Even for $y \geq 1$ ($y = 3$ in Fig.2.5), the damped oscillatory behavior appears, which looks like the time delay factor of $\sin(w\Delta T)$ although only a single image exists in the geometrical optics limit (see equation (2.38)). In the right panel, for $w \gtrsim 1$, θ_F converges to the geometrical optics limit (Eq.(2.37)),

$$\begin{aligned} \theta_F &= \arctan\left[\frac{-|\mu_-|^{1/2}\cos(w\Delta T)}{|\mu_+|^{1/2} + |\mu_-|^{1/2}\sin(w\Delta T)}\right] \quad \text{for } y \leq 1, \\ &= 0 \qquad\qquad\qquad\qquad\qquad\qquad\qquad\quad \text{for } y \geq 1. \end{aligned} \tag{2.39}$$

For $y < 1$, θ_F oscillates with the amplitude of $\arctan(|\mu_-/\mu_+|^{1/2})$ and the period of $w\Delta T$ as shown in right panel. We note for $y \geq 1$ ($y = 3$ in the right panel) that the dumped oscillation is seen in θ_F as well as in $|F|$ (left panel). We discuss the reason for this dumped oscillations in the next chapter.

2.2.3 Navarro-Frenk-White lens

The NFW profile was proposed from numerical simulations of cold dark matter (CDM) halos by Navarro, Frenk & White (1996,1997). They showed that the density profile of the dark halos has the "universal" form,

$$\rho(r) = \frac{\rho_s}{(r/r_s)(r/r_s + 1)^2}, \tag{2.40}$$

where r_s is a scale length and ρ_s is a characteristic density. The scale length r_s is typically 10 (100) kpc on a galactic (cluster) halo scale. The NFW lens is used for lensing by galactic halos and clusters of galaxies. The surface mass density is written as (Bartelmann 1996),

$$
\begin{aligned}
\Sigma(\xi) &= 2\rho_s r_s \left[\frac{2}{\{1-(\xi/r_s)^2\}^{3/2}} \,\mathrm{arctanh}\sqrt{\frac{1-\xi/r_s}{1+\xi/r_s}} - \frac{1}{1-(\xi/r_s)^2} \right] && (2.41)\\
&\qquad \text{for } \ \xi \le r_s, \\
&= 2\rho_s r_s \left[\frac{-2}{\{(\xi/r_s)^2-1\}^{3/2}} \,\arctan\sqrt{\frac{\xi/r_s-1}{\xi/r_s+1}} + \frac{1}{(\xi/r_s)^2-1} \right] && (2.42)\\
&\qquad \text{for } \ \xi \ge r_s.
\end{aligned}
$$

The deflection potential is also written as (Bartelmann 1996; Keeton 2001),

$$
\begin{aligned}
\psi(x) &= \frac{\kappa_s}{2}\left[\left(\ln\frac{x}{2}\right)^2 - \left(\mathrm{arctanh}\sqrt{1-x^2}\right)^2 \right] \quad \text{for } \ x \le 1, \\
&= \frac{\kappa_s}{2}\left[\left(\ln\frac{x}{2}\right)^2 + \left(\arctan\sqrt{x^2-1}\right)^2 \right] \quad \text{for } \ x \ge 1, && (2.43)
\end{aligned}
$$

where $\kappa_s = 16\pi\rho_s(D_L D_{LS}/D_S)r_s$ is the dimensionless surface density and we adopt the scale radius, not the Einstein radius, as the normalization length: $\xi_0 = r_s$. With the above equation (2.43), we numerically integrate the integral of F in equation (2.27). F depends on three parameters; w, y and κ_s. We show the results for $\kappa_s = 1$ and 10, since κ_s is of the order of 1 suggested by the numerical simulations (e.g. Bullock *et al.* 2001).

We show the lens equation, $y = x - \psi'(x)$, for the NFW lens with $\kappa_s = 1$ (left) and 10 (right) in Fig.2.6. For $|y| < y_{crit}$ three images are formed, while for $|y| > y_{crit}$ a single image is formed. The tangential (radial) caustic is $y = 0$ ($y = y_{cr}$) in which the magnification becomes infinite. The image positions x_j, magnifications μ_j and time delays T_j are numerically obtained from the lens equation. F_{geo} is also numerically calculated.

The amplification factor $|F|$ and the phase θ_F for the NFW lens are shown for $\kappa_s = 1$ in Fig.2.7 and for $\kappa_s = 10$ in Fig.2.8. The source position is fixed as $y/y_{cr} = 0.1, 0.3$ and 2 in both figures. The values of w in the horizontal axis of the Fig.2.7 (Fig.2.8) is about 100 (0.1) times larger (smaller) than that in the previous figures (see Fig.2.4 and 2.5). This is because that w is proportional to ξ_0^2 and we adopt the scale radius, not the Einstein radius (which is adopted in the previous cases), as the normalization length: $\xi_0 = r_s$. From the left (right) panel of Fig.2.6, the Einstein radius is $x \sim 0.2$ ($x \sim 3$), which is determined by $y = 0 = x - \psi'(x)$. Then r_s is about 5 (0.3) times larger (smaller) than the Einstein radius, and hence the dimensionless frequency w is about 30 (0.1) times larger (smaller) than that in the case of using the Einstein radius (since $w \propto \xi_0^2$, see Eq.(2.22)). Thus, as

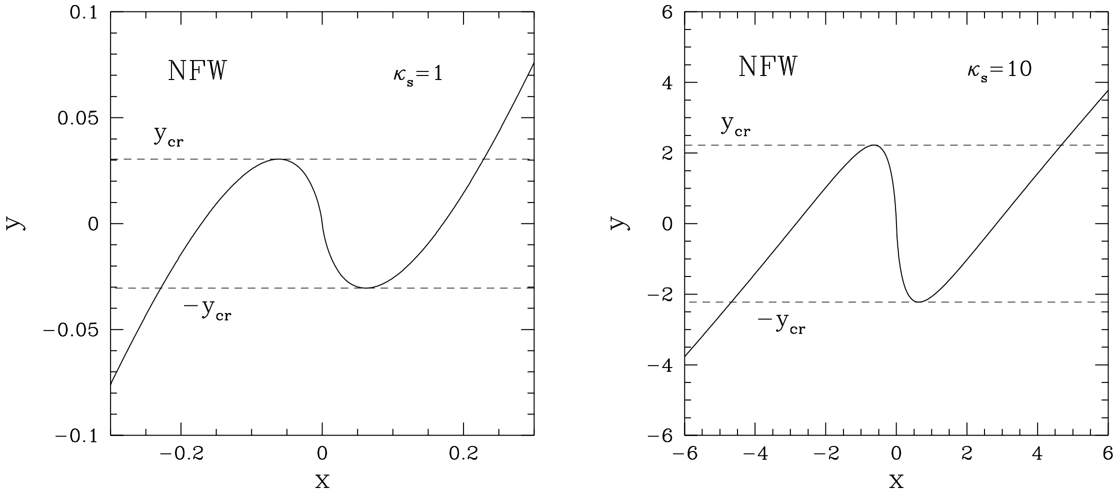

Figure 2.6: The lens equation for the NFW lens with $\kappa_s = 1$ (left) and $\kappa_s = 10$ (right). For $|y| < y_{crit}$ three images are formed, while for $|y| > y_{crit}$ single image is formed.

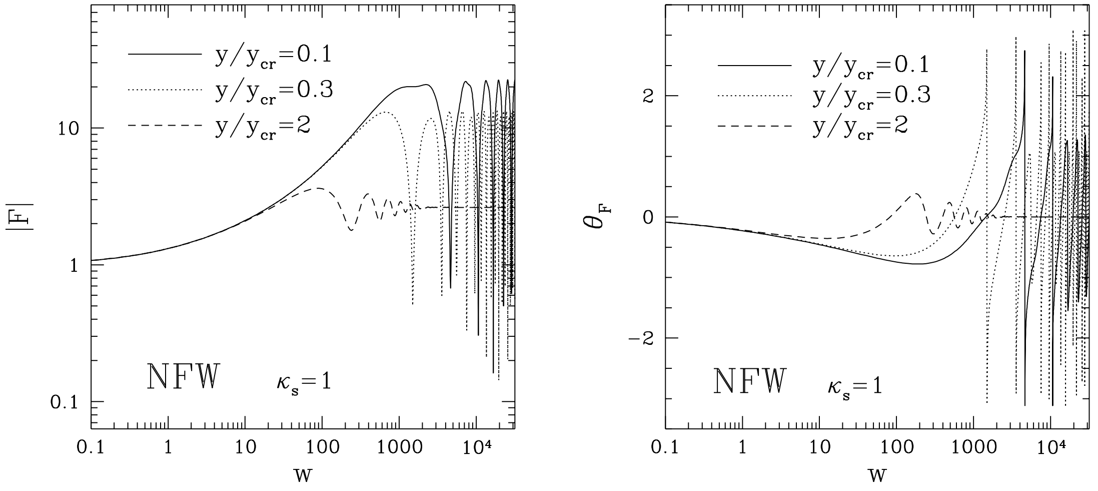

Figure 2.7: Same as Fig.2.4, but for NFW lens with $\kappa_s = 1$. We note that even if $y > y_{cr}$ (a single image is formed in the geometrical optics limit), the dumped oscillatory behavior appears similar to the SIS model.

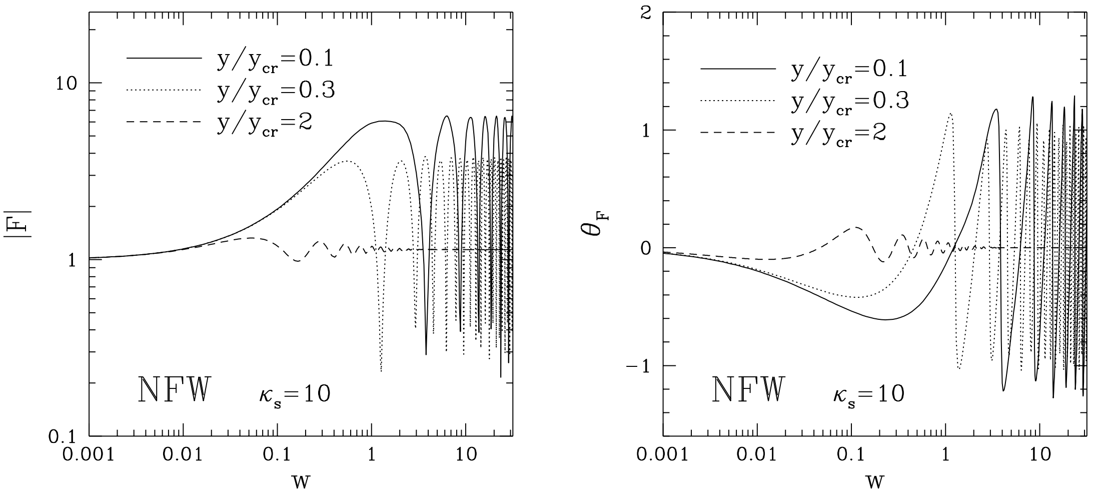

Figure 2.8: Same as Fig.2.7, but for $\kappa_s = 10$.

shown in Fig.2.7, the diffraction effect is important for $w \lesssim 10^2$. For $w \gtrsim 10^2$ in $y/y_{cr} = 0.1$ and 0.3, the three images are formed, and hence the interference patterns between the three images are relatively complicated. We note that for $y/y_{cr} = 2$ the dumped oscillatory behavior is appeared similar to the case in the SIS model with $y = 3$ as shown in Fig.2.5. The reason for this dumped oscillation is discussed in the next chapter.

Fig.2.8 is the same as Fig.2.7, but for $\kappa_s = 10$. The behavior of F and θ_F is similar to that for $\kappa_s = 1$. The diffraction effect is important for $w \lesssim 1$. The amplitude of the oscillation in $|F|$ is smaller than that for $\kappa_s = 1$ in Fig.2.7, because the magnification μ_j is large in the case of $\kappa_s = 1$.

2.2.4 Binary lens

We consider the two point mass lenses with mass M_1 and M_2 in the lens plane. We assume the two lens positions are fixed with the separation $2L$. The surface density of the binary lens is, $\Sigma(\boldsymbol{\xi}) = M_1\delta^2(\boldsymbol{\xi} - \mathbf{L}) + M_2\delta^2(\boldsymbol{\xi} + \mathbf{L})$, where we set $\mathbf{L} = (L, 0)$ in the lens plane. As the normalization constant we adopt the Einstein radius $\xi_0 = [4(M_1 + M_2)D_L D_{LS}/D_S]^{1/2}$, and the (dimensionless) deflection potential is (Schneider & Weiss 1986),

$$\psi(\mathbf{x}) = \nu_1 \ln |\mathbf{x} - \boldsymbol{\ell}| + \nu_2 \ln |\mathbf{x} + \boldsymbol{\ell}| \,. \tag{2.44}$$

The mass ratio $\nu_{1,2}$ and the separation vector $\boldsymbol{\ell}$ are defined as,

$$\nu_{1,2} = \frac{M_{1,2}}{M_1 + M_2}, \quad \boldsymbol{\ell} = \frac{\mathbf{L}}{\xi_0}. \tag{2.45}$$

With the above equation (2.44), we numerically calculate the amplification factor F in Eq.(2.26). Since the binary lens is non-axially symmetric, it takes a long time to numerically calculate the double integral in Eq.(2.26). Thus, we consider the equal mass lens ($\nu_{1,2} = 1/2$) for simplicity. Then, the amplification factor F depends on $w, \mathbf{y}$ and ℓ.

The lens equation for the binary lens is obtained from Eq.(2.44) as, $\mathbf{y} = \mathbf{x} - \nabla_x \psi(\mathbf{x})$. The image positions $\mathbf{x}_j$, magnifications μ_j, and time delays T_j are numerically obtained.[4] In Fig.2.9, we show the lensing configurations with fixed source position $\mathbf{y} = (1, \sqrt{3})/10$ and the separation $\ell = 1.2$ (upper panel) and $\ell = 0.5$ (lower panel). The upper part of each panel displays the source position (star) and the caustics (solid line) in the source plane. The lower part of each panel displays the two point mass lenses (filled circle), the image positions (open circles), and the critical curves (dotted line) in the lens plane. The caustics (critical curves) are defined as the curves on which the magnification is infinite in the source (lens) plane. Thus, if the source is near the caustics the amplification factor F is very large. The three images are formed in the upper panel, while the five images are formed in the lower panel. In the binary lens, if the source is inside the caustics the five images are formed, while if the source is outside the caustics the three images are formed (see Schneider & Weiss 1986).

In Fig.2.10, we show the amplification factor $|F|$ and the phase θ_F for the binary lens in the case shown in Fig.2.9. In this case, since the three or five images are formed, the interference patterns are quit complicated. For $\ell = 0.5$, since the source is near the caustics in Fig.2.9 and the five images are formed, the amplification F is larger than that for $\ell = 1.2$.

In Fig.2.11, we show the amplification factor $|F|$ with the separation $\ell = 0.3, 0.1,$ and 0 (this corresponds to the point mass lens). The source position is $\mathbf{y} = (1, \sqrt{3})/10$ (left panel) and $\mathbf{y} = (\sqrt{3}, 1) \times 0.15$ (right panel). In both these panels, the shape for $\ell = 0.3$ (dashed line) is different from that for the point mass lens (solid line). But, the shape for $\ell = 0.1$ (dotted line) is very similar to that for the point mass lens. Thus, if the separation L is about 0.1 times smaller than the Einstein radius $\ell \lesssim 0.1$ or $L \lesssim 0.1 \times \xi_0$, then the amplification factor is quit similar to that in the point mass lens.

---

[4] We use the method developed by Asada (Asada 2002; Asada, Kasai & Kasai 2002) to obtain $\mathbf{x}_j$, μ_j, and T_j. They showed that the lens equation for the binary lens, which is a simultaneous equation, can be reduced to a real fifth-order equation.

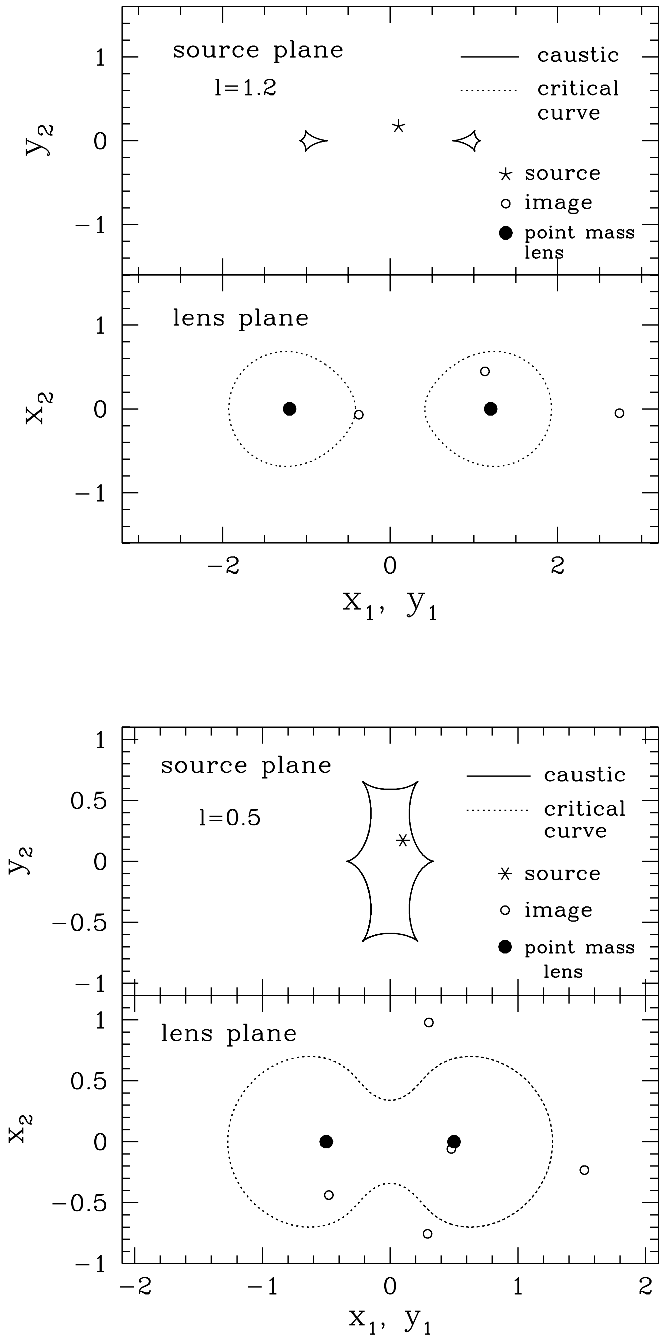

Figure 2.9: The lensing configurations with the separation $\ell = 1.2$ (upper) and $\ell = 0.5$ (lower) for the binary lens with equal mass. The source position is fixed as $\mathbf{y} = (1, \sqrt{3})/10$. In the upper part of each panel, the source position (star) and the caustics (solid line) are shown in the source plane. In the lower part of each panel, the two point mass lenses (filled circle), the image positions (open circles), and the critical curves (dotted line) are shown in the lens plane.

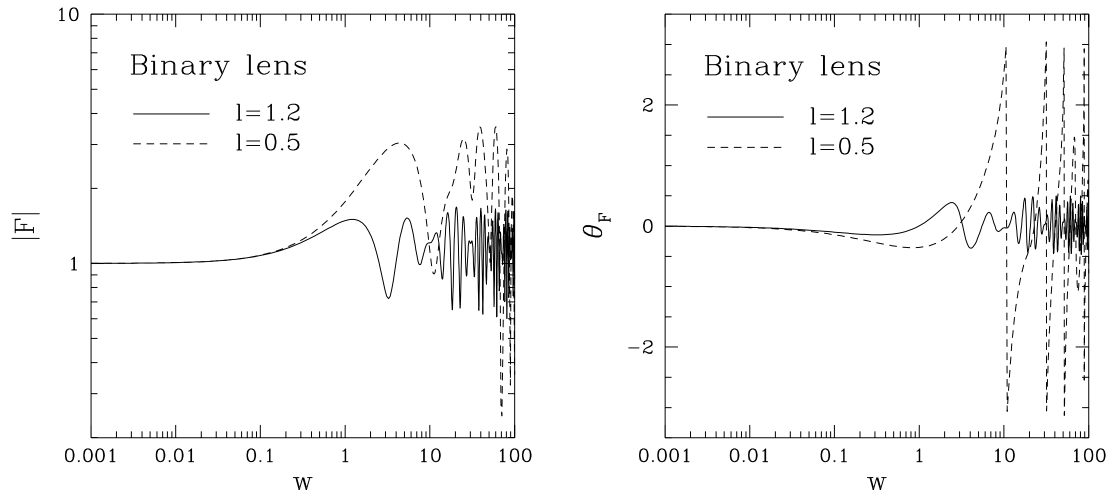

Figure 2.10: Same as Fig.2.4, but for the binary lens with equal mass. The separation of the two lenses is $\ell = 1.2$ (solid line) and $\ell = 0.5$ (dashed line) with the fixed source position $\mathbf{y} = (1, \sqrt{3})/10$.

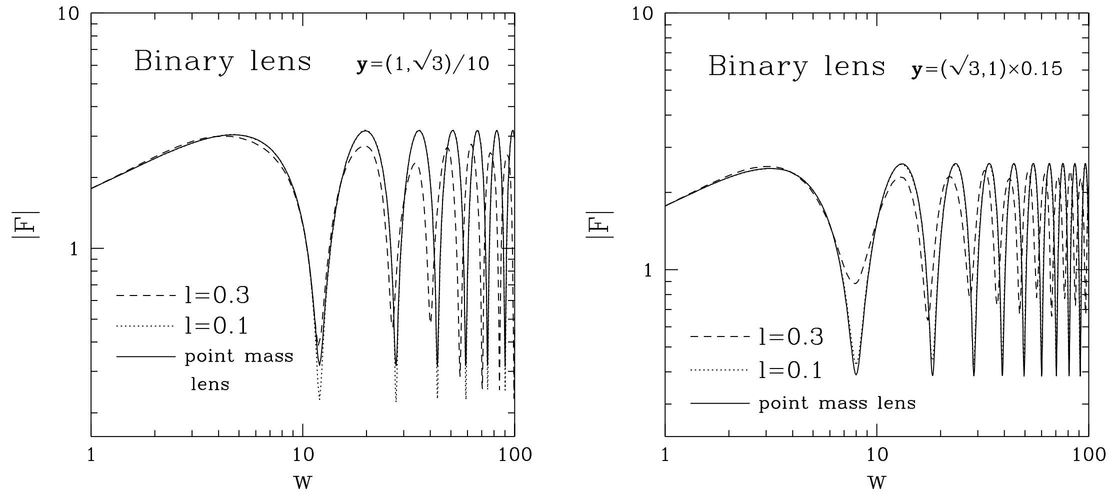

Figure 2.11: The amplification factor $|F|$ for the binary lens with the separation $\ell = 0.3, 0.1$, and 0 (the point mass lens). The source position is $\mathbf{y} = (1, \sqrt{3})/10$ (left panel) and $\mathbf{y} = (\sqrt{3}, 1) \times 0.15$ (right panel).

Chapter 3

Quasi-geometrical Optics Approximation in Gravitational Lensing

In the previous chapter, we reviewed the wave optics in the gravitational lensing of gravitational waves. We showed that for $\lambda \gtrsim M_L$ (where λ is the wavelength of gravitational waves and M_L is the Schwarzschild radius of the lens) the diffraction effect is important and the magnification is small, and for $\lambda \ll M_L$ the geometrical optics approximation is valid. In this chapter, we consider the case for $\lambda \lesssim M_L$, i.e. the quasi-geometrical optics approximation which is the geometrical optics including corrections arising from the effects of the finite wavelength. We can obtain these correction terms by an asymptotic expansion of the diffraction integral (discussed in §2.1) in powers of the wavelength λ.[1] We note that these terms can be obtained analytically.

It is important to derive these correction terms for the following two reasons: (i) calculations in the wave optics are based on the amplification factor F (in Eq.(2.26)), but it is time consuming to numerically calculate F especially for high frequency $\omega \gg 1$ (see the sentences after equation (2.27)). Hence, it is a great saving of computing time to use the analytical expressions. (ii) We can understand clearly the difference between the wave optics and the geometrical optics.

In this chapter, we explore the asymptotic expansion of $F(w, \mathbf{y})$ (in Eq.(2.26)) in powers of the inverse of the dimensionless frequency $1/w$. Here, $1/w$ is roughly equal to λ/M_L from the discussion at the end of §2.1.3. The first term, arising from the high frequency limit $w \to \infty$, corresponds to the geometrical optics limit F_{geo} in the previous chapter. The second term, being of the order of $1/w$, is the first correction term arising from diffraction effect. We study this first correction term, and do not consider the higher order terms, for simplicity.

---

[1] The asymptotic expansion of the diffraction integral has been studied in optics. See the following text books for detailed discussion: Kline & Kay (1965), Ch.XII; Mandel & Wolf (1995), Ch.3.3; Born & Wolf (1997), App.III, and references therein.

3.1 Effect on the Magnifications of the Images

We expand the amplification factor $F(w, \mathbf{y})$ in powers of $1/w$ ($\ll 1$) and discuss the behavior of the order of $1/w$ term. Here, we only consider axially symmetric lens models because the basic formulae are relatively simple, while the case of the non-axially symmetric lens models is discussed in the Appendix C. In the axially symmetric lens, the deflection potential is a function of $|\mathbf{x}|$ as $\psi(\mathbf{x}) = \psi(|\mathbf{x}|)$ where $\mathbf{x} = (x_1, x_2)$; the source position and the image position are $\mathbf{y} = (y, 0)$ and $\mathbf{x}_j = (x_j, 0)$, respectively. The lens equation reduces to a one-dimensional form, $y = x_1 - \partial_1 \psi(x)$. In this case, the expansion of $T(\mathbf{x}, \mathbf{y})$ around the image position $\mathbf{x}_j$ in Eq.(2.29) is simply rewritten as,

$$T(\mathbf{x}, \mathbf{y}) = T_j + \alpha_j \tilde{x}_1^2 + \beta_j \tilde{x}_2^2 + \mathcal{O}(\tilde{x}^3), \tag{3.1}$$

where $\tilde{\mathbf{x}} = \mathbf{x} - \mathbf{x}_j$. T_j, α_j and β_j are defined by,

$$\begin{aligned} T_j &= \frac{1}{2}(x_j - y)^2 - \psi_j + \phi_m & (3.2) \\ \alpha_j &= \frac{1}{2}\left(1 - \psi_j''\right) & (3.3) \\ \beta_j &= \frac{1}{2}\left(1 - \frac{\psi_j'}{|x_j|}\right) & (3.4) \end{aligned}$$

where $\psi_j^{(n)} = d^n \psi(|\mathbf{x}_j|)/dx^n$. The magnification μ_j and the coefficient n_j in F_{geo} of equation (2.30) are also rewritten as, $\mu_j = 1/(4\alpha_j \beta_j) = 1/[(1 - \psi_j'')(1 - \psi_j'/|x_j|)]$ and $n_j = 1/2 - \mathrm{sign}(\alpha_j)/4 - \mathrm{sign}(\beta_j)/4$.

We expand $T(\mathbf{x}, \mathbf{y})$ in Eq.(3.1) up to the fourth order of $\tilde{x}$ as,

$$\begin{aligned} T(\mathbf{x}, \mathbf{y}) = T_j + \alpha_j \tilde{x}_1^2 + \beta_j \tilde{x}_2^2 &+ \frac{1}{6} \sum_{a,b,c} \partial_a \partial_b \partial_c T(\mathbf{x}_j, \mathbf{y}) \tilde{x}_a \tilde{x}_b \tilde{x}_c \\ &+ \frac{1}{24} \sum_{a,b,c,d} \partial_a \partial_b \partial_c \partial_d T(\mathbf{x}_j, \mathbf{y}) \tilde{x}_a \tilde{x}_b \tilde{x}_c \tilde{x}_d + \mathcal{O}(\tilde{x}^5). \end{aligned} \tag{3.5}$$

Inserting the above equation (3.5) into (2.26), we obtain,

$$\begin{aligned} F(w, y) &= \frac{1}{2\pi i} \sum_j e^{iwT_j} \int d^2\mathbf{x}' \exp \Big[i \Big(\alpha_j {x_1'}^2 + \beta_j {x_2'}^2 \\ &\quad + \frac{1}{6\sqrt{w}} \sum_{a,b,c} \partial_a \partial_b \partial_c T(\mathbf{x}_j, \mathbf{y}) x_a' x_b' x_c' \\ &\quad + \frac{1}{24w} \sum_{a,b,c,d} \partial_a \partial_b \partial_c \partial_d T(\mathbf{x}_j, \mathbf{y}) x_a' x_b' x_c' x_d' + \mathcal{O}(w^{-3/2}) \Big) \Big]. \end{aligned} \tag{3.6}$$

Here, we change the integral variable from $\mathbf{x}$ to $\mathbf{x}' = \sqrt{w}\tilde{\mathbf{x}} = \sqrt{w}(\mathbf{x} - \mathbf{x}_j)$. We expand the above equation (3.6) in powers of $1/w$ as,

$$\begin{aligned} F(w,y) &= \frac{1}{2\pi i}\sum_j e^{iwT_j}\int d^2\mathbf{x}' e^{i\left(\alpha_j x_1'^2 + \beta_j x_2'^2\right)}\left[1 + \frac{i}{6\sqrt{w}}\sum_{a,b,c}\partial_a\partial_b\partial_c T(\mathbf{x}_j,\mathbf{y})x'_a x'_b x'_c \right. \\ & + \frac{1}{w}\left\{ -\frac{1}{72}\left(\sum_{a,b,c}\partial_a\partial_b\partial_c T(\mathbf{x}_j,\mathbf{y})x'_a x'_b x'_c\right)^2 \right. \\ & \left.\left. + \frac{i}{24}\sum_{a,b,c,d}\partial_a\partial_b\partial_c\partial_d T(\mathbf{x}_j,\mathbf{y})x'_a x'_b x'_c x'_d \right\} + \mathcal{O}(w^{-3/2})\right]. \end{aligned} \tag{3.7}$$

The first term of the above equation (3.7) is the amplification factor in the geometrical optics limit F_{geo} in equation (2.30). The integral in the second term vanishes because the integrand is an odd function of x'_a. The third term is the correction term, being proportional to $1/w$, arising from the diffraction effect. Thus the deviation from the geometrical optics is of the order of $1/w \sim \lambda/M_L$. Inserting $T(\mathbf{x},\mathbf{y})$ in Eq.(2.24) into (3.7), we obtain F as,

$$F(w,y) = \sum_j |\mu_j|^{1/2}\left(1 + \frac{i}{w}\Delta_j\right)e^{iwT_j - i\pi n_j} + \mathcal{O}(w^{-2}), \tag{3.8}$$

where

$$\Delta_j = \frac{1}{16}\left[\frac{1}{2\alpha_j^2}\psi_j^{(4)} + \frac{5}{12\alpha_j^3}\psi_j^{(3)2} + \frac{1}{\alpha_j^2}\frac{\psi_j^{(3)}}{|x_j|} + \frac{\alpha_j - \beta_j}{\alpha_j\beta_j}\frac{1}{|x_j|^2}\right], \tag{3.9}$$

and Δ_j is a real number. We denote dF_m as the second term of the above equation (3.8) as,

$$dF_m(w,y) \equiv \frac{i}{w}\sum_j \Delta_j |\mu_j|^{1/2} e^{iwT_j - i\pi n_j}. \tag{3.10}$$

Since dF_m is the correction term arising near the image positions, this term represents the corrections to the properties of these images such as its magnifications, and the time delays. We rewrite F in above equation (3.8) as,

$$F(w,y) = \sum_j \left| \mu_j\left[1 + \left(\frac{\Delta_j}{w}\right)^2\right]\right|^{1/2} e^{iwT_j + i\delta\varphi - i\pi n_j} + \mathcal{O}(w^{-2}), \tag{3.11}$$

where $\delta\varphi = \arctan(\Delta_j/w)$. Thus in the quasi-geometrical optics approximation, the magnification μ_j is modified to $\mu_j[1+(\Delta_j/w)^2]$, where $(\Delta_j/w)^2$ is of the order of $(\lambda/M_L)^2$. That is, the magnification is slightly larger than that in the geometrical optics limit. The phase is also changed by $\delta\varphi$, which is of the order of λ/M_L.

The lensed wave in the time domain is given by,

$$\phi^L(t,\mathbf{r}) = \phi^L_{geo}(t,\mathbf{r}) + \sum_j \tilde{\Delta}_j |\mu_j|^{1/2} e^{-i\pi n_j}\int^{t - t_{d,j}} dt' \phi(t',\mathbf{r}), \tag{3.12}$$

where $\tilde{\Delta}_j = (D_L D_{LS}/D_S)\xi_0^{-2}(1+z_L)^{-1}\Delta_j$ and ϕ^L_{geo} is the lensed wave in the geometrical optics limit in equation (2.31). The second term is the deviation from the geometrical optics limit. For example, we consider the monochromatic wave $\phi(t)$ with the frequency ω as the unlensed waveform: $\phi(t,\mathbf{r}) = A\sin(\omega t + \varphi_0)$, where A is the amplitude and φ_0 is the phase. Inserting this monochromatic wave into Eq.(2.31) and (3.12), we obtain the lensed wave ϕ^L as,

$$\phi^L(t,\mathbf{r}) = A\sum_j \left| \mu_j \left[1+\left(\frac{\tilde{\Delta}_j}{\omega}\right)^2\right]\right|^{1/2} \sin\left[\,\omega(t-t_{d,j})+\varphi_0+\delta\varphi\right]\; e^{-i\pi n_j}, \qquad (3.13)$$

where $\delta\varphi = \arctan(\tilde{\Delta}_j/\omega)$, and we note that $\tilde{\Delta}_j/\omega = \Delta_j/w$. From the above equation, the each lensed image is magnified by $\mu_j[1+(\tilde{\Delta}_j/\omega)^2]$, and the phase is changed by $\delta\varphi$. These results are consistent with that in the frequency domain (see the sentences after equation (3.11)).

3.2 Contributions from the Non-stationary Points

In the previous section, we showed that the contributions to the diffraction integral F arise from the stationary points (or image positions). In this section, we discuss the contributions from the non-stationary points. We denote $\mathbf{x}_{ns}$ as the non-stationary point, at which the condition $|\nabla T| \neq 0$ satisfies. If $T(\mathbf{x},\mathbf{y})$ can be expanded at $\mathbf{x}_{ns}$, we obtain the series of T similar to Eq.(3.1) as,

$$T(\mathbf{x},\mathbf{y}) = T_{ns} + T_1'\tilde{x}_1 + T_2'\tilde{x}_2 + \alpha_{ns}\tilde{x}_1^2 + \beta_{ns}\tilde{x}_2^2 + \mathcal{O}(\tilde{x}^3), \qquad (3.14)$$

where $\tilde{\mathbf{x}} = \mathbf{x} - \mathbf{x}_{ns}$, and $T'_{1,2} = \partial_{1,2}T(\mathbf{x}_{ns},\mathbf{y})$. Note that either T_1' or T_2' does not vanish because of $|\nabla T| \neq 0$ at $\mathbf{x}_{ns}$. T_{ns}, α_{ns}, and β_{ns} are defined same as equations from (3.2) to (3.4), but at the non-stationary point $\mathbf{x}_{ns}$.

Inserting the above equation (3.14) to (2.26), we obtain,

$$F(w,y) = \frac{e^{iwT_{ns}}}{2\pi i w}\int d^2\mathbf{x}' \exp\left[i\left\{T_1'x_1' + T_2'x_2' + \frac{1}{w}\left(\alpha_j {x_1'}^2 + \beta_j {x_2'}^2\right) + \mathcal{O}(w^{-2})\right\}\right], \qquad (3.15)$$

where $\mathbf{x}' = w\tilde{\mathbf{x}}$. We expand the integrand of the equation (3.15) in powers of $1/w$ as,

$$F(w,y) = \frac{e^{iwT_{ns}}}{2\pi i w}\int d^2\mathbf{x}'\; e^{i(T_1'x_1' + T_2'x_2')}\left[1 + \frac{1}{w}\left(\alpha_{ns}{x_1'}^2 + \beta_{ns}{x_2'}^2\right) + \mathcal{O}(w^{-2})\right]. \qquad (3.16)$$

The above equation can be integrated as,

$$F(w,y) = 2\pi\frac{e^{iwT_{ns}}}{iw}\left[\delta(T_1')\delta(T_2') - \frac{1}{w}\left(\alpha_{ns}\frac{\partial^2}{\partial T_1'^2} + \beta_{ns}\frac{\partial^2}{\partial T_2'^2}\right)\delta(T_1')\delta(T_2') + \mathcal{O}(w^{-2})\right]. \qquad (3.17)$$

Thus, if both $T'_1 \neq 0$ and $T'_2 \neq 0$, the above equation vanishes. Even if either $T'_1 = 0$ or $T'_2 = 0$, it is easy to show that F vanishes doing the same calculations from equations (3.15) to (3.17). Thus, the contributions to the amplification factor F at the non-stationary points are negligible.

In the above discussion, we assume that $T(\mathbf{x}, \mathbf{y})$ has the derivatives at the non-stationary point $\mathbf{x}_{ns}$ (see the sentences before the equation (3.14)). But, if the derivatives of T are not defined at $\mathbf{x}_{ns}$, the result in Eq.(3.17) should be reconsidered. If the lens has the cuspy (or singular) density profile at the center, the derivatives of T are not defined at the lens center. We will discuss this case in the next section.

3.3 Central Cusp of the Lens

We consider the correction terms in the amplification factor F arising at the central cusp of the lens. For the inner density profile of the lens $\rho \propto r^{-\alpha}$ $(0 < \alpha \leq 2)$,[2] the surface density and the deflection potential at small radius are given by,

$$\begin{aligned} \Sigma(\boldsymbol{\xi}) &\propto \xi^{-\alpha+1} \quad \text{for } \alpha \neq 1, \\ &\propto \ln \xi \qquad \text{for } \alpha = 1, \end{aligned} \tag{3.18}$$

$$\begin{aligned} \psi(\mathbf{x}) &\propto x^{-\alpha+3} \quad \text{for } \alpha \neq 1, \\ &\propto x^2 \ln x \quad \text{for } \alpha = 1. \end{aligned} \tag{3.19}$$

We note that the Taylor series of $\psi(\mathbf{x})$ around $\mathbf{x} = 0$ like Eq.(3.14) cannot be obtained from the above equation (3.19). For example, in the case of $\alpha = 2$, the deflection potential is $\psi \propto x$, but the derivative of $|\mathbf{x}|$ is discontinuous at $\mathbf{x} = 0$. Hence we use ψ in Eq.(3.19) directly, not the Taylor series in equation (3.14). Let us calculate the correction terms in the amplification factor contributed from the lens center for following four cases; $\alpha = 2$, $1 < \alpha < 2$, $\alpha = 1$, and $0 < \alpha < 1$.

Case of $\boldsymbol{\alpha = 2}$ If the inner density profile is $\rho \propto r^{-2}$ (e.g. the singular isothermal sphere model), the deflection potential is given by $\psi(\mathbf{x}) = \psi_0 x$ (ψ_0 is a constant) from equation (3.19). Inserting this potential ψ into equation (2.26), we obtain,

$$F(w, y) = \frac{e^{iw[y^2/2 + \phi_m(y)]}}{2\pi i w} \int dx'^2 \exp\left[-i\left\{ y x'_1 + \psi_0 \sqrt{x'^2_1 + x'^2_2} + \mathcal{O}(1/w) \right\}\right], \tag{3.20}$$

where we changed the integral variable from $\mathbf{x}$ to $\mathbf{x}' = w\mathbf{x}$. We denote $dF_c(w, y)$ as the leading term of the above integral which is proportional to $1/w$. dF_c is obtained by integrating the above equation as,

---

[2] We do not consider the steeper profile $\alpha > 2$, since the mass at the lens center is infinite.

$$\begin{aligned} dF_c(w,y) &= \frac{e^{iw[y^2/2+\phi_m(y)]}}{w} \frac{1}{(y^2-\psi_0^2)^{3/2}} \quad \text{for} \ \ |y|>|\psi_0|, & (3.21)\\ &= \frac{e^{iw[y^2/2+\phi_m(y)]}}{w} \frac{i}{(\psi_0^2-y^2)^{3/2}} \quad \text{for} \ \ |y|<|\psi_0|. & (3.22) \end{aligned}$$

Thus, the contributions to the amplification factor F at the lens center is of the order of $1/w \sim \lambda/M_L$. This is because of the singularity in the density profile at the lens center. The correction terms dF_c in equation (3.21) and (3.22) represent a diffracted image which is formed at the lens center by the diffraction effect. The magnification of this image is of the order of $\sim \lambda/M_L$.

Case of $1<\alpha<2$ The deflection potential at the small radius is $\psi(\mathbf{x}) = \psi_0 \ x^{-\alpha+3}$ (ψ_0 is a constant) from equation (3.19). We insert ψ into equation (2.27),

$$F(w,y) = -\frac{i}{w} \ e^{iw[y^2/2+\phi_m(y)]} \int_0^\infty dx'x' J_0(yx') \ e^{i/(2w)x'^2} \ e^{-iw^{\alpha-2}\psi_0 x'^{-\alpha+3}}, \tag{3.23}$$

where $x'=wx$. We expand the integrand in powers of $1/w$ as:

$$F(w,y) = -\frac{i}{w} \ e^{iw[y^2/2+\phi_m(y)]} \int_0^\infty dx'x' J_0(yx') \left[1 - iw^{\alpha-2}\psi_0 \ x'^{-\alpha+3} + \mathcal{O}(w^{2(\alpha-2)})\right]. \tag{3.24}$$

The above equation can be integrated analytically (e.g. Gradshteyn & Ryzhik 2000). [3] The first term in Eq.(3.24) vanishes, and the second term is the leading term. We denote the leading term as $dF_c(w,y)$:

$$dF_c(w,y) = -\frac{1}{2}\left(\frac{y}{2}\right)^{\alpha-5} \psi_0 w^{\alpha-3} \ e^{iw[y^2/2+\phi_m(y)]} \ \frac{\Gamma((5-\alpha)/2)}{\Gamma((\alpha-3)/2)}, \tag{3.25}$$

where Γ is the gamma function. Thus, the diffracted image is formed at the lens center similar to the case of $\alpha=2$. The magnification is roughly $\sim (\lambda/M_L)^{3-\alpha}$.

Case of $\alpha=1$ If the inner density profile is $\rho \propto r^{-1}$ (e.g. the Navarro Frenk White model), the deflection potential is given by $\psi(\mathbf{x}) = \psi_0 x^2 \ln x$ (ψ_0 is a constant) from equation (3.19). Inserting this ψ into equation (2.27), we have,

$$F(w,y) = -\frac{i}{w} \ e^{iw[y^2/2+\phi_m(y)]} \int_0^\infty dx'x' J_0(yx') \ e^{i/(2w)x'^2[1-2\psi_0\ln(x'/w)]}, \tag{3.26}$$

---

[3] A formula for the Bessel function, $x^n J_0(yx) = [d/(ydy)]^n (y^n J_n(yx))$, where n is a integer (Abramowitz & Stegun 1970), is useful to integrate F.

where $x' = wx$. We expand the integrand of Eq.(3.26) in powers of $1/w$:

$$F(w, y) = -\frac{i}{w} e^{iw[y^2/2+\phi_m(y)]} \int_0^\infty dx' x' J_0(yx') \left[1 + \frac{i}{2w} x'^2 \left\{ 1 - 2\psi_0 \ln \frac{x'}{w} \right\} + \mathcal{O}(w^{-2}) \right]. \quad (3.27)$$

The above equation can be integrated analytically (e.g. Gradshteyn & Ryzhik 2000), similar to the previous case of $1 < \alpha < 2$. The first term in Eq.(3.27) vanishes and the second term becomes the leading term. Denoting $dF_c(w, y)$ as this leading term, dF_c is written as,

$$dF_c(w, y) = \frac{-4\psi_0}{(wy^2)^2} e^{iw[y^2/2+\phi_m(y)]}. \quad (3.28)$$

Thus, the diffracted image is formed at the lens center similar to the previous cases. The magnification is roughly $\sim (\lambda/M_L)^2$.

Case of $0 < \alpha < 1$ The diffraction potential is the same as that in the previous case $1 < \alpha < 2$, and the amplification factor is similarly given in equation (3.23). We expand the integrand of Eq.(3.23) in powers of $1/w$ as:

$$F(w, y) = -\frac{i}{w} e^{iw[y^2/2+\phi_m(y)]} \int_0^\infty dx' x' J_0(yx') \left[1 + \frac{i}{2w} x'^2 - iw^{\alpha-2} \psi_0 \, x'^{-\alpha+3} + \mathcal{O}(1/w^2) \right], \quad (3.29)$$

where we note that the leading correction term in the integrand is $\sim 1/w$, not $\sim w^{\alpha-2}$ (this is the case for equation (3.24)), since $0 < \alpha < 1$. The above equation can be integrated similar to the previous cases. The first and the second term in Eq.(3.29) vanish, and the leading term is the third term. Denoting $dF_c(w, y)$ as this leading term, we have dF_c as,

$$dF_c(w, y) = -\frac{1}{2} \left(\frac{y}{2} \right)^{\alpha-5} \psi_0 w^{\alpha-3} \, e^{iw[y^2/2+\phi_m(y)]} \, \frac{\Gamma((5-\alpha)/2)}{\Gamma((\alpha-3)/2)}. \quad (3.30)$$

This is the same as dF_c in Eq.(3.25).

From the discussion for the four cases, the diffracted image is always formed at the lens center for the inner density profile $\rho \propto r^{-\alpha}$ $(0 < \alpha \leq 2)$. The magnification of this central image is roughly given by, $\mu \sim (\lambda/M_L)^{3-\alpha}$.

3.4 Results for Specific Lens Models

We apply the quasi-geometrical optics approximation to simple lens models. We consider the following axially symmetric lens models: point mass lens, singular isothermal sphere (SIS) lens, isothermal sphere lens with a finite core, and Navarro-Frenk-White (NFW) lens. Since the amplification factor F and that in the geometrical optics F_{geo} are discussed in the previous chapter, we derive only dF_m (in §3.1) and dF_c (in §3.3) for the above lens models. We define dF for convenience as the sum of dF_m and dF_c:

$$dF(w,y) \equiv dF_m(w,y) + dF_c(w,y). \tag{3.31}$$

3.4.1 Point Mass Lens

The surface mass density is given by, $\Sigma(\boldsymbol{\xi}) = M_L \delta^2(\boldsymbol{\xi})$, where M_L is the lens mass. F and F_{geo} are given in equation (2.32) and (2.33), respectively. In this model $dF_c = 0$, and dF $(= dF_m)$ is given from equation (3.10) by,

$$dF(w,y) = \frac{i}{3w}\frac{4x_+^2-1}{(x_+^2+1)^3(x_+^2-1)}\left|\mu_+\right|^{1/2} + \frac{1}{3w}\frac{4x_-^2-1}{(x_-^2+1)^3(x_-^2-1)}\left|\mu_-\right|^{1/2} e^{iw\Delta T}, \tag{3.32}$$

where $x_\pm = (y \pm \sqrt{y^2+4})/2$ is the position of each image, $\mu_\pm = 1/2 \pm (y^2+2)/(2y\sqrt{y^2+4})$ is the magnification of each image, and $\Delta T = y\sqrt{y^2+4}/2 + \ln((\sqrt{y^2+4}+y)/(\sqrt{y^2+4}-y))$ is the time delay between the double images. The first and second terms in Eq.(3.32) are the correction terms for the magnifications of the two images as discussed in §3.1.

In Fig.3.1(a), the amplification factor is shown as a function of w with a fixed source position $y = 0.3$. The solid line is the full result $|F|$ in Eq.(2.32); the dotted line is the geometrical optics approximation $|F_{geo}|$ in Eq.(2.33); the dashed line is the quasi-geometrical optics approximation $|F_{geo}+dF|$ in Eq.(2.33) and (3.32). The oscillatory behavior (in Fig.3.1(a)) is due to the interference between the double images (see also the discussion in §2.2.1). For large w ($\gtrsim 10$), these three lines asymptotically converge.

In Fig.3.1(b), the differences between F, F_{geo} and $F_{geo} + dF$ are shown as a function of w with $y = 0.3$. The thin solid line is $|F - F_{geo}|$, and the thin dashed line is $|F - (F_{geo} + dF)|$. The thick solid (dashed) line represents the power of $w^{-1}(w^{-2})$. From this figure, for larger w ($\gg 1$) F converges to F_{geo} with the error of $\mathcal{O}(1/w)$ and converges to $F_{geo} + dF$ with the error of $\mathcal{O}(1/w^2)$. These results are consistent with the analytical calculation in section 3.1.

3.4.2 Singular Isothermal Sphere

The surface density of the SIS model is characterized by the velocity dispersion v as, $\Sigma(\boldsymbol{\xi}) = v^2/(2\xi)$, and the deflection potential is given by, $\psi(\mathbf{x}) = x$. F and

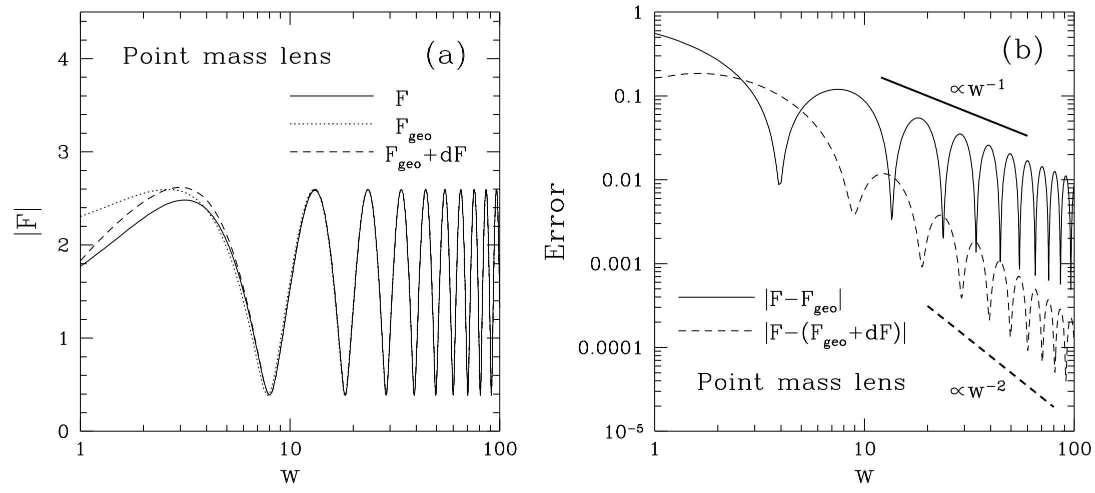

Figure 3.1: (a) The amplification factor $|F|$ for a point mass lens as a function of w with a fixed source position $y = 0.3$. The solid line is the full result F; the dotted line is the geometrical optics approximation F_{geo}; the dashed line is the quasi-geometrical optics approximation $F_{geo} + dF$. (b) The differences between F, F_{geo} and $F_{geo} + dF$ for a point mass lens as a function of w with $y = 0.3$. The thin solid line is $|F - F_{geo}|$, and the thin dashed line is $|F - (F_{geo} + dF)|$. The thick solid (dashed) line represents the power of $w^{-1}(w^{-2})$.

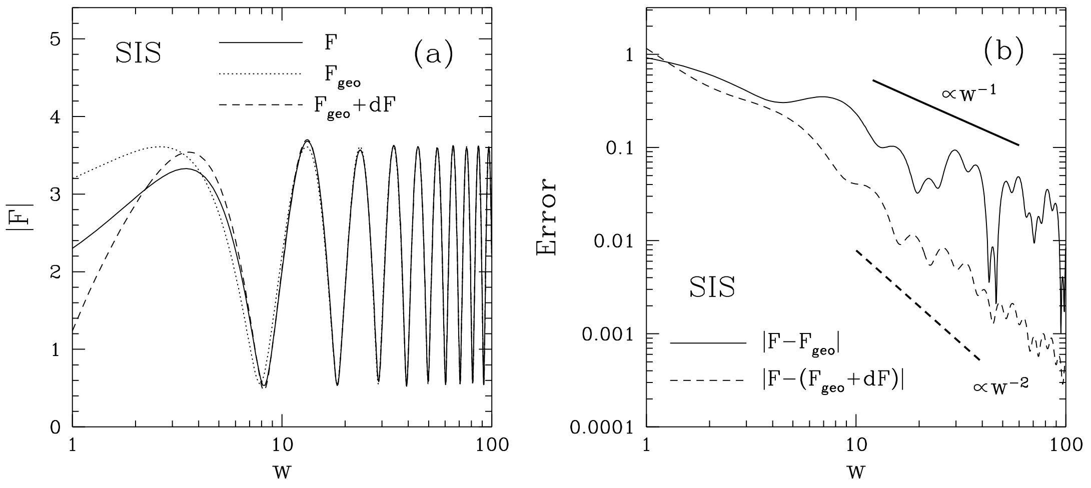

Figure 3.2: Same as Fig.3.1, but for SIS lens with a source position $y = 0.3$.

F_{geo} are given in equation (2.36) and (2.37), respectively. In the quasi-geometrical optics approximation, dF is given by,

$$\begin{aligned} dF(w,y) &= \frac{i}{8w}\frac{|\mu_+|^{1/2}}{y(y+1)^2} - \frac{1}{8w}\frac{|\mu_-|^{1/2}}{y(1-y)^2}\ e^{iw\Delta T} + \frac{i}{w}\frac{1}{(1-y^2)^{3/2}}\ e^{iw[y^2/2+\phi_m(y)]}, \\ & \qquad\qquad\qquad\qquad\qquad\qquad\qquad\qquad\qquad\qquad \text{for } y < 1, \\ &= \frac{i}{8w}\frac{|\mu_+|^{1/2}}{y(y+1)^2} + \frac{1}{w}\frac{1}{(y^2-1)^{3/2}}\ e^{iw[y^2/2+\phi_m(y)]} \qquad \text{for } y \geq 1, \end{aligned} \tag{3.33}$$

where $\mu_\pm = \pm 1 + 1/y$, $\Delta T = 2y$, and $\phi_m(y) = y + 1/2$. For $y < 1$, the first and the second term in Eq.(3.33) are correction terms for the magnifications of the images formed in the geometrical optics (i.e. dF_m in §3.1), and the third term corresponds to the diffracted image at the lens center (i.e. dF_c in §3.2). For $y \geq 1$, the first term is correction term for the magnification dF_m, and the second term corresponds to the diffracted image at the lens center dF_c. Thus, in the quasi-geometrical optics approximation, for $y < 1$ the three images are formed, while for $y \geq 1$ the double images are formed in the SIS model.

Fig.3.2 is the same as Fig.3.1, but for the SIS lens with a source position $y = 0.3$. In Fig.3.2(a), the behavior is similar to that in the point mass lens (in Fig.3.1(a)). The oscillation of $|F_{geo}|$ is because of the interference between the double images, while the oscillation of $|F_{geo} + dF|$ is because of that among the three images. But, since the diffracted image is fainter than the others, the difference between $|F_{geo}|$ and $|F_{geo} + dF|$ is very small for $w \gtrsim 10$ as shown in Fig.3.2(a). As shown in Fig.3.2(b), the errors decrease as w increases, and the results are consistent with the analytical calculation.

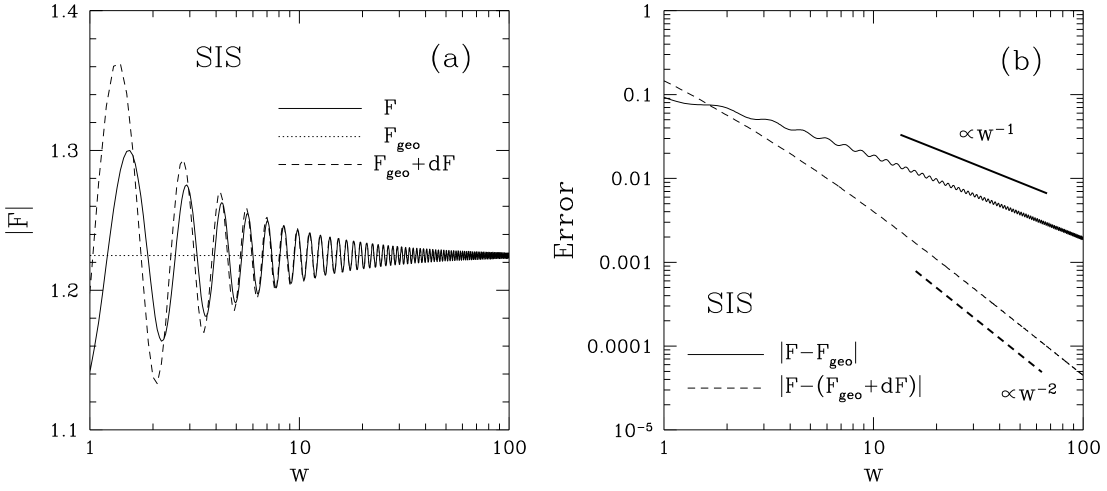

Figure 3.3: Same as Fig.3.2, but for $y = 2$.

Fig.3.3 is the same as Fig.3.2, but for the source position $y = 2$. In Fig.3.3(a), the damped oscillatory behavior of $|F|$ appears, which looks like the interference between the images, although only a single image exists in the geometrical optics (see the behavior of $|F_{geo}|$). For large w ($\gg 1$), $|F|$ converges to $|F_{geo} + dF|$ which is given from Eq.(2.37) and (3.33) by,

$$|F_{geo} + dF| = |\mu_+|^{1/2} + \frac{1}{w(y^2-1)^{3/2}} \cos\left[\frac{w}{2}(y+1)^2\right] + \mathcal{O}(1/w^2). \qquad (3.34)$$

The first term is the magnification of the single image formed in the geometrical optics. The second term is the interference between this image and the diffracted image formed at the lens center in the quasi-geometrical optics approximation. Hence, the damped oscillatory behavior is due to the interference between these images. The amplitude and the period of this oscillation are $1/[w(y^2-1)^{3/2}]$ and $w(y+1)^2/2$ (in equation (3.34)), respectively. As shown in Fig.3.3(b), the errors decrease as w increases, and the results are consistent with the analytical calculation.

3.4.3 Isothermal Sphere with a Finite Core

We investigate the effect of a finite core at lens center on the amplification factor. We consider the isothermal sphere having a finite core. The deflection potential is $\psi(x) = (x^2 + x_c^2)^{1/2}$ where x_c is a dimensionless core radius, and we set $x_c = 0.2$. The amplification factor F is numerically calculated in equation (2.27).

Fig.3.4 is the same as Fig.3.1, but for the isothermal sphere with a core model (core radius is $x_c = 0.2$). The source position is $y = 2$, and the single image

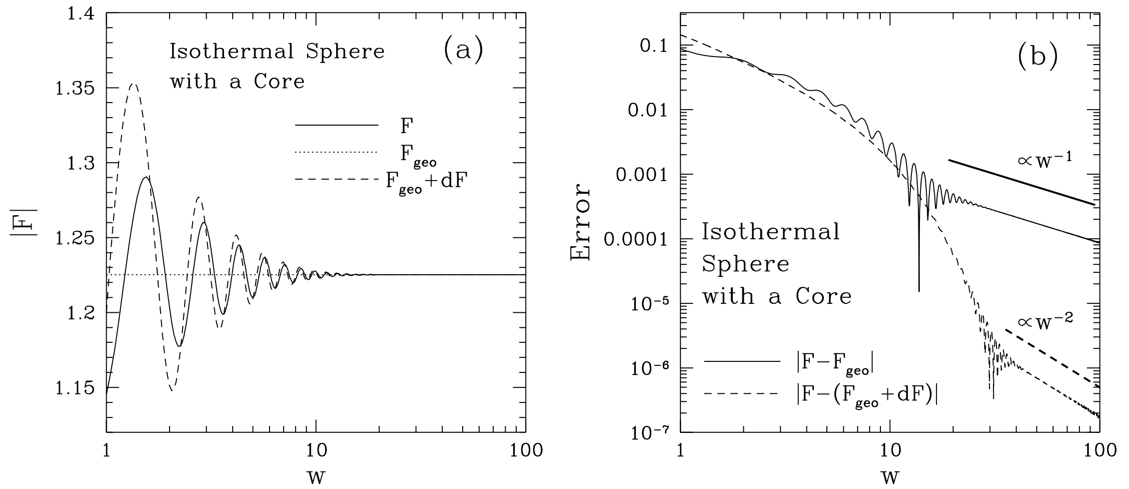

Figure 3.4: Same as Fig.3.1, but for the isothermal sphere with a core lens. The core radius is $x_c = 0.2$ and the source position is $y = 2$.

is formed in the geometrical optics. In this model, the central core of the lens contributes the integral of F in Eq.(2.26). Denoting dF_c as the contribution of F at the lens center, we obtain,

$$dF_c(w, y) = \frac{e^{iwy^2/2}}{2\pi iw} \int d\mathbf{x}'^2 \exp\left[-i\left\{yx_1' + \sqrt{x_1'^2 + x_2'^2 + (wx_c)^2} + \mathcal{O}(1/w)\right\}\right]. \tag{3.35}$$

For $wx_c \lesssim 1$ the above equation is the same as dF_c in the SIS model (see equation (3.20)) and $dF_c \propto 1/w$, but for $wx_c \gtrsim 1$ dF_c exponentially decreases as w increases. Thus, for the small core $x_c \lesssim 1/w$ the wave does not feel the existence of the core, and the behavior of dF_c is similar to that for the lens without the core. The results for F, F_{geo}, and dF are consistent with the analytical calculation as shown in Fig.3.4(b).

3.4.4 NFW lens

The density profile is given in Eq.(2.40) as, $\rho(r) = \rho_s(r/r_s)^{-1}(r/r_s + 1)^{-2}$ where r_s is the scale length and ρ_s is the characteristic density. The deflection potential is given in Eq.(2.43), and the amplification factor F is numerically obtained with Eq.(2.27). In the quasi-geometrical optics approximation, dF is given by,

$$dF(w, y) = \frac{i}{w} \sum_j \Delta_j \left|\mu_j\right|^{1/2} e^{iwT_j - i\pi n_j} + \frac{\kappa_s}{(wy^2)^2}\, e^{iw[y^2/2 + \phi_m(y)]} \tag{3.36}$$

where $\kappa_s = 16\pi\rho_s(D_L D_{LS}/D_S)r_s$ is the dimensionless surface density. The first term in Eq.(3.36) is the corrections for the magnifications of the images (i.e. dF_m

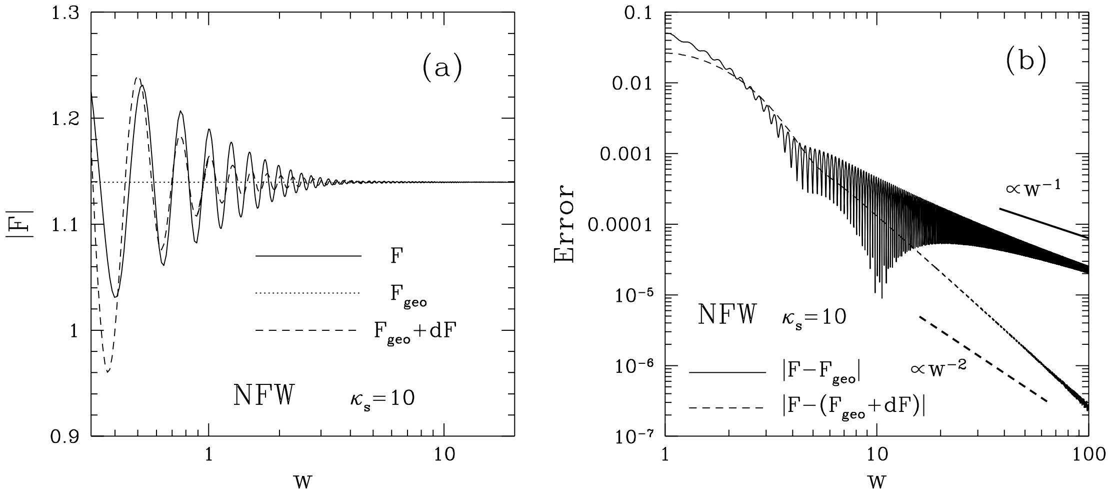

Figure 3.5: Same as Fig.3.1, but for the NFW lens for $\kappa_s = 10$ with $y/y_{cr} = 2$.

in §3.1). μ_j, T_j, and n_j are numerically obtained from the lens equation. The second term corresponds to the diffracted image at the lens center (i.e. dF_c in §3.2).

Fig.3.5 is the same as Fig.3.1, but for the NFW model for $\kappa_s = 10$ with the source position $y/y_{cr} = 2$. A single image is formed in the geometrical optics. In Fig.3.5(a), the dumped oscillatory behavior of $|F|$ is appeared, similar to the case of the SIS. For large w, $|F|$ asymptotically converges to $|F_{geo} + dF|$, which is given from Eq.(3.36) as,

$$|F_{geo} + dF| \simeq |\mu_1|^{1/2} + \frac{\Delta_1}{2w^2}|\mu_1|^{1/2} + \frac{\kappa_s}{(wy^2)^2} \cos\left\{w\left(T_1 - y^2/2 - \phi_m(y)\right)\right\} \quad (3.37)$$

where we set $j = 1$ in Eq.(3.36) since the single image is formed in the geometrical optics. The first and the second term in Eq.(3.37) correspond to the image formed in the quasi-geometrical optics approximation. The third term is the interference between the single image formed in the geometrical optics and the diffracted image formed at the lens center. The amplitude and the period of the oscillation are $\kappa_s/(wy^2)^2$ and $w\left(T_1 - y^2/2 - \phi_m(y)\right)$, respectively. As shown in Fig.3.3(b), the results are consistent with the analytical calculation.

Chapter 4

Wave Effects in the Gravitational Lensing of Gravitational Waves from Chirping Binaries

In the previous chapters 2 and 3, we discussed the physical aspect of the wave optics in the gravitational lensing. In this chapter, we apply the wave optics to the real observational situations. We consider the gravitational lensing of gravitational waves from chirping binaries. We take the coalescence of the super massive black holes (SMBHs) of mass $10^4-10^7 M_\odot$ at the redshift $z = 1-10$ as the sources. SMBH binary is one of the most promising sources for LISA and will be detected with very high signal to noise ratio, $S/N \sim 10^3$ (Bender *et al.* 2000). Since the merging SMBHs events will be detected for extremely high redshift ($z > 5$), the lensing probability is relatively high and hence some lensing events are expected. We consider two cases for lens models: 1) the point mass lens for compact objects (such as black holes), and 2) the SIS (Singular Isothermal Sphere) lens for galaxies, star clusters and CDM (Cold Dark Matter) halos. The wave effects become important for the lens mass $10^6 - 10^9 M_\odot$ which is determined by the LISA band, 10^{-4} to 10^{-1} Hz from Eq.(1.3). The frequency of the gravitational waves from the coalescing SMBH binary chirps so that we could see wave effects for different frequency in the lensed chirp signals.

We calculate the gravitationally lensed waveform using the wave optics for the two lens models: the point mass lens and the SIS. Then, we investigate how accurately we can extract the information on the lens object from the gravitational lensed signals detected by LISA using the Fisher-matrix formalism (e.g. Cutler & Flanagan 1994). Cutler (1998) studied the estimation errors for the merging SMBHs by LISA (see also Vecchio & Cutler 1998; Hughes 2002; Moore & Hellings 2002; Hellings & Moore 2003; Seto 2002; Vecchio 2003). Following Cutler (1998), we calculate the estimation errors especially for the lens mass and the source position. We also calculate the lensing effects on the signal-to-noise ratio. We assume the 1 yr observation before the final merging and consider the lens mass in the

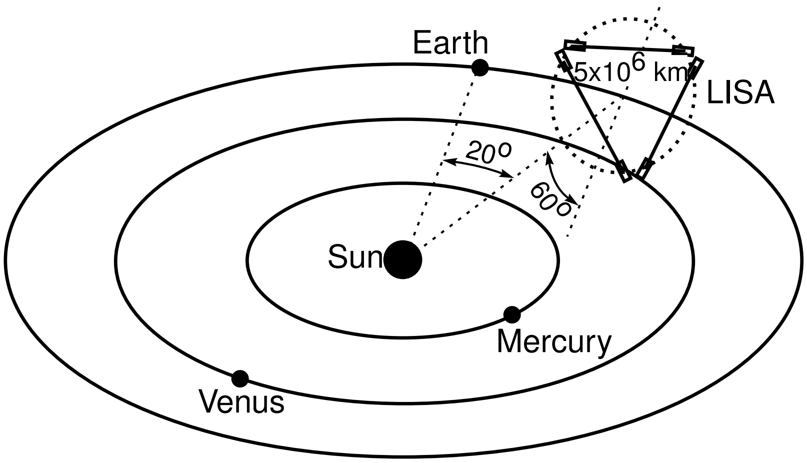

Figure 4.1: Orbital configuration of the LISA antenna. From Hughes (2003).

range $10^6 - 10^9 M_\odot$. Then the typical time delay between the double images is $10 - 10^4$ sec which is much smaller than 1 yr. Throughout this chapter, we assume a $(\Omega_M, \Omega_\Lambda) = (0.3, 0.7)$ cosmology and a Hubble parameter $H_0 = 70 \mathrm{kms}^{-1}\mathrm{Mpc}^{-1}$.

4.1 Gravitationally Lensed Waveform and Parameter Estimation

4.1.1 Gravitational Wave Measurement with LISA

We briefly discuss the gravitational wave measurement with LISA (see Cutler 1998; Bender *et al.* 2000). LISA consists of three spacecrafts forming an equilateral triangle and orbits around the Sun, trailing 20° behind the Earth (see Fig.4.1). The sides of the triangle are $L = 5 \times 10^6$ km in length, and the plane of the triangle is inclined at 60° with respect to the ecliptic. The triangle rotates annually. The gravitational wave signal is reconstructed from three data streams that effectively correspond to three time-varying armlengths $(\delta L_1, \delta L_2, \delta L_3)$. We basically analyze two data streams given by $s_I(t) = [\delta L_1(t) - \delta L_2(t)]/L$ and $s_{II}(t) = [\delta L_1(t) + \delta L_2(t) - 2\delta L_3(t)]/(3)^{1/2} L$. These data can be regarded as the response of two 90° interferometers rotated by 45° to one another (Cutler 1998). The data $s_{I,II}(t)$ contain both gravitational waves signals $h_{I,II}(t)$ to be fitted by matched filtering and noises $n_{I,II}(t)$. The latter is constituted by the detector's noise and binary confusion noise. As in Cutler (1998), we assume that the noises are stationary, Gaussian and uncorrelated with each other.

The gravitational wave signals $h_{I,II}(t)$ from a binary are written as

$$h_{I,II}(t) = \frac{\sqrt{3}}{2} \left[F^{+}_{I,II}(t) h_{+}(t) + F^{\times}_{I,II}(t) h_{\times}(t) \right], \tag{4.1}$$

where $F^{+,\times}_{I,II}(t)$ are the pattern functions which depend on the source's angular position of the binary, its orientation and detector's configuration. The quantities $h_{+,\times}(t)$ are the two polarization modes of gravitational radiation from the binary. The direction and the orientation of the binary and the direction of the lens are assumed to be constant during the observation in a fixed barycenter frame of the solar system. Further discussion and details about the pattern functions are shown in Cutler (1998).

4.1.2 Gravitationally Lensed Signal Measured by LISA

We consider the SMBH binaries at redshift z_S as the sources. We use a restricted post-Newtonian approximation for the in-spiral waveform (Cutler & Flanagan 1994). The coalescing time for circular orbit is typically $t_c = 0.1\text{yr}\,(\mathcal{M}_z/10^6 M_\odot)^{-5/3}$ $\times(f/10^{-4}\text{Hz})^{-8/3}$ where $\mathcal{M}_z = (M_1 M_2)^{3/5}(M_1+M_2)^{-1/5}(1+z_S)$ is the redshifted chirp mass. At the solar system barycenter, the unlensed waveforms $\tilde{h}_{+,\times}(f)$ in the frequency domain are given by

$$\begin{aligned}\tilde{h}_+(f) &= \mathcal{A}\left[1+(\mathbf{L}\cdot\mathbf{n})^2\right] f^{-7/6} e^{i\Psi(f)},\\ \tilde{h}_\times(f) &= -2i\mathcal{A}\,(\mathbf{L}\cdot\mathbf{n})\, f^{-7/6} e^{i\Psi(f)},\end{aligned} \tag{4.2}$$

where $\mathbf{L}$ (given by $\bar{\theta}_L, \bar{\phi}_L$) is the unit vector in the direction of the binary's orbital angular momentum and $\mathbf{n}$ (given by $\bar{\theta}_S, \bar{\phi}_S$) is the unit vector toward the binary. These vectors are defined in a fixed barycenter frame of the solar system. The amplitude $\mathcal{A}$ and the phase $\Psi(f)$ depend on six parameters; the redshifted chirp mass $\mathcal{M}_z$ and reduced mass $\mu_z = M_1 M_2(1+z_S)/(M_1+M_2)$; the spin-orbit coupling constant β; a coalescence time t_c and phase ϕ_c; the angular diameter distance to the source D_S. The amplitude is

$$\mathcal{A} = \sqrt{\frac{5}{96}}\frac{\pi^{-2/3}\mathcal{M}_z^{5/6}}{D_S(1+z_S)^2}. \tag{4.3}$$

where $D_S(1+z_S)^2$ is the luminosity distance to the source. The phase $\Psi(f)$ is given by,

$$\Psi(f) = 2\pi f t_c - \phi_c - \frac{\pi}{4} + \frac{3}{4}\left(8\pi\mathcal{M}_z f\right)^{-5/3}\left[1+\frac{20}{9}\left(\frac{743}{336}+\frac{11\mu_z}{4M_z}\right)x + (4\beta-16\pi)\,x^{3/2}\right], \tag{4.4}$$

where $M_z = (M_1+M_2)(1+z_S)$ is the redshifted total mass, and $x = (\pi M_{t,z} f)^{2/3}$ is the post-Newtonian expansion parameter which is roughly $\mathcal{O}(v^2/c^2)$.

The gravitationally lensed waveforms $\tilde{h}^L_{+,\times}(f)$ in the frequency domain are given by the product of the amplification factor $F(f)$ and the unlensed waveforms $\tilde{h}_{+,\times}(f)$ (see §2):

$$\tilde{h}^L_{+,\times}(f) = F(f)\;\tilde{h}_{+,\times}(f). \tag{4.5}$$

where the function $F(f)$ is given in Eq.(2.32) for the point mass lens and in Eq.(2.36) for the SIS lens. The dimensionless frequency w in these equations (2.32) and (2.36) is related to the frequency f as, $w = 8\pi M_{Lz} f$, where $M_{Lz} = M_L(1+z_L)$ is the redshifted lens mass. We note that the amplification factor $F(f)$ includes the two lens parameters: the redshifted lens mass M_{Lz} and the source position y^1 as discussed in §2.2.1 for the point mass lens and §2.2.2 for the SIS. Using Eq.(4.1),(4.2) and (4.5), the observed lensed signals $\tilde{h}^L_\alpha(f)$ ($\alpha = I, II$) with LISA are given in the stationary phase approximation as,

$$\begin{aligned}\tilde{h}^L_\alpha(f) &= \frac{\sqrt{3}}{2}\frac{D_S\ \xi_0^2\,(1+z_L)}{D_L D_{LS}}\frac{f}{i}\int d^2\mathbf{x}\ \Lambda_\alpha(t+t_d(\mathbf{x},\mathbf{y}))\ e^{-i(\phi_D+\phi_{p,\alpha})(t+t_d(\mathbf{x},\mathbf{y}))} \\ &\quad \times \mathcal{A} f^{-7/6} e^{i\Psi(f)}\ e^{2\pi i f t_d(\mathbf{x},\mathbf{y})}, \end{aligned} \tag{4.6}$$

where

$$\begin{aligned}\phi_{p,\alpha}(t) &= \tan^{-1}\left[\frac{2(\mathbf{L}\cdot\mathbf{n})F_\alpha^\times(t)}{1+(\mathbf{L}\cdot\mathbf{n})^2 F_\alpha^+(t)}\right] \\ \Lambda_\alpha(t) &= \left[(2\ \mathbf{L}\cdot\mathbf{n})^2 F_\alpha^{\times\ 2}(t) + \{1+(\mathbf{L}\cdot\mathbf{n})^2\}^2 F_\alpha^{+\ 2}(t)\right]^{1/2}.\end{aligned}$$

The Doppler phase is

$$\phi_D(t) = 2\pi f(t) R \sin\bar{\theta}_S \cos\left(\bar{\phi}(t) - \bar{\phi}_S\right),$$

where $R = 1$ AU, $\bar{\phi}(t) = 2\pi t/T$ ($T = 1$ yr), and $t = t(f)$ is given by,

$$t(f) = t_c - 5\,(8\pi f)^{-8/3}\mathcal{M}_z\left[1 + \frac{4}{3}\left(\frac{743}{336} + \frac{11\mu_z}{4M_z}\right)x - \frac{32\pi}{5}x^{3/2}\right]. \tag{4.7}$$

In the no lens limit of $|F| = 1$ in Eq.(4.5), the lensed signals $\tilde{h}^L_\alpha(f)$ in Eq.(4.6) agree with the unlensed ones $\tilde{h}_\alpha(f)$ in Cutler (1998). We assume the source position $\mathbf{y}$ is constant during the observation, since the characteristic scale of the interference pattern, $\sim 10^7 \mathrm{AU}(M_{Lz}/10^8 M_\odot)^{-1/2}(f/\mathrm{mHz})^{-1}\ [(D_S D_L/D_{LS})/\mathrm{Gpc}]^{1/2}$, is extremely larger than the LISA's orbital radius (1 AU).

Since the lensed signals $\tilde{h}^L_\alpha(f)$ in Eq.(4.6) are given by double integral, we approximate $\tilde{h}^L_\alpha(f)$ in the two limiting cases; 1) geometrical optics limit ($f \gg t_d^{-1}$) and 2) the time delay being much smaller than LISA's orbital period of ($t_d \ll 1$ yr). In the geometrical optics limit, from Eq.(2.30) we obtain,

$$\tilde{h}^L_\alpha(f) = \frac{\sqrt{3}}{2}\sum_j |\mu_j|^{1/2}\,\Lambda_\alpha(t+t_{d,j}) e^{2\pi i f t_{d,j} - i\pi n_j} e^{-i(\phi_D+\phi_{p,\alpha})(t+t_{d,j})} \times \mathcal{A} f^{-7/6} e^{i\Psi(f)}. \tag{4.8}$$

---

[1] The source position y is defined in Eq.(2.21) and Fig.2.1.

If the time delay is much smaller than LISA's orbital period ($t_d \ll 1$ yr), we expand Λ_α, ϕ_D and $\phi_{p,\alpha}$ around $t_d = 0$ as,

$$\begin{aligned}\tilde{h}^L_\alpha(f) &= \frac{\sqrt{3}}{2}\Lambda_\alpha(t)e^{-i(\phi_D+\phi_{p,\alpha})(t)} \times \mathcal{A}f^{-7/6}e^{i\Psi(f)} \\ &\times \left[F(f) + \frac{d}{dt}\left\{\ln\Lambda_\alpha - i\left(\phi_D+\phi_{p,\alpha}\right)\right\}\frac{f}{2\pi i}\frac{d}{df}\left(\frac{F(f)}{f}\right) + \mathcal{O}\left((t_d/1\mathrm{yr})^2\right)\right]. \quad (4.9)\end{aligned}$$

Since we consider the lens mass $M_{Lz} = 10^6 - 10^9 M_\odot$, the time delay is much smaller than 1 yr. Thus we use the above equation (4.9) as the lensed waveforms for the following calculations.

In Fig.4.2, the lensed signals $|\tilde{h}^L_\alpha(f)|$ ($\alpha = I, II$) and the unlensed ones $|\tilde{h}_\alpha(f)|$ are shown. We show the results from one year before the final merging to the inner most stable circular orbit (the binary separation is $r = 6(M_1 + M_2)$). We set typical parameters at the SMBH binary masses $M_{1,2z} = 10^6 M_\odot$, the lens mass $M_{Lz} = 10^8 M_\odot$ and the source position $y = 1$ for the point mass lens. The angular parameters are $\cos\bar{\theta}_S = 0.3, \bar{\phi}_S = 5.0, \cos\bar{\theta}_L = 0.8, \bar{\phi}_L = 2.0$, and the source redshift is $z_S = 1$ (the angular diameter distance is $H_0 D_S = 0.386$). Therefore the frequency range is from 5×10^{-5} to 2×10^{-3} Hz and the time delay is 4×10^3 sec. The strange behavior in the lower frequency $f \lesssim 10^{-4}$ Hz is due to the LISA's orbital motion. In this frequency region, however, the difference between the lensed signal and the unlensed one is small due to the diffraction (see Fig.2.4). On the other hand, the oscillatory behavior appears in the higher frequency region $f \gtrsim 10^{-4}$ Hz. This critical frequency is determined by the inverse of the lens mass $8\pi M_{Lz}$ (see Fig.2.4). The oscillatory amplitude and the period are determined by the product of the magnifications $2|\mu_+\mu_-|^{1/2} = 2/(y\sqrt{y^2+4})$ and the inverse of the time delay, $1/\Delta t_d$ (see the third term of Eq.(2.34)).

4.1.3 Parameter Extraction

We briefly mention the matched filtering analysis and the parameter estimation errors (Finn 1992; Cutler & Flanagan 1994). We assume that the signal $\tilde{h}^L_\alpha(f)$ is characterized by some unknown parameters γ_i. In the present case, there are ten source parameters ($\mathcal{M}_z$, μ_z, β, ϕ_c, t_c, D_S, $\bar{\theta}_S$, $\bar{\phi}_S$, $\bar{\theta}_L$, $\bar{\phi}_L$) and two lens parameters (M_{Lz}, y). In the matched filtering analysis the variance-covariance matrix of the parameter estimation error $\Delta\gamma_i$ is given by inverse of the Fisher information matrix Γ_{ij} as $\langle\Delta\gamma_i\Delta\gamma_j\rangle = (\Gamma^{-1})_{ij}$. The Fisher matrix becomes

$$\Gamma_{ij} = 4\sum_{\alpha=I,II}\mathrm{Re}\int\frac{df}{Sn(f)}\frac{\partial\tilde{h}^{L*}_\alpha(f)}{\partial\gamma_i}\frac{\partial\tilde{h}^L_\alpha(f)}{\partial\gamma_j}, \quad (4.10)$$

where $Sn(f)$ is the noise spectrum. The noise spectrum $Sn(f)$ is the sum of the instrumental and the confusion noise, and we adopt the same noise spectrum as

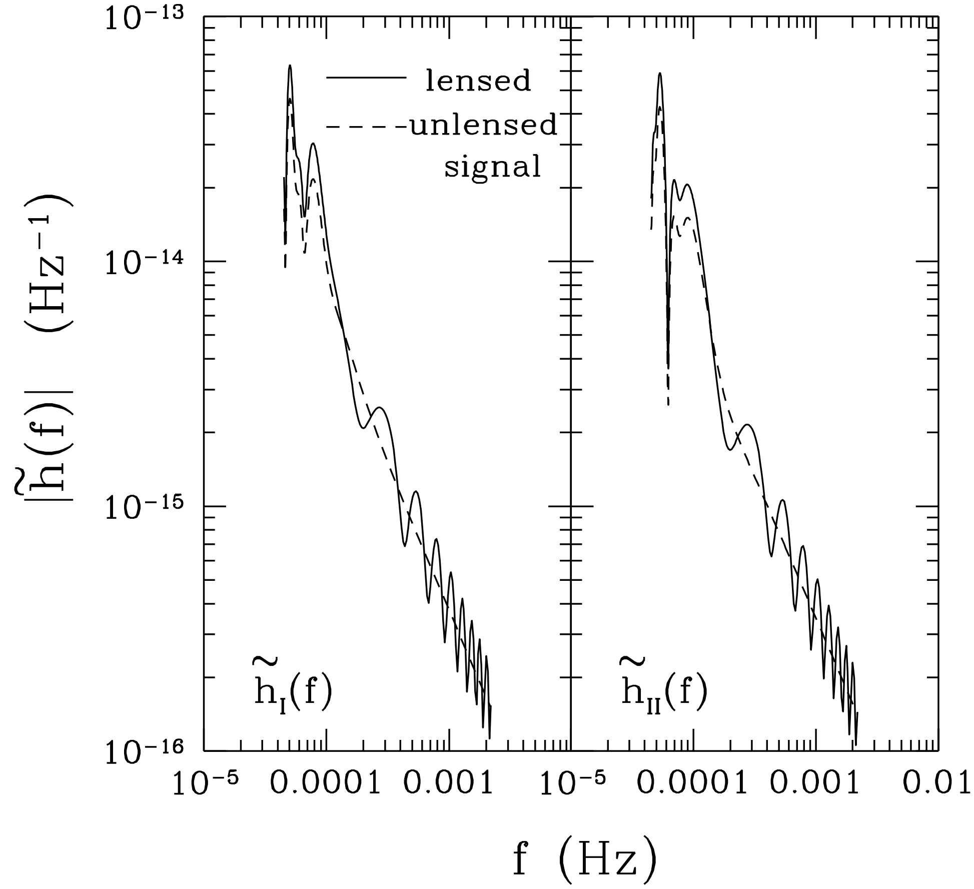

Figure 4.2: The lensed signals $|\tilde{h}^L_\alpha(f)|$ ($\alpha = I, II$) (solid line) and unlensed ones $|\tilde{h}_\alpha(f)|$ (dashed line) measured by LISA. The signals are shown from 1yr before coalescence to ISCO of $r = 6(M_1+M_2)$. The redshifted masses of the SMBH binary is $M_{1,2z} = 10^6 M_\odot$, the redshifted lens mass is $M_{Lz} = 10^8 M_\odot$ and the source position $y = 1$. The angular parameters are $\cos\bar{\theta}_S = 0.3, \bar{\phi}_S = 5.0, \cos\bar{\theta}_L = 0.8, \bar{\phi}_L = 2.0$, and the source redshift is $z_S = 1$ (distance is $H_0 D_S = 0.386$). The strange behavior for $f \lesssim 10^{-4}$ Hz is due to the LISA orbital motion, and the difference between the two signals is small due to the diffraction. On the other hand, the oscillatory behavior appears for $f \gtrsim 10^{-4}$ Hz which is determined by the inverse of the lens mass $8\pi M_{Lz}$ (see Fig.2.4). This oscillation is due to the interference between the double images.

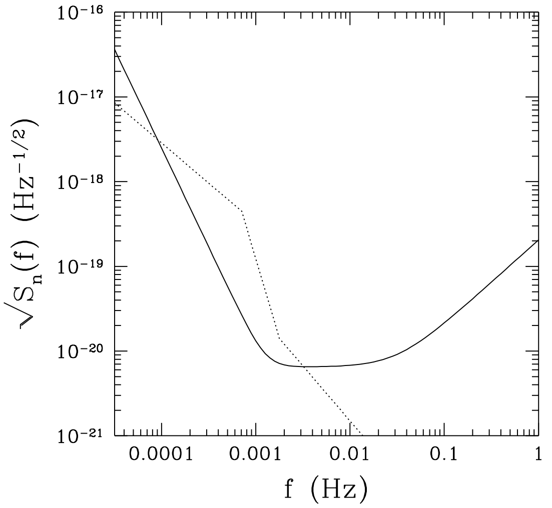

Figure 4.3: The noise spectrum for LISA. The solid line is the instrumental noise, and the dotted line is the confusion noise. The total noise is the sum of them.

that in Cutler (1998). We show $Sn(f)$ in Fig.4.3, and the solid (dotted) line is instrumental (confusion) noise. The signal to noise ratio (S/N) is given by

$$(S/N)^{\,2} = 4 \sum_{\alpha=I,II} \int \frac{df}{Sn(f)} \left| \tilde{h}^L_\alpha(f) \right|^2 . \tag{4.11}$$

We computed the variance-covariance matrix Γ_{ij} for a wide range of the lens parameters (M_{Lz}, y), using the lensed waveform in Eq.(4.9). Since the S/N is very high for the SMBH merger, the Fisher matrix approach to calculate the estimation errors is valid (Cutler 1998). We integrate gravitational lensed waveform (in Eq.(4.10) and Eq.(4.11)) from 1 yr before the final merging to the cut-off frequency f_{cut} when the binary separation becomes $r = 6(M_1 + M_2)$. Then, the initial frequency is given by,

$$f_{init} = 4.1 \times 10^{-5} \left(\frac{\mathcal{M}_z}{10^6 M_\odot} \right)^{-5/8} \ \mathrm{Hz}, \tag{4.12}$$

and the cut-off frequency is

$$f_{cut} = 4.4 \times 10^{-3} \left(\frac{M_{1z} + M_{2z}}{10^6 M_\odot} \right)^{-1} \ \mathrm{Hz}. \tag{4.13}$$

4.2 Results

In this section, we present numerical results to compute the signal to noise ratio (S/N) and the errors in estimation parameters. We randomly distribute 100 binaries over various directions and orientations on celestial spheres at $z_S = 1$ (the distance is $H_0 D_S = 0.386$). We present the mean value averaged for 100 binaries.

4.2.1 Lensing Effects on the Signal to Noise Ratio

We demonstrate the gravitational lensing effect on the signal to noise ratio (S/N). In Fig.4.4, the increasing factor of S/N by the gravitational lensing for the point mass lens is shown for the fixed source position[2] $y = 0.1, 0.3, 1,$ and 3 as a function of the lens mass M_{Lz}. The vertical axis is the S/N with the gravitational lensing divided by the unlensed S/N. Four panels are shown for the various SMBH binary masses $M_{1,2z} = 10^4, 10^5, 10^6,$ and $10^7 M_\odot$. We only show the mean value averaged for 100 binaries, but the dispersion is negligibly small (less than 5 %). For the lens mass smaller than $10^6 M_\odot$ the magnification is very small irrespective of the SMBH binary masses due to the diffraction effects. In this case the Schwarzschild radius of the lens mass M_{Lz} is smaller than the wavelength of gravitational waves $\lambda \sim 1$ AU, and the waves are not magnified by lensing. This critical lens mass ($10^6 M_\odot$) is mainly determined by the inverse of the knee frequency of the LISA's noise spectrum, $1/(8\pi f) \sim 8 \times 10^6 M_\odot (f/\mathrm{mHz})^{-1}$ (see Fig.2.4). But for $10^7 + 10^7 M_\odot$, the SMBH binary coalescences at the lower frequency ($f \sim 10^{-4}$ Hz), thus the critical lens mass is shifted for a larger mass ($10^7 M_\odot$) as shown in the right bottom panel of Fig.4.4. This tells us that if the lens mass is smaller than $10^6 M_\odot$, the effect of the lens is very small. If the lens mass is larger than $10^7 M_\odot$, the damped oscillatory behavior appears due to the interference between the two images, and the S/N converges to the geometrical optics limit, $|\mu|^{1/2} = (y^2+2)^{1/2}/[y^{1/2}(y^2+4)^{1/4}]$, which is independent of the lens mass. As y increases from 0.1 (solid line) to 3 (dashed line), the amplification decreases since the magnifications of the two images ($|\mu_\pm(y)|$) decrease as y increases (see also Fig.2.4).

Fig.4.5 is the same as Fig.4.4, but for the SIS lens model. The behavior is very similar to that in the point mass lens. For the lens mass larger than $10^7 M_\odot$, the S/N converges to the geometrical optics limit, $|\mu|^{1/2} = (2/y)^{1/2}$ for $y \leq 1$ and $|\mu|^{1/2} = (1 + 1/y)^{1/2}$ for $y \geq 1$. As y increases from 0.1 (solid line) to 3 (dashed line), the amplification decreases (see also Fig.2.5).

4.2.2 Parameter Estimation for the Lens Objects

In this section, we show the parameter estimation for the lens objects. We show the results for the SMBH binary with masses $10^6 + 10^6 M_\odot$, because we found S/N is higher than the other binary masses ($M_{1,2z} = 10^4, 10^5$ and $10^7 M_\odot$). We distribute

---

[2] The source position y is defined in Eq.(2.21), and see also Fig.2.1.

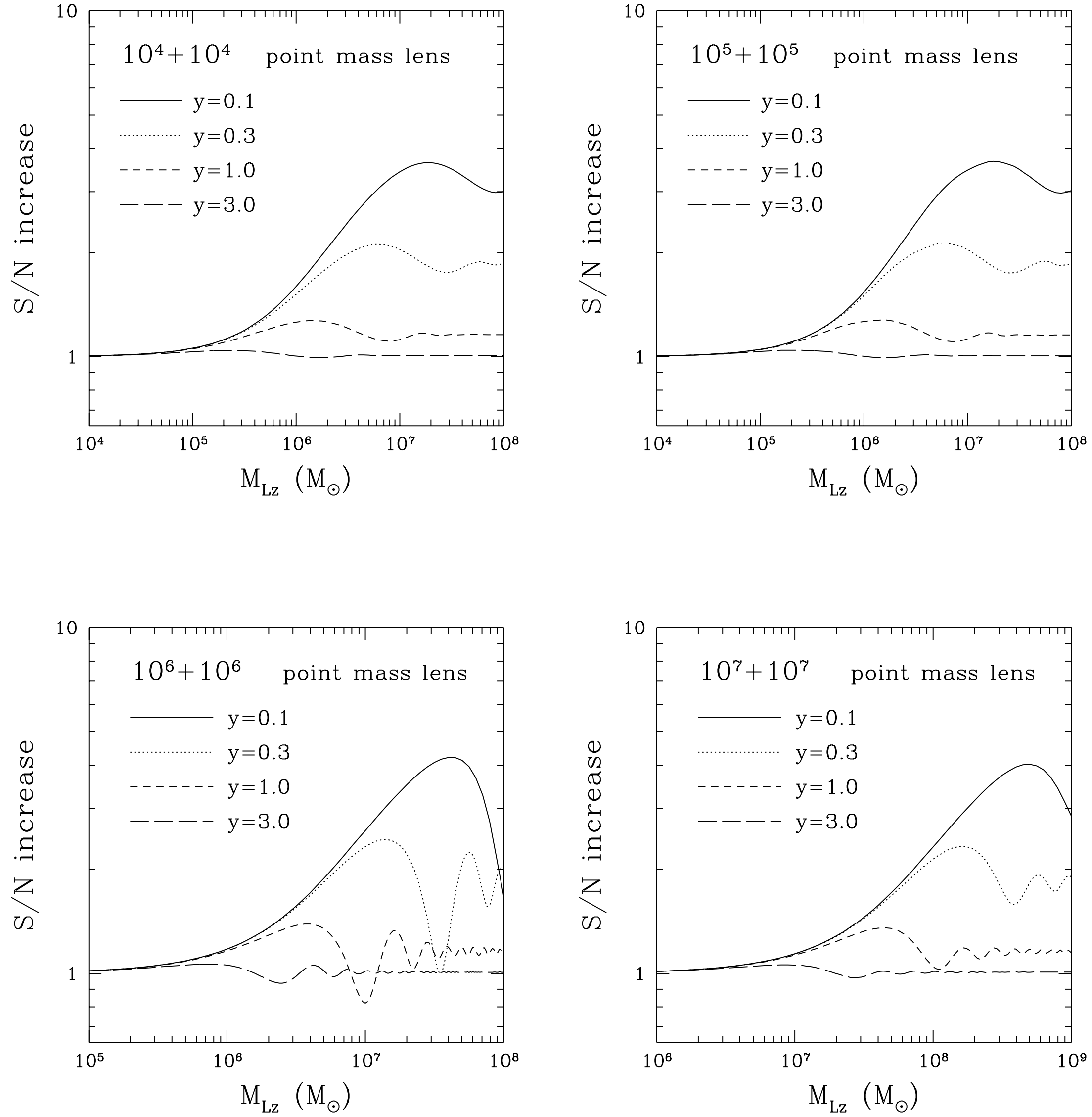

Figure 4.4: The increasing factor in S/N due to the gravitational lensing by the point mass lens for the various SMBH binary masses $M_{1,2z} = 10^4, 10^5, 10^6$, and $10^7 M_\odot$. The horizontal axis is the redshifted lens mass; the vertical axis is the lensed S/N divided by the unlensed S/N. The source position is fixed at $y = 0.1, 0.3, 1$, and 3. For $M_{Lz} \lesssim 10^6 M_\odot$, the magnification is very small due to the diffraction effect irrespective of the SMBH binary masses. For $M_{Lz} \gtrsim 10^7 M_\odot$, the damped oscillatory patterns appear due to the interference between the two images, and this behavior converge in the geometrical optics limit, $|\mu|^{1/2} = (y^2 + 2)^{1/2}/[y^{1/2}(y^2+4)^{1/4}]$.

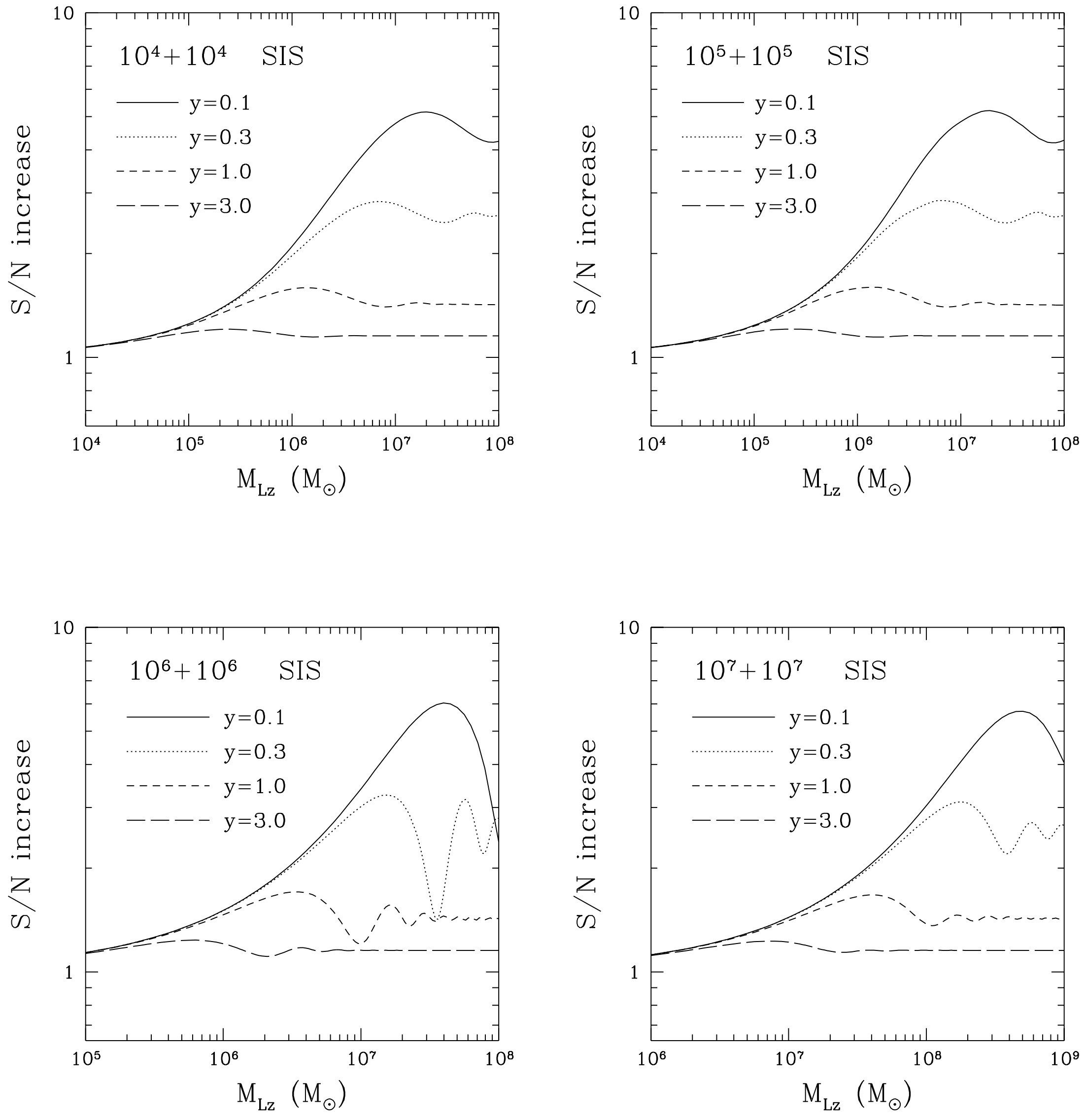

Figure 4.5: Same as Fig.4.4, but for the SIS lens model. For $M_{Lz} \gtrsim 10^7 M_\odot$, the results converge in the geometrical optics limit, $|\mu|^{1/2} = (2/y)^{1/2}$ for $y \leq 1$ and $|\mu|^{1/2} = (1 + 1/y)^{1/2}$ for $y \geq 1$.

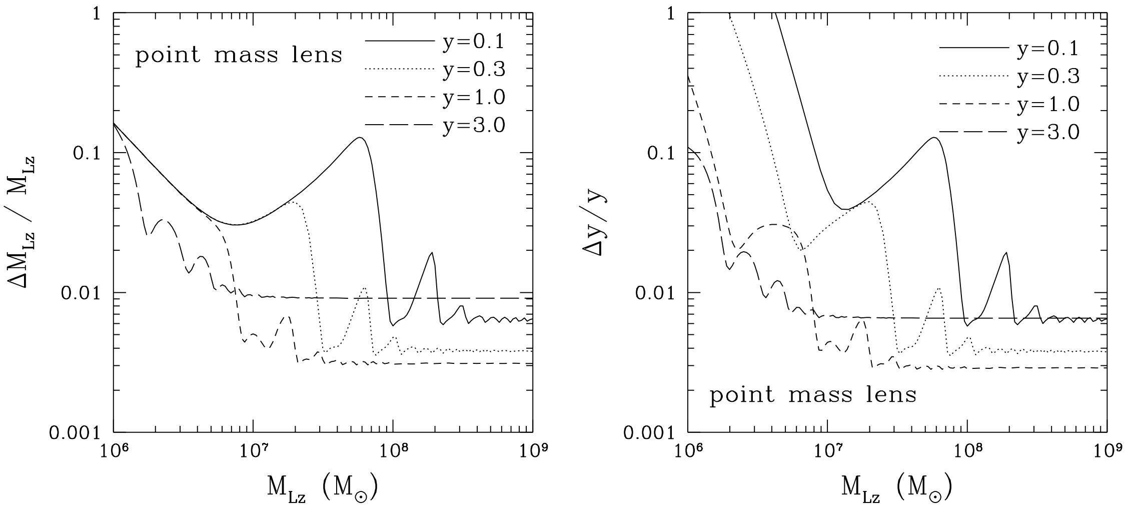

Figure 4.6: The estimation errors for the redshifted lens mass ΔM_{Lz} (left panel) and the source position Δy (right panel) for the point mass lens. The results are presented for the SMBH binary of masses $10^6 + 10^6 M_\odot$ at $z_S = 1$. The errors are normalized by $S/N = 10^3$ and simply scale as $(S/N)^{-1}$. For $M_{Lz} \lesssim 10^7 M_\odot$ the errors are relatively large, since the effect of lensing is very small due to the diffraction. For $M_{Lz} \gtrsim 10^8 M_\odot$ the geometrical optics approximation is valid, and errors converge to constants.

the 100 binaries over the various directions and the orientations at $z_S = 1$, and the mean value of the S/N without lensing is 2600 in these 100 binaries. We show the mean value of errors averaged for 100 binaries, for $M_{Lz} \lesssim 10^7 M_\odot$ the dispersion is relatively large ($\lesssim 40\%$), but for $M_{Lz} \gtrsim 10^7 M_\odot$ the results converge to that in the geometrical optics limit and the dispersion is negligibly small.

In Fig.4.6, the estimation errors for the redshifted lens mass ΔM_{Lz} (left panel) and the source position Δy (right panel) are shown as a function of M_{Lz} with $y = 0.1, 0.3, 1,$ and 3 for the point mass lens. We use the units of $S/N = 10^3$, and the results (ΔM_{Lz}, Δy) scale as $(S/N)^{-1}$. For $M_{Lz} \lesssim 10^7 M_\odot$ the estimation errors are relatively large $\gtrsim 10\%$, since the effect of lensing on the signals is very small due to the diffraction. For $M_{Lz} \gtrsim 10^8 M_\odot$ the geometrical optics approximation is valid, and the errors converge to a constant in Fig.4.6. The redshifted lens mass and the source position can be determined up to the accuracy of $\sim 0.1\%$, as shown in Fig.4.6. The errors in the geometrical optics limit are well fitted by (see the Appendix D),

$$\frac{\Delta M_{Lz}}{M_{Lz}} = \frac{1}{S/N} \times \frac{\sqrt{y(y^2+2)}(y^2+4)^{5/4}}{2\tau},$$

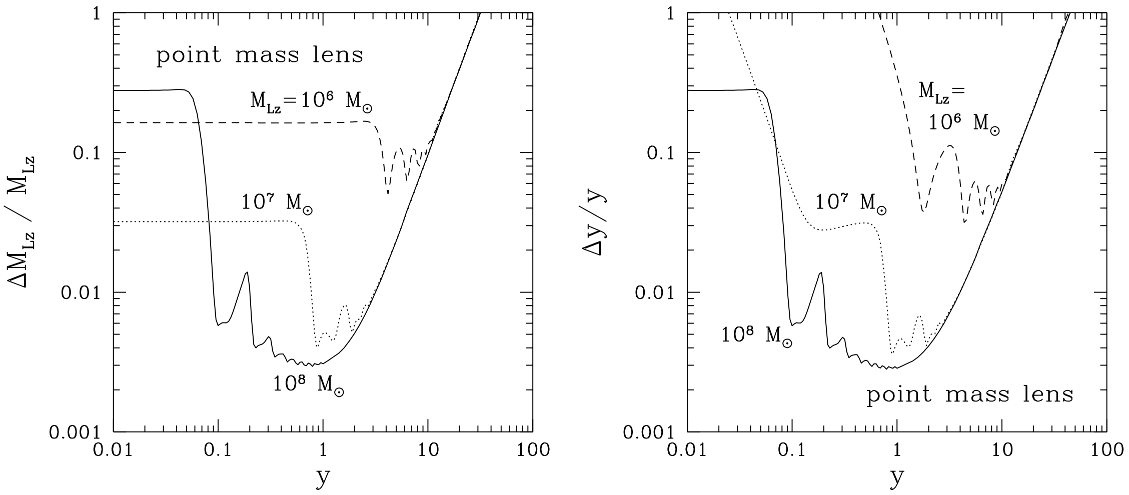

Figure 4.7: Same as Fig.4.6, but as a function of y. We note that even for $y \gtrsim 10$ we can extract the lens information. Then the lensing cross section ($\propto y^2$) increases an order of magnitude larger than that for the usual strong lensing of light ($y = 1$).

$$\frac{\Delta y}{y} \;=\; \frac{1}{S/N} \times \frac{\sqrt{y^2+2}(y^2+4)^{3/4}}{2\sqrt{y}}, \tag{4.14}$$

where S/N is in the unlensed case, and $\tau = \Delta t_d/4M_{Lz} = y\sqrt{y^2+4}/2 + \ln((\sqrt{y^2+4}+y)/(\sqrt{y^2+4}-y))$. Thus, one could determine the lens parameters, the redshifted lens mass and the source position, up to the accuracy of $\sim (S/N)^{-1}$. The above equations (4.14) are valid if the time delay Δt_d is much smaller than the LISA's orbital period 1 yr. If the time delay Δt_d becomes comparable to 1 yr, the LISA's orbital motion affects the results.

Fig.4.7 is the same as Fig.4.6, but as a function of y. For $y \gtrsim 1$, the errors are convergent to the geometrical optics limit of Eq.(4.14) irrespective of the lens mass. As y increases, the time delay t_d increases, and the geometrical optics limit ($ft_d \gg 1$) is valid. We note that even for $y \gtrsim 10$ one can extract the lens information. For light the observable is the lensed flux which is proportional to the magnifications, $\propto |\mu_\pm|$, while for gravitational waves the observable is the lensed amplitude which is proportional to the square root of the magnifications, $\propto |\mu_\pm|^{1/2}$. Thus, it is possible to detect the faint image $|\mu| \ll 1$ by the gravitational waves. For example, let us consider the case where the flux ratio of a brighter image to a fainter one is 100 : 1. Then the amplitude ratio is 10 : 1 so that the fainter image can be observed even if the source position is far from the Einstein radius in the case of gravitational waves. Denoting the largest source position for which one can extract the lens parameters as y_{cr}, we approximate the errors in Eq.(4.14) for the

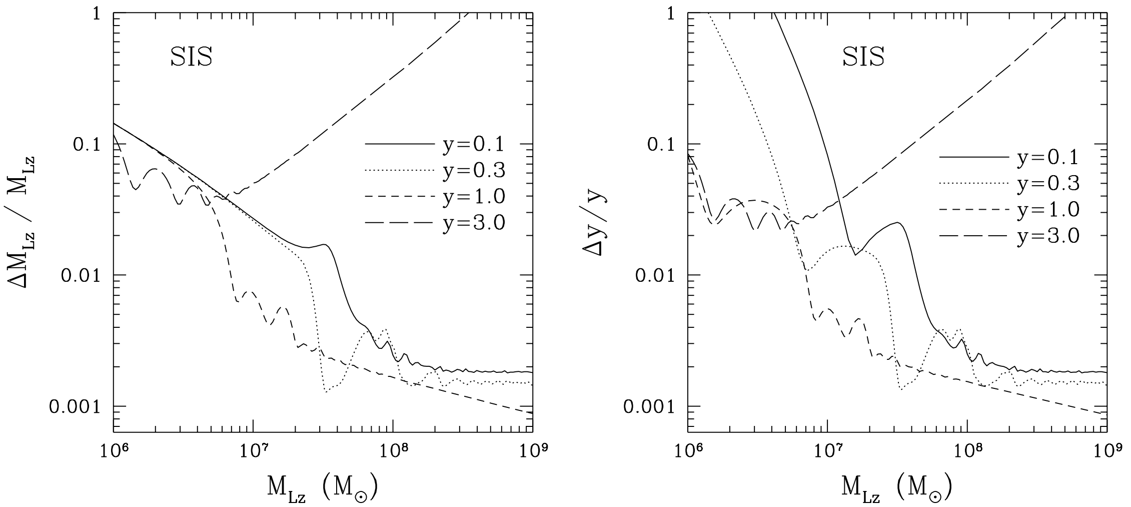

Figure 4.8: The estimation errors for the redshifted lens mass ΔM_{Lz} (left) and the source position Δy (right) for the SIS model. The results are presented for the SMBH binary of masses $10^6 + 10^6 M_\odot$ at $z_S = 1$. The errors are normalized by $S/N = 10^3$ and simply scale as $(S/N)^{-1}$. Even for $y = 3$ (a single image is formed in the geometrical optics limit), the lens parameters can be extracted at $M_{Lz} \sim 10^6 - 10^8 M_\odot$ due to the wave effects.

large y limit; $\Delta\gamma/\gamma \simeq (S/N)^{-1} y^2$, where $\gamma = M_{Lz}, y$. Then we obtain

$$y_{cr} \simeq 10 \left(\frac{\Delta\gamma/\gamma}{0.1}\right)^{1/2} \left(\frac{S/N}{10^3}\right)^{1/2}. \tag{4.15}$$

Thus the lensing cross section ($\propto y_{cr}^2$) increases an order of magnitude larger than that for the usual strong lensing of light ($y_{cr} = 1$) (e.g. Turner, Ostriker & Gott 1984).

In Fig.4.8, the estimation errors for the SIS model are shown. For $M_{Lz} \lesssim 10^7 M_\odot$ the behavior is similar for the point mass lens. But for $M_{Lz} \gtrsim 10^8 M_\odot$ the behavior strongly depends on y. The errors in the quasi-geometrical optics approximation are well fitted by (see the Appendix D),

$$\frac{\Delta M_{Lz}}{M_{Lz}} = \frac{\Delta y}{y} = \frac{1}{S/N} \times \frac{2\sqrt{1-y^2}}{2y+1}, \tag{4.16}$$

for $y < 1$. We note that even for $y = 3$ the lens parameters can be extracted for $M_{Lz} \sim 10^6 - 10^8 M_\odot$ as shown in Fig.4.8. This is because the diffracted image is newly formed at the lens center by the wave effects (see the discussion §4.3). Hence the double images are formed even for $y > 1$, and the information on the lens can be extracted. The errors for $y > 1$ are given in the quasi-geometrical

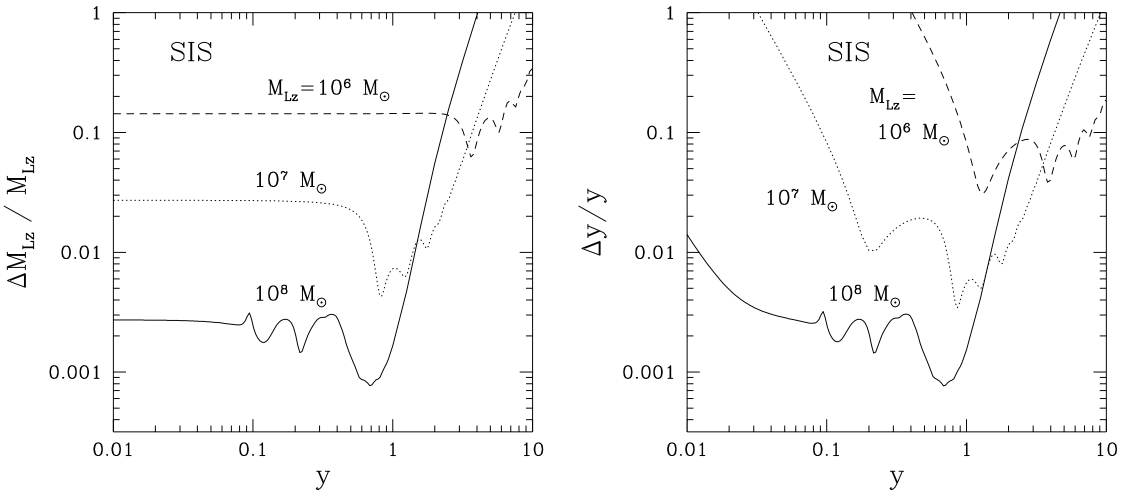

Figure 4.9: Same as Fig.4.8, but as a function of y. We note that even for $y > 1$ we can determine the lens parameters. Then the lensing cross section ($\propto y^2$) becomes larger than that in the geometrical optics approximation ($y = 1$).

optics approximation as (see the Appendix D),

$$\frac{\Delta M_{Lz}}{M_{Lz}} = \frac{1}{S/N} \times \frac{32\pi y(y-1)^2\sqrt{y^2-1}}{2y+1} M_{Lz}\langle f\rangle, \qquad (4.17)$$

$$\frac{\Delta y}{y} = \frac{1}{S/N} \times \frac{16\pi (y^2-1)^{3/2}(y-1)}{2y+1} M_{Lz}\langle f\rangle, \qquad (4.18)$$

where $\langle f\rangle$ is defined by,

$$\langle f\rangle^2 = (S/N)^2 \times \left[4 \sum_{\alpha=I,II} \int \frac{df}{Sn(f)} \left|\frac{\tilde{h}_\alpha^L(f)}{f}\right|^2\right]^{-1},$$

and the mean value of $\langle f\rangle$ averaged for 100 binaries is 1.2 mHz. For $y = 1$, the errors decrease as lens mass increases as shown in Fig.4.8, because the errors converge to the results in the quasi-geometrical optics limit of Eq.(4.16) - (4.18) which vanish at $y = 1$. As a result, if $y > 1$, the errors asymptotically increase with the increase of the lens mass, but if $y < 1$, they asymptotically converge to constants.

Fig.4.9 is the same as Fig.4.8, but as a function of y. We note that even for larger $y \gtrsim 1$ we can extract the lens information. Thus the lensing probability ($\propto y^2$) to determine the lens parameters increases as compared with the results in geometrical optics limit for the lens objects in the mass range $10^6 - 10^8 M_\odot$.

4.2.3 Lensing Effects on the Estimation Errors of the Binary Parameters

We discuss the gravitational lensing effects on the estimation errors of the SMBH binary parameters. We study five binary parameters; the redshifted chirp mass $\mathcal{M}_z$, the reduced mass μ_z, the distance to the source D_S and the angular resolution $(\bar{\theta}_S, \bar{\phi}_S)$. We find that the estimation errors of these parameters decrease because S/N increases by lensing (see Fig.4.4 and 4.5). The error $\Delta\gamma$ is roughly proportional to the inverse of the S/N as $\Delta\gamma \propto (S/N)^{-1}$ (see Eq.(4.10) and (4.11)).

4.2.4 Results for Various SMBH Masses and Redshifts

So far we presented the results for equal mass SMBH binaries with redshift $z_S = 1$. In this section, we comment on the results for the case of various (unequal) SMBH masses $10^4 - 10^7 M_\odot$ and redshifts $z_S = 1 - 10$.

The critical lens mass in which the wave effects become important $(10^6 - 10^8 M_\odot)$ is mainly determined by the inverse of the knee frequency of the LISA's noise spectrum, $\sim 8 \times 10^6 M_\odot \ (f/\mathrm{mHz})^{-1}$, independent of the binary mass. But for the massive total mass binary $(M_{1z} + M_{2z}) \gtrsim 10^7 M_\odot$, the binary coalescences at the lower frequency $(\sim 10^{-4}\mathrm{Hz})$, thus the critical lens mass is shifted for larger mass $(10^7 - 10^9 M_\odot)$. For the larger lens mass $M_{Lz} \gtrsim 10^8 M_\odot$, the results (the S/N increase and the estimation errors) converge to that in the geometrical optics limit irrespective of the binary mass. The estimation errors in Fig.4.6-4.9 are the case of $10^6 - 10^6 M_\odot$ binary at redshift $z_S = 1$ and are normalized to $S/N = 10^3$ and simply scale as $(S/N)^{-1}$. In order to translate the results into the various unequal SMBH binaries, we present the S/N for binary masses $M_{1,2z} = 10^4 - 10^7 M_\odot$ with redshifts $z_S = 1, 3, 5, 10$ in Table.4.1. We assume 1 yr observation of in-spiral phase before final merging. The results are the mean value of 100 binaries which are randomly distributed at each redshift, and the dispersion is relatively large $\sim 50\%$. From Table 4.1, one could translate the results in Fig.4.6-4.9 into errors in real situations.

We also comment on the results for the case with only h_I data available, as opposed to the combination of h_I and h_{II} data that we used. In this case, the S/N increase in Fig.4.4 and 4.5 is not changed, but the estimation errors are slightly larger ($\sim 30\%$) than that in Fig.4.6-4.9 for $M_{Lz} \lesssim 10^7 M_\odot$ if the errors are normalized to $S/N = 10^3$. We note that the S/N is $\sqrt{2}$ times smaller than that in the case of the two data available in Table 4.1.

4.3 Lensing Event Rate

We discuss the event rate of merging SMBHs and estimate the lensing probability and the lensing event rate. The expected rate of merging SMBHs detected by LISA is in the range $0.1 - 10^2$ events per year (Haehnelt 1994,1998). Recently, Wyithe

Binary Masses ($M_\odot$)	$z_S = 1$	$z_S = 3$	$z_S = 5$	$z_S = 10$
$10^7 + 10^7$	1038	270	147	66
$10^7 + 10^6$	519	135	74	33
$10^7 + 10^5$	175	46	25	11
$10^7 + 10^4$	52	14	7	3
$10^6 + 10^6$	2575	669	365	164
$10^6 + 10^5$	1517	394	215	97
$10^6 + 10^4$	508	132	72	32
$10^5 + 10^5$	877	228	124	56
$10^5 + 10^4$	310	81	44	20
$10^4 + 10^4$	132	34	19	8

Table 4.1: The signal to noise ratio (S/N) for the various binary masses $10^4 - 10^7 M_\odot$ with redshift $z_S = 1, 3, 5, 10$. We assume 1 yr observation of in-spiral phase before final merging.

& Loeb (2003) suggested that some hundreds detectable events per year could be expected, considering the merger rate at exceedingly high redshift ($z > 5 - 10$). Thus we take $\sim$ 300 events per year as the merging event rate.

We consider the lens objects distributed over the universe and calculate the lensing probability for each lens model. For the point mass lens, we take the compact objects ($10^6 - 10^9 M_\odot$) such as black holes as lens. Denoting the mass density parameter of compact objects as $\Omega_{\rm CO}$, the lensing probability for a source at redshift z_S is (Schneider, Ehlers & Falco 1992),

$$P(z_S) = \frac{3}{2}\Omega_{\rm CO} y_{cr}^2 \int_0^{z_S} dz_L \frac{(1+z_L)^2}{H(z_L)/H_0} \frac{H_0 D_{LS}(z_L, z_S)\ H_0 D_L(z_L)}{H_0 D_S(z_S)}, \tag{4.19}$$

where $H(z)$ is the Hubble parameter at redshift z. The cosmological abundance of the compact objects in the mass range $10^6 - 10^9 M_\odot$ is limited by $\Omega_{\rm CO} \le 0.01$ by the search for multiple images in radio sources (Wilkinson *et al.* 2001; see also Nemiroff *et al.* 2001). In Table 4.2, we show the upper limit on the lensing probability for the point mass lens. Since we set $y_{cr} = 10$ (Eq.(4.15)), the lensing probability is one hundred times larger than that normally assumed for the strong lensing of light ($y_{cr} = 1$). As shown in Table 4.2, the upper limit of the lensing probability is very high (almost 1) and is typically $\sim (\Omega_{\rm CO}/10^{-2})$. The lensing event rate is the product of the merging rate ($\sim$ 300 per year) and the lensing probability, so that the lensing events will be 1 event per year if $\Omega_{\rm CO} = 10^{-4}$.

For the SIS model we take CDM halos ($10^6 - 10^9 M_\odot$) as the lens objects (e.g.

Lens Model	$z_S = 1$	$z_S = 3$	$z_S = 5$	$z_S = 10$
Point mass lens	< 0.21	< 1.1	< 2.0	< 3.9
SIS	7.2×10^{-5}	8.1×10^{-4}	2.0×10^{-3}	4.7×10^{-3}

Table 4.2: The lensing probability by the lens mass in the range $10^6 - 10^9 M_\odot$ with the source redshift $z_S = 1, 3, 5, 10$. For the point mass lens, we give the upper limit which is determined by the observational constraint on the abundance of the compact objects. When the lensing probability is more than one, the lensing occurs sometimes. For the SIS, CDM halos are assumed to be lenses. The presented values are for the case of $S/N = 10^3$, and hence the results are somewhat overestimated for the binaries of $S/N < 10^3$ in Table 4.1. If the expected rate of merging SMBHs is ~ 300 per year (Wyithe & Loeb 2003), then the lensing events will be detected 1 event per year.

Narayan & White 1988). The lensing probability is

$$P(z_S) = \pi y_{cr}^2 \int_0^{z_S} dz_L \frac{(1+z_L)^2}{H(z_L)/H_0} \frac{H_0 D_{LS}(z_L, z_S)\ H_0 D_L(z_L)}{H_0 D_S(z_S)} \int_{10^6 M_\odot}^{10^9 M_\odot} dM_L v N_v(v, z_L), \tag{4.20}$$

where N_v is the comoving number density of the lens and is assumed to be given by the Press-Schechter velocity function (Press & Schechter 1974) with $\sigma_8 = 1$. In Table 4.2, we show the lensing probability for the SIS model. We set $y_{cr} = 3$ (see Fig.4.8) and hence the lensing probability is almost ten times larger than that for light ($y_{cr} = 1$). As shown in Table 4.2, the lensing probability is typically $\sim 10^{-4} - 10^{-3}$. The merger rate is ~ 300 events per year at high redshift ($z > 5$), then the lensing events would be 1 event per year.

We note that the results in Table 4.2 are for the case of the $S/N = 10^3$, and are somewhat overestimated for the binaries of $S/N < 10^3$ in Table 4.1. For example, the lensing probability is proportional to (S/N) from Eq.(4.15) for the point mass lens, and it is appropriate to use $y_{cr} = 1$ for $S/N < 10^3$ in the SIS. In the case of the high event rate (~ 300 events/year), many fainter signals ($S/N \ll 10^3$) are expected, and the errors in Fig.4.6-4.9 are worse for these binaries.

Next, we discuss how we can identify the lensing signal. If the lensing event occurs, the amplitude and the arrival time of the gravitational waves are changed by lensing. But the other features (such as binary mass) are not changed. Thus, if the two signals have the same binary parameters (such as chirp mass) except for the amplitude and the arrival time, that would be a signature of gravitational lensing in the geometrical optics limit. More generally, oscillatory behavior in the waveform $|\tilde{h}^L(f)|$ is a signature of gravitational lensing (see Fig.4.2). However it will be difficult to identify the source and the lens objects in the sky, since the angular resolution of the LISA is ~ 1 deg (see Cutler 1998). Furthermore, the gravitational wave amplitude is changed by the lensing magnification and hence one must assume the lens model in order to determine the distance to the source. (Effect of lensing on measuring the distance is recently discussed in Holz & Hughes (2002).) As one determines the distance to the source $D_S(z_S)$, The redshift $z_S(D_S)$ could be determined if the distance to the source $D_S(z_S)$ could be measured assuming the cosmological parameters (see Hughes 2002).

Chapter 5

Summary

In this thesis, we discussed the wave optics in gravitational lensing of gravitational waves and its application to the gravitational wave observations in the near future.

We review the wave optics in the gravitational lensing, which is more fundamental than the geometrical optics, in §2. If the wavelength λ of the gravitational waves is larger than the Schwarzschild radius of the lens mass M_L, the wave optics should be used. In the short wavelength limit $\lambda \to 0$, the wave optics is reduced to the geometrical optics limit. We use the diffraction integral formula to obtain the gravitationally lensed waveform. We show the wave optics for the various lens models: the point mass lens, the SIS model, the NFW model, and the binary lens.

In §3, we studied the gravitational lensing in the quasi-geometrical optics approximation which is the geometrical optics including the corrections arising from the effects of the finite wavelength. Theses correction terms can be obtained analytically by the asymptotic expansion of the diffraction integral in powers of the wavelength λ. The first term, arising from the short wavelength limit $\lambda \to 0$, corresponds to the geometrical optics limit. The second term, being of the order of λ/M_L (M_L is the Schwarzschild radius of the lens), is the first correction term arising from the diffraction effect. By analyzing this correction term, we obtain the following results:

- The lensing magnification μ is modified to $\mu(1+\delta)$, where δ is of the order of $(\lambda/M_L)^2$.
- If the lens has cuspy (or singular) density profile at the center $\rho(r) \propto r^{-\alpha}$ $(0 < \alpha \leq 2)$ the diffracted image is formed at the lens center with the magnification $\mu \sim (\lambda/M_L)^{3-\alpha}$. Thus if we observe this diffracted image by the various wavelength (e.g. the chirp signal), the slope α can be determined.

In §4, we discussed the gravitational lensing of gravitational waves from chirping binaries. The SMBH binary is taken as the source detected by LISA, and the two simple lens models are considered: the point mass lens and the SIS model. We calculate the lensing effects on the signal to noise ratio (S/N) and how accurately the information of the lens object, its mass, can be extracted from the lensed signal. As expected, for the lens mass smaller than $10^8 M_\odot$, the wave effects are very important to calculate the S/N and the errors in the estimation parameters. We obtain the following results:

- For the lens mass smaller than $10^6 M_\odot$ the signals are not magnified by lensing due to the diffraction effect. For the lens mass larger than $10^8 M_\odot$ the lens parameters can be determined within (very roughly) $\sim 0.1\%$ $[(S/N)/10^3]^{-1}$.
- The lensing cross section to determine the lens parameters is order of magnitude larger than that for light.

Cutler & Thorne (2003) suggest that the mergers of compact binaries will be detected before $\sim$ 2010 or sooner by the ground based interferometers. This is because in about 2007 the first generation interferometers (TAMA300, LIGO, VIRGO, GEO) will be upgraded to produce the second generation detectors (advanced LIGO, LCGT), and the neutron star mergers will be detected by these upgraded detectors. The space interferometer LISA will be launched in $\sim$ 2011. There are some known Galactic binaries which LISA is guaranteed to observe. The mergers of SMBHs are also some of the promising candidates. Furthermore, the space interferometer DECIGO/BBO is planed to construct in $\sim$ 2020, and will detect $\sim 10^5$ events yr^{-1} of the neutron star mergers. Hence, the gravitational wave astronomy will be established at the broad frequency band in the near future, and the lensing events will also be expected for these various detectors.

Acknowledgements

I would like to thank Prof. Takashi Nakamura for variable discussion and encouragement. We would like to thank Takeshi Chiba, Naoki Seto and Kazuhiro Yamamoto for useful comments and discussions. I also wish to thank all the members of theoretical astrophysics group at Kyoto University and Yukawa Institute for Theoretical Physics.

Appendix A

Path Integral Formula for the Wave Optics

We present the path integral formula which was developed by Nakamura & Deguchi (1999) to derive the diffraction integral.

A.1 Basic Wave Equation

We consider the scalar wave $\phi(t, \mathbf{r})$ propagating under the curved space-time due to the gravitational potential $U(\mathbf{r})$ of the lens objects (see also §2.1.1). The wave equation in the frequency domain is given in equation (2.7) as,

$$\left(\nabla^2 + \omega^2\right) \tilde{\phi} = 4\omega^2 U \tilde{\phi}. \tag{A.1}$$

where ω is the frequency.

We show the lensing configuration in Fig.A.1 for the source, the lens, and the observer. The source is located at the center of the coordinate system. r_l, r_o, and r_{lo} are distances to the lens, to the observer, and from the lens to the observer, respectively. We use the spherical coordinate system (r, θ, ϕ), then the observer is located at $\mathbf{r}_o = (r_o, \theta_o, \phi_o)$ with $\theta_o \ll 1$.

In the no lens limit ($U = 0$), the solution of the wave equation (A.1) is,

$$\tilde{\phi}_0 = A \frac{e^{i\omega r}}{r}, \tag{A.2}$$

where A is the amplitude. With the above equation (A.2) and the amplification factor F of the wave amplitude due to the lensing, the gravitationally lensed wave $\tilde{\phi}$ is written as,

$$\tilde{\phi}(\omega, \mathbf{r}) = F(\omega, \mathbf{r}) \frac{e^{i\omega r}}{r}. \tag{A.3}$$

Inserting this $\tilde{\phi}$ into the equation (A.1), we obtain,

$$\frac{\partial^2 F}{\partial r^2} + 2i\omega \frac{\partial F}{\partial r} + \frac{1}{r^2} \nabla_\theta^2 F = 4\omega^2 U F, \tag{A.4}$$

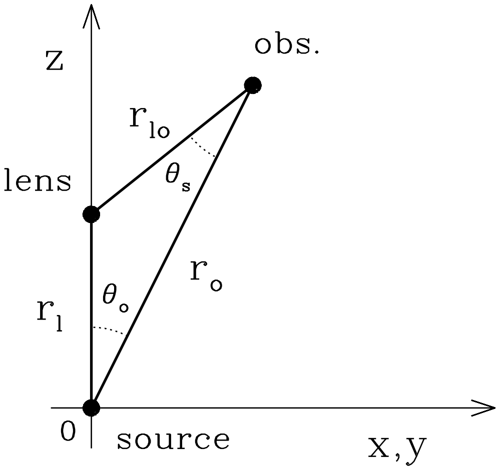

Figure A.1: Lensing configuration for the source, the lens, and the observer. r_l, r_o, and r_{lo} are the distances between them. The angles are very small: $\theta_o, \theta_s \ll 1$.

where

$$\nabla_\theta^2 = \frac{1}{\theta}\frac{1}{\partial\theta}\left(\theta\frac{1}{\partial\theta}\right) + \frac{\partial^2}{\partial\phi^2}.$$

We assume that the wave length $\sim 1/\omega$ is much smaller than the scale on which F varies, then we have $|\partial^2 F/\partial r^2| \ll |\omega\ \partial F/\partial r|$ and the first term in Eq.(A.4) is negligible. The equation (A.4) is rewritten as,

$$i\frac{\partial F}{\partial r} = -\frac{1}{2\omega r^2}\nabla_\theta^2 F + 2\omega U F \tag{A.5}$$

The above equation (A.5) is the same as the Schrödinger equation, if we consider r as the time, ωr^2 as the mass, $2\omega U$ as the potential, and F as the wave function.

A.2 Path Integral

The wave equation (A.5) can be solved by using the path integral (e.g. Sakurai 1994). From the analogy of Eq.(A.5) with the Schrödinger equation, the Lagrangian is given by,

$$L(r, \boldsymbol{\theta}, \dot{\boldsymbol{\theta}}) = \frac{1}{2}\omega r^2 |\dot{\boldsymbol{\theta}}|^2 - 2\omega U(r, \boldsymbol{\theta}) \tag{A.6}$$

where $\boldsymbol{\theta} = \theta(\cos\phi, \sin\phi)$ and $\dot{\boldsymbol{\theta}} = d\boldsymbol{\theta}/dr$. Then the solution of the wave equation (A.5) at the observer $\mathbf{r}_o$ is obtained with Eq.(A.6) as,

$$F(\omega, \mathbf{r}_o) = \int \mathcal{D}\boldsymbol{\theta}(r) \exp\left(i\int_0^{r_o} dr L\right). \tag{A.7}$$

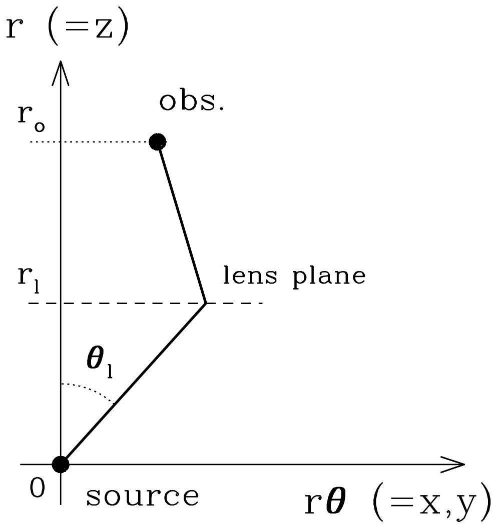

Figure A.2: The thick solid line is the path in the integration of Eq.(A.7). The dashed line is the lens plane on which the wave is scattered.

We assume the thin lens approximation in which the gravitational potential of the lens U does not vanish only on the lens plane. Then, the potential U is rewritten as,

$$U(r,\boldsymbol{\theta}) = \frac{1}{2}\delta(r-r_l)\hat{\psi}(\boldsymbol{\theta}), \tag{A.8}$$

where $\hat{\psi}$ is the deflection potential as defined in Eq.(2.14).

We calculate the integration in Eq.(A.7) along the path denoted the thick solid line from the source to the observer as shown in Fig.A.2. The wave is scattered only on the lens plane at $r = r_l$. We note that $\dot{\boldsymbol{\theta}}$ in the Lagrangian (A.6) corresponds to the slope of this thick solid line. Hence we obtain,

$$\begin{aligned} \dot{\boldsymbol{\theta}} &= 0, && \text{for } 0 \le r < r_l, \\ &= \frac{1}{r^2}\frac{r_l r_o}{r_{lo}}\left(\boldsymbol{\theta}_o - \boldsymbol{\theta}_l\right), && \text{for } r_l < r \le r_o. \end{aligned} \tag{A.9}$$

From Eqs.(A.6), (A.8) and (A.9), the integrand of Eq.(A.7) is written as,

$$\int_0^{r_o} drL = \omega\frac{r_l r_o}{2r_{lo}}\left|\boldsymbol{\theta}_l - \boldsymbol{\theta}_o\right|^2 - \omega\hat{\psi}. \tag{A.10}$$

Thus, the amplification factor F at the observer $\mathbf{r}_o$ is obtained from Eqs.(A.7) and (A.10) as,

$$F(\omega,\mathbf{r}_o) = \frac{\omega}{2\pi i}\frac{r_l r_o}{r_{lo}}\int d^2\boldsymbol{\theta}_l \exp\left[i\omega\left\{\frac{r_l r_o}{2r_{lo}}\left|\boldsymbol{\theta}_l - \boldsymbol{\theta}_o\right|^2 - \hat{\psi}(\boldsymbol{\theta}_l)\right\}\right], \tag{A.11}$$

where F is normalized such that $F = 1$ in the no-lens limit ($\hat{\psi} = 0$). The result (A.11) is coincident with the amplification factor in Eq.(2.19) which is derived by using the Kirchhoff diffraction integral.

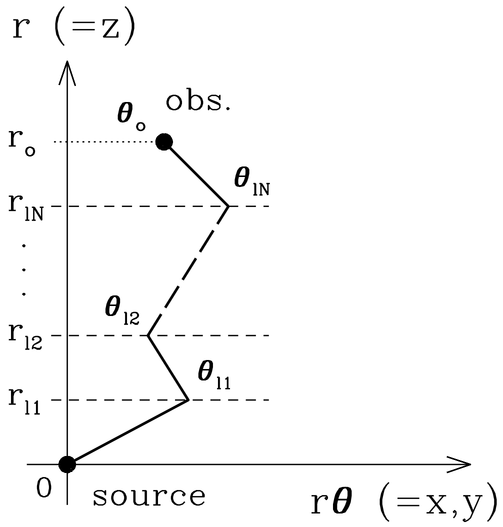
r (=z)
obs.
$\boldsymbol{\theta}_o$
r_o
$\boldsymbol{\theta}_{lN}$
r_{lN}
$\boldsymbol{\theta}_{l2}$
r_{l2}
$\boldsymbol{\theta}_{l1}$
r_{l1}
0
source
$r\boldsymbol{\theta}$ (=x,y)

Figure A.3: Same as Fig.A.2, but for the multi-lens system with N lens planes (dashed lines).

A.3 Application to Multi-Lens System

We present the application of the path integral formula to the multi-lens system which was developed by Yamamoto (2003). We consider N lens planes which are located at $r = r_{lj}$ $(j = 1, 2, \cdots, N)$ with the deflection potential $\hat{\psi}_j(\boldsymbol{\theta})$ (see Fig.A.3). Then, the gravitational potential U in Eq.(A.8) is rewritten as,

$$U(r, \boldsymbol{\theta}) = \frac{1}{2} \sum_{j=1}^{N} \delta(r - r_{lj}) \hat{\psi}_j(\boldsymbol{\theta}). \tag{A.12}$$

$\dot{\boldsymbol{\theta}}$ in Eq.(A.9) is also rewritten as,

$$\begin{aligned} \dot{\boldsymbol{\theta}} &= 0, && \text{for } 0 \le r < r_{l1}, \\ &= \frac{1}{r^2} \frac{r_{lj} r_{l(j+1)}}{r_{lj,l(j+1)}} \left(\boldsymbol{\theta}_{l(j+1)} - \boldsymbol{\theta}_{lj} \right), && \text{for } r_{lj} < r < r_{l(j+1)}, \\ &= \frac{1}{r^2} \frac{r_{lN} r_o}{r_{lN,o}} \left(\boldsymbol{\theta}_o - \boldsymbol{\theta}_{lN} \right), && \text{for } r_{lN} < r \le r_o, \end{aligned} \tag{A.13}$$

where $r_{lj,l(j+1)} = r_{l(j+1)} - r_{lj}$ for $j = 1, 2, \cdots, N-1$, and $r_{lN,o} = r_o - r_{lN}$. From above equations (A.12) and (A.13), the equation (A.10) is rewritten as,

$$\int_0^{r_o} dr L = \omega \left[\sum_{j=1}^{N-1} \frac{r_{lj} r_{l(j+1)}}{2 r_{lj,l(j+1)}} \left| \boldsymbol{\theta}_{l(j+1)} - \boldsymbol{\theta}_{lj} \right|^2 + \frac{r_{lN} r_o}{2 r_{lN,o}} \left| \boldsymbol{\theta}_o - \boldsymbol{\theta}_{lN} \right|^2 \right] - \omega \sum_{j=1}^{N} \hat{\psi}_j(\boldsymbol{\theta}_{lj}). \tag{A.14}$$

The amplification factor is obtained from Eqs.(A.7) and (A.14) as,

$$\begin{aligned}
F(\omega,\mathbf{r}_o) &= \frac{\omega}{2\pi i}\frac{r_{l1}r_{l2}}{r_{l1,l2}}\int d^2\boldsymbol{\theta}_{l1}\exp\left[i\omega\left\{\frac{r_{l1}r_{l2}}{2r_{l1,l2}}\left|\boldsymbol{\theta}_{l1}-\boldsymbol{\theta}_{l2}\right|^2-\hat{\psi}_1(\boldsymbol{\theta}_{l1})\right\}\right] \\
&\times \frac{\omega}{2\pi i}\frac{r_{l2}r_{l3}}{r_{l2,l3}}\int d^2\boldsymbol{\theta}_{l2}\exp\left[i\omega\left\{\frac{r_{l2}r_{l3}}{2r_{l2,l3}}\left|\boldsymbol{\theta}_{l2}-\boldsymbol{\theta}_{l3}\right|^2-\hat{\psi}_2(\boldsymbol{\theta}_{l2})\right\}\right] \\
&\qquad\vdots \\
&\times \frac{\omega}{2\pi i}\frac{r_{lN}r_o}{r_{lN,o}}\int d^2\boldsymbol{\theta}_{lN}\exp\left[i\omega\left\{\frac{r_{lN}r_o}{2r_{lN,o}}\left|\boldsymbol{\theta}_{lN}-\boldsymbol{\theta}_o\right|^2-\hat{\psi}_N(\boldsymbol{\theta}_{lN})\right\}\right],
\end{aligned}$$

where F is normalized such that $F=1$ in no lens limit ($\hat{\psi}_j=0$ for all j).

Appendix B

Numerical Computation for the Amplification Factor

We present the method for the numerical integration of the amplification factor F discussed in §2.1.3. The amplification factor is given in Eq.(2.26) as,

$$F(w,\mathbf{y}) = \frac{w}{2\pi i}\int d^2x \exp[iwT(\mathbf{x},\mathbf{y})], \tag{B.1}$$

where w is the frequency and $\mathbf{y}$ is the source position. The time delay T is given in Eq.(2.24) as,

$$T(\mathbf{x},\mathbf{y}) = \frac{1}{2}\left|\mathbf{x}-\mathbf{y}\right|^2 - \psi(\mathbf{x}) + \phi_m(\mathbf{y}), \tag{B.2}$$

where ψ is the deflection potential of the lens and ϕ_m is the additional phase in F. Since the integrand of F is rapidly oscillating function especially for large w, it is time consuming to numerically calculate F.

B.1 Axially Symmetric Lens Model

If the lens is axially symmetric, the potential $\psi(\mathbf{x})$ is a function of $x = |\mathbf{x}|$ and the amplification factor F is reduced to the simple form given in Eq.(2.27):

$$F(w,y) = -iwe^{iw[y^2/2+\phi_m(y)]}\int_0^\infty dx\ x\ J_0(wxy)e^{iw[x^2/2-\psi(x)]} \tag{B.3}$$

where J_0 is the Bessel function of zeroth order. Changing the integral variable from x to $z = x^2/2$ in the above equation (B.3), we obtain,

$$F(w,y) = \int_0^\infty dz f(z:w,y)\ e^{iwz} \tag{B.4}$$

where the function f is defined by,

$$f(z:w,y) \equiv -iwe^{iw[y^2/2+\phi_m(y)]}J_0(wy\sqrt{2z})e^{-iw\psi(\sqrt{2z})}. \tag{B.5}$$

Thus, we obtain the Fourier integral (B.4). We present the method for computing Fourier integral in Numerical Recipes (Press *et al.* 1992). The equation (B.4) is rewritten as,

$$\begin{aligned} F(w,y) &= \int_0^b dz f(z:w,y)\, e^{iwz} + \int_b^\infty dz f(z:w,y)\, e^{iwz}, \\ &= \int_0^b dz f(z:w,y)\, e^{iwz} - \frac{f(b:w,y)e^{iwb}}{iw} + \frac{f'(b:w,y)e^{iwb}}{(iw)^2} - \cdots, \end{aligned} \tag{B.6}$$

where $f' = \partial f/\partial b$. The first term of the above equation (B.6) is evaluated by numerical integration directly. For the series of the above equation, we use the integration by parts. Since $f(b:w,y) \propto b^{-1/4}$ for $b \gg 1$ from Eq.(B.5),[1] the asymptotic expansion in Eq.(B.6) converges for large b.

B.2 Non-axially Symmetric Lens Model

For the non-axially symmetric lens model, the amplification factor F in Eq.(B.1) is rewritten as,

$$F(w,\mathbf{y}) = \frac{w}{2\pi i}\, e^{iw[y^2/2+\phi_m(\mathbf{y})]} \int_0^\infty dx\; x\; e^{iwx^2/2} \int_0^{2\pi} d\theta\; e^{-iw[xy\cos\theta+\psi(x,\theta)]}, \tag{B.7}$$

where θ is defined as $\mathbf{x}\cdot\mathbf{y} = xy\cos\theta$. Similarly for the previous case, we use the integral variable $z = x^2/2$ in the above equation (B.7), we obtain,

$$F(w,\mathbf{y}) = \int_0^\infty dz f(z:w,\mathbf{y})\, e^{iwz} \tag{B.8}$$

where f is defined by,

$$f(z:w,\mathbf{y}) \equiv \frac{w}{2\pi i}\, e^{iw[y^2/2+\phi_m(\mathbf{y})]} \int_0^{2\pi} d\theta\; e^{-iw[y\sqrt{2z}\cos\theta+\psi(\sqrt{2z},\theta)]}. \tag{B.9}$$

Thus we can evaluate the above integral (B.8) using the method in the previous section.

---

[1] Note that $J_0(x) \propto x^{-1/2}$ for $x \gg 1$ (e.g. Abramowitz & Stegun 1970).

Appendix C

Asymptotic Expansion of the Amplification Factor for Non-axially Symmetric Lens Models

In §3.1, we considered the asymptotic expansion of the amplification factor F in powers of the inverse of the frequency $1/w$ for the axially symmetric lens model for simplicity. In this Appendix, we consider the expansion of F for the non-axially symmetric lens model.

In this case, the expansion of $T(\mathbf{x},\mathbf{y})$ around the j-th image position $\mathbf{x}_j$ in Eq.(2.29) is rewritten as,

$$T(\mathbf{x},\mathbf{y}) = T_j + \frac{1}{2}\sum_{a,b} T_{ab}\tilde{x}_a\tilde{x}_b + \mathcal{O}(\tilde{x}^3), \tag{C.1}$$

where $\tilde{\mathbf{x}} = \mathbf{x} - \mathbf{x}_j$, $T_j = T(\mathbf{x}_j,\mathbf{y})$, and $T_{ab} = \partial_a\partial_b T(\mathbf{x}_j,\mathbf{y})$ is a 2×2 matrix. We change the variable from $\tilde{x}_a$ to $z_a = \sum_b A_{ab}\tilde{x}_b$ in order to diagonalize the matrix T_{ab} in the above equation (C.1). Here, A_{ab} satisfies,

$$\sum_{a,b} T_{ab}A_{ac}A_{bd} = \lambda_c\delta_{cd}, \tag{C.2}$$

where λ_c is the eigenvalue of T_{ab}. Thus, the equation (C.1) is simply rewritten as,

$$T(\mathbf{x},\mathbf{y}) = T_j + \frac{1}{2}\left(\lambda_1 z_1^2 + \lambda_2 z_2^2\right) + \mathcal{O}(z^3). \tag{C.3}$$

The above result is similar to the equation (3.1) in the case of the axially symmetric lens. The magnification μ_j and the coefficient n_j in F_{geo} of equation (2.30) are also rewritten as, $\mu_j = 1/|\lambda_1\lambda_2|$ and $n_j = 1/2 - \mathrm{sign}(\lambda_1)/4 - \mathrm{sign}(\lambda_2)/4$.

We expand $T(\mathbf{x},\mathbf{y})$ in Eq.(C.1) up to the fourth order of $\tilde{x}$ as,

$$T(\mathbf{x},\mathbf{y}) = T_j + \frac{1}{2}\sum_{a,b} T_{ab}\tilde{x}_a\tilde{x}_b + \frac{1}{6}\sum_{a,b,c}\partial_a\partial_b\partial_c T(\mathbf{x}_j,\mathbf{y})\tilde{x}_a\tilde{x}_b\tilde{x}_c + \frac{1}{24}\sum_{a,b,c,d}\partial_a\partial_b\partial_c\partial_d T(\mathbf{x}_j,\mathbf{y})\tilde{x}_a\tilde{x}_b\tilde{x}_c\tilde{x}_d + \mathcal{O}(\tilde{x}^5). \tag{C.4}$$

Changing the variable $\tilde{x}_a$ to z_a, the above equation (C.4) is rewritten as,

$$T(\mathbf{x},\mathbf{y}) = T_j + \frac{1}{2}\left(\lambda_1 z_1^2 + \lambda_2 z_2^2\right) + \sum_{a,b,c} M_{abc}\; z_a z_b z_c + \sum_{a,b,c,d} N_{abcd}\; z_a z_b z_c z_d + \mathcal{O}(z^5), \tag{C.5}$$

where M_{abc} and N_{abcd} are defined by,

$$\begin{aligned} M_{abc} &= \frac{1}{6}\sum_{d,e,f}\partial_d\partial_e\partial_f T(\mathbf{x}_j,\mathbf{y})\; A_{ad}A_{be}A_{cf}, \\ N_{abcd} &= \frac{1}{24}\sum_{e,f,g,h}\partial_e\partial_f\partial_g\partial_h T(\mathbf{x}_j,\mathbf{y})\; A_{ae}A_{bf}A_{cg}A_{dh}. \end{aligned}$$

Inserting the above equation (C.5) to (2.26), we obtain,

$$F(w,\mathbf{y}) = \frac{1}{2\pi i}\sum_j e^{iwT_j}\int d^2z' \exp\left[i\left\{\frac{1}{2}\left(\lambda_1 z_1'^2 + \lambda_2 z_2'^2\right) + \frac{1}{\sqrt{w}}\sum_{a,b,c} M_{abc}\; z'_a z'_b z'_c + \frac{1}{w}\sum_{a,b,c,d} N_{abcd}\; z'_a z'_b z'_c z'_d + \mathcal{O}(w^{-3/2})\right\}\right], \tag{C.6}$$

where we change the integral variable from z_a to $z'_a = \sqrt{w}z_a$ and we use $d^2x = \det A\; d^2z = d^2z$. We expand the above equation (C.6) in powers of $1/w$ as,

$$F(w,y) = \frac{1}{2\pi i}\sum_j e^{iwT_j}\int d^2z' e^{i\left(\lambda_1 z_1'^2+\lambda_2 z_2'^2\right)/2}\left[1 + \frac{i}{\sqrt{w}}\sum_{a,b,c} M_{abc}\; z'_a z'_b z'_c + \frac{1}{w}\left\{-\frac{1}{2}\left(\sum_{a,b,c} M_{abc} z'_a z'_b z'_c\right)^2 + i\sum_{a,b,c,d} N_{abcd} z'_a z'_b z'_c z'_d\right\} + \mathcal{O}(w^{-3/2})\right]. \tag{C.7}$$

The first term of the above equation (C.7) is the amplification factor in the geometrical optics limit F_{geo} in equation (2.30). The integral in the second term vanishes because the integrand is an odd function of z'_a. The third term is the leading correction term, being proportional to $1/w$, arising from diffraction effect. Integrating the above equation (C.7), we obtain,

$$F(w,\mathbf{y}) = \sum_j |\mu_j|^{1/2} \left(1 + \frac{i}{w}\Delta_j\right) e^{iwT_j - i\pi n_j} + \mathcal{O}(w^{-2}), \tag{C.8}$$

where

$$\begin{aligned}\Delta_j \quad = \quad & \frac{15}{2}\left(\frac{M_{111}^2}{\lambda_1|\lambda_1|^2} + 3\frac{M_{111}M_{122}}{|\lambda_1|^2\lambda_2} + 3\frac{M_{112}M_{222}}{\lambda_1|\lambda_2|^2} + \frac{M_{222}^2}{\lambda_2|\lambda_2|^2}\right) \\ & - 3\left(\frac{N_{1111}}{|\lambda_1|^2} + 2\frac{N_{1122}}{\lambda_1\lambda_2} + \frac{N_{2222}}{|\lambda_2|^2}\right) \end{aligned} \tag{C.9}$$

and Δ_j is the real number.

Appendix D

Estimation Errors in the Geometrical Optics Limit

To evaluate the estimation errors $\Delta M_{Lz}, \Delta y$ in the geometrical optics limit, we consider the simple waveform

$$\tilde{h}^L(f) = \left(|\mu_+|^{1/2} - i \, |\mu_-|^{1/2} \, e^{2\pi i f \Delta t_d} \right) \times \tilde{h}(f), \tag{D.1}$$

where $\tilde{h} \propto \mathcal{A}$ is the unlensed signal and $\Delta t_d \propto M_{Lz}$, with three parameters $\gamma_i = (\ln M_{Lz}, y, \ln \mathcal{A})$. Then, the Fisher matrix $\Gamma_{ij} (i, j = 1, 2, 3)$ in Eq.(4.10) can be analytically obtained as,

$$\begin{aligned}
\Gamma_{11} &= (2\pi \Delta t_d)^2 \, |\mu_-| \;\; (f\tilde{h}|f\tilde{h}), \\
\Gamma_{12} &= 4\pi^2 \Delta t_d \frac{\partial \Delta t_d}{\partial y} \, |\mu_-| \;\; (f\tilde{h}|f\tilde{h}), \\
\Gamma_{13} &= 0, \\
\Gamma_{22} &= \left(2\pi \frac{\partial \Delta t_d}{\partial y} \right)^2 |\mu_-| \;\; (f\tilde{h}|f\tilde{h}) + \frac{1}{4} \left[\frac{1}{|\mu_+|} \left(\frac{\partial |\mu_+|}{\partial y} \right)^2 + \frac{1}{|\mu_-|} \left(\frac{\partial |\mu_-|}{\partial y} \right)^2 \right] \;\; (\tilde{h}|\tilde{h}), \\
\Gamma_{23} &= \frac{1}{2} \frac{\partial}{\partial y} \left(|\mu_+| + |\mu_-| \right) \;\; (\tilde{h}|\tilde{h}), \\
\Gamma_{33} &= \left(|\mu_+| + |\mu_-| \right) \;\; (\tilde{h}|\tilde{h}),
\end{aligned} \tag{D.2}$$

and $\Gamma_{ji} = \Gamma_{ij}$. $(\tilde{h}|\tilde{h})$ and $(f\tilde{h}|f\tilde{h})$ in the above equation (D.2) are,

$$\begin{aligned}
(\tilde{h}|\tilde{h}) = (S/N)^2 = 4 \int \frac{df}{Sn(f)} \; \left| \tilde{h}(f) \right|^2, \\
(f\tilde{h}|f\tilde{h}) = 4 \int \frac{df}{Sn(f)} \; \left| f\tilde{h}(f) \right|^2.
\end{aligned} \tag{D.3}$$

The S/N is the signal to noise ratio for the unlensed signal $\tilde{h}$. The estimation errors can be analytically obtained by the inverse of the Fisher matrix, $\Delta M_{Lz}/M_{Lz} =$

$[(\Gamma^{-1})_{11}]^{1/2}$ and $\Delta y/y = [(\Gamma^{-1})_{22}]^{1/2}/y$. Using the geometrical optics approximation, $f\Delta t_d \gg 1$, we obtain the errors with Eq.(D.2) and (D.3) as

$$\begin{aligned}\frac{\Delta M_{Lz}}{M_{Lz}} &= \frac{1}{S/N} \times \sqrt{\frac{|\mu_+| + |\mu_-|}{|\mu_+ \mu_-|}} \left| 2\frac{\partial}{\partial y} \ln \Delta t_d \Big/ \frac{\partial}{\partial y} \ln \left| \frac{\mu_+}{\mu_-} \right| \right|, \\ \frac{\Delta y}{y} &= \frac{1}{S/N} \times \sqrt{\frac{|\mu_+| + |\mu_-|}{|\mu_+ \mu_-|}} \left| 2 \Big/ y \frac{\partial}{\partial y} \ln \left| \frac{\mu_+}{\mu_-} \right| \right|. \end{aligned} \tag{D.4}$$

The above equations (D.4) are used for the general lens model when the double images form.

Estimation errors in the quasi-geometrical optics approximation

We evaluate the estimation errors in the quasi-geometrical optics approximation for the SIS lens. We take into account the effect of the diffracted image formed at lens center on the estimation errors. Then, the lensed waveform (D.1) is rewritten as,

$$\tilde{h}^L(f) = \left(|\mu_+|^{1/2} - i\,|\mu_-|^{1/2}\, e^{2\pi i f \Delta t_d} + \frac{\delta_c}{M_{Lz} f}\, e^{2\pi i f t_c} \right) \times \tilde{h}(f), \tag{D.5}$$

where $\mu_- = 0$ for $y > 1$. δ_c is defined as,

$$\begin{aligned}\delta_c &= \frac{i}{8\pi} \frac{1}{(1-y^2)^{3/2}} \quad \text{for } y < 1, \\ &= \frac{1}{8\pi} \frac{1}{(y^2-1)^{3/2}} \quad \text{for } y > 1,\end{aligned}$$

and $t_c = 2M_{Lz}(y+1)^2$ for the SIS lens (see §4.4.2). The third term in Eq.(D.5) corresponds to the diffracted image. The Fisher matrix $\Gamma_{ij}(i,j = 1,2,3)$ can be obtained similar to equations (D.2) as,

$$\begin{aligned}\Gamma_{11} &= (2\pi \Delta t_d)^2 |\mu_-|\ (f\tilde{h}|f\tilde{h}) + (2\pi)^2 |\delta_c|^2 \left(\frac{t_c}{M_{Lz}}\right)^2 (\tilde{h}|\tilde{h}) + \frac{|\delta_c|^2}{M_{Lz}^2} (f^{-1}\tilde{h}|f^{-1}\tilde{h}), \\ \Gamma_{12} &= 4\pi^2 \Delta t_d \frac{\partial \Delta t_d}{\partial y} |\mu_-|\ (f\tilde{h}|f\tilde{h}) + (2\pi|\delta_c|)^2 \frac{t_c}{M_{Lz}^2} \frac{\partial t_c}{\partial y} (\tilde{h}|\tilde{h}) \\ &\quad - \frac{\delta_c}{M_{Lz}^2} \frac{\partial \delta_c^*}{\partial y} (f^{-1}\tilde{h}|f^{-1}\tilde{h}), \\ \Gamma_{13} &= -\frac{|\delta_c|^2}{M_{Lz}^2} (f^{-1}\tilde{h}|f^{-1}\tilde{h}), \\ \Gamma_{22} &= \left(2\pi \frac{\partial \Delta t_d}{\partial y}\right)^2 |\mu_-|\ (f\tilde{h}|f\tilde{h}) + \frac{1}{4}\left[\frac{1}{|\mu_+|}\left(\frac{\partial |\mu_+|}{\partial y}\right)^2 + \frac{1}{|\mu_-|}\left(\frac{\partial |\mu_-|}{\partial y}\right)^2\right] (\tilde{h}|\tilde{h}) \\ &\quad + \left(2\pi \frac{|\delta_c|}{M_{Lz}} \frac{\partial t_c}{\partial y}\right)^2 (\tilde{h}|\tilde{h}) + \frac{1}{M_{Lz}^2} \left|\frac{\partial \delta_c}{\partial y}\right|^2 (f^{-1}\tilde{h}|f^{-1}\tilde{h}),\end{aligned}$$

$$\begin{aligned}
\Gamma_{23} &= \frac{1}{2}\frac{\partial}{\partial y}\left(|\mu_+|+|\mu_-|\right)\ (\tilde{h}|\tilde{h}) + \frac{\delta_c}{M_{Lz}^2}\frac{\partial \delta_c^*}{\partial y}\ (f^{-1}\tilde{h}|f^{-1}\tilde{h}), \\
\Gamma_{33} &= \left(|\mu_+|+|\mu_-|\right)\ (\tilde{h}|\tilde{h}) + \frac{|\delta_c|^2}{M_{Lz}^2}\ (f^{-1}\tilde{h}|f^{-1}\tilde{h}),
\end{aligned} \tag{D.6}$$

where $(f^{-1}\tilde{h}|f^{-1}\tilde{h})$ is defined as,

$$(f^{-1}\tilde{h}|f^{-1}\tilde{h}) = 4\int \frac{df}{Sn(f)}\ \left|f^{-1}\tilde{h}(f)\right|^2. \tag{D.7}$$

The estimation errors $\Delta M_{Lz}/M_{Lz} = [(\Gamma^{-1})_{11}]^{1/2}$ and $\Delta y/y = [(\Gamma^{-1})_{22}]^{1/2}/y$ are obtained from Eq.(D.6) as,

$$\begin{aligned}
\frac{\Delta M_{Lz}}{M_{Lz}} &= \frac{1}{S/N}\times\frac{2\left|\frac{\partial}{\partial y}\ln\Delta t_d\right|}{\left[\frac{|\mu_+\mu_-|}{|\mu_+|+|\mu_-|}\left(\frac{\partial}{\partial y}\ln\left|\frac{\mu_+}{\mu_-}\right|\right)^2 + 16\pi^2|\delta_c|^2\frac{t_c^2}{M_{Lz}^2}\left(\frac{\partial}{\partial y}\ln\left|\frac{t_c}{\Delta t_d}\right|\right)^2\right]^{1/2}}, \\
\frac{\Delta y}{y} &= \frac{1}{S/N}\times\frac{2/y}{\left[\frac{|\mu_+\mu_-|}{|\mu_+|+|\mu_-|}\left(\frac{\partial}{\partial y}\ln\left|\frac{\mu_+}{\mu_-}\right|\right)^2 + 16\pi^2|\delta_c|^2\frac{t_c^2}{M_{Lz}^2}\left(\frac{\partial}{\partial y}\ln\left|\frac{t_c}{\Delta t_d}\right|\right)^2\right]^{1/2}},
\end{aligned} \tag{D.8}$$

for $y < 1$. If we set $\delta_c = 0$, the results in Eq.(D.8) coincide with the previous results in Eq.(D.4). For $y > 1$, the errors is also obtained from Eq.(D.6) as,

$$\begin{aligned}
\frac{\Delta M_{Lz}}{M_{Lz}} &= \left|\frac{(\partial/\partial y)\ln t_c}{\delta_c(\partial/\partial y)\ln\left(t_c\delta_c/|\mu_+|^{1/2}\right)}\right| \times \frac{M_{Lz}^2}{(f^{-1}\tilde{h}|f^{-1}\tilde{h})}, \\
\frac{\Delta y}{y} &= \left|\frac{1}{\delta_c(\partial/\partial y)\ln\left(t_c\delta_c/|\mu_+|^{1/2}\right)}\right| \times \frac{M_{Lz}^2}{(f^{-1}\tilde{h}|f^{-1}\tilde{h})}.
\end{aligned} \tag{D.9}$$

Bibliography

Abramowitz, M. & Stegun, I.A., Handbook of Mathematical Functions, Dover Publications, New York, (1970).

Asada, H., A & A, **390**, L11, (2002).

Asada, H., Kasai, T. & Kasai, M., Prog. Theor. Phys., **108**, 1031, (2002).

Bartelmann, M., A & A, **313**, 697, (1996).

Baraldo, C., Hosoya, A. & Nakamura, T.T., Phys. Rev. D, **59**, 083001, (1999).

Bender, P.L. *et al.* , LISA: A Cornerstone Mission for the Observation of Gravitational Waves, System and Technology Study Report ESA-SCI(2000) 11, 2000.

Bliokh, P.V. & Minakov, A.A., Ap. Space Sci., **34**, L7, (1975).

Bontz, R.J. & Haugan, M.P., Ap. Space Sci., **78**, 199, (1981).

Born, M. & Wolf, E., Princeples of Optics (Cambridge University Press, Cambridge, England, 1997).

Bullock, J.S., *et al.* , MNRAS, **321**, 559, (2001).

Cutler, C. & Flanagan, E.F., Phys. Rev. D, **49**, 2658, (1994).

Cutler, C., Phys. Rev. D, **57**, 7089, (1998).

Cutler, C. & Thorne, K.S., in Early Universe and Cosmological Observations: A critical Review, ed. Dunsby, P., Ellis, G.F.R., & Maartens, R., (Bristol:IOP), 72, (2002).

Deguchi, S. & Watson, W.D., ApJ, **307**, 30, (1986).

Deguchi, S. & Watson, W.D., Phys. Rev. D, **34**, 1708, (1986).

De Paolis, F., Ingrosso, G., & Nucita, A.A., A & A, **366**, 1065, (2001).

De Paolis, F., *et al.* , A & A, **394**, 749, (2002).

Finn, L.S., Phys. Rev. D, **46**, 5236, (1992).

Finn, L.S., Phys. Rev. D, **53**, 2878, (1996).

Gradshteyn, I.S. & Ryzhik, I.M., Table of Integrals, Series, and Products, Academic Press, New York, (2000).

Haehnelt, M.G., MNRAS, **269**, 199, (1994).

Haehnelt, M.G., in AIP Conf. Proc. 456, Second International LISA Symposium on the Detection and Observation of Gravitational Waves in Space, ed. W. M. Folkner (New York: AIP), 45, (1998).

Hellings, R.W. & Moore, T.A., Class. Quant. Grav., **20**, 181, (2003).

Holz, D.E. & Hughes, S.A., astro-ph/0212218, (2002).

Hughes, S. A., MNRAS, **331**, 805, (2002).

Hughes, S. A., Annals Phys., **303**, 142, (2003).

Jaffe, A.H. & Backer, D.C., ApJ, **583**, 616, (2003).

Kalogera, V., *et al.* , ApJ, **556**, 340, (2001).

Kalogera, V., *et al.* , astro-ph/0312101, (2003).

Keeton, C.R., astro-ph/0102341, (2001).

Kline, M. & Kay, I.W., Electromagnetic Theory and Geometrical Optics, Interscience Publishers, New York, (1965).

Mandel, L. & Wolf, E., Optical coherence and quantum optics, Cambridge University Press, Cambridge, England, (1995).

Mandzhos, A.V., Soviet Astron. Lett., **7**, 213, (1981).

Menou, K., Haiman, Z., & Narayanan, V.K., ApJ, **558**, 535, (2001).

Misner, C.W., Thorne, K.S. & Wheeler, J.A., Gravitation, (Freeman, San Francisco 1973).

Moore, T.A. & Hellings, R.W., Phys. Rev. D **65**, 062001, (2002).

Nakamura, T.T., Phys. Rev. Lett., **80**, 1138, (1998).

Nakamura, T.T. & Deguchi, S., Prog. Theor. Phys. Suppl., **133**, 137, (1999).

Narayan, R. & White, S.D.M., MNRAS, **231**, 97, (1988).

Narayan, R., Piran, T, & Shemi, A., ApJ, **379**, L17, (1991).

Navarro, J.F., Frenk, C.S. & White, S.D.M., ApJ, **462**, 563, (1996).

Navarro, J.F., Frenk, C.S. & White, S.D.M., ApJ, **490**, 493, (1997).

Nemiroff, R.J., *et al.* , Phys. Rev. Lett., **86**, 580, (2001).

Ohanian, H.C., Int. J. Theor. Phys., **9**, 425, (1974).

Ohanian, H.C., ApJ, **271**, 551, (1983).

Peters, P.C., Phys. Rev., **136**, B1224, (1964).

Peters, P.C., Phys. Rev. D, **9**, 2207, (1974).

Peterson, J.B. & Falk, T., ApJ, **374**, L5, (1991).

Phinney, E.S., ApJ, **380**, L17, (1991).

Press, W.H. & Schechter, P., ApJ, **187**, 425, (1974).

Press, W.H. *et al.* , Numerical Recipes in Fortran 77 2nd ed., Cambridge Univ. Press, Cambridge, 1992.

Ruffa, A.A., ApJ, **517**, L31, (1999).

Sakurai, J.J., Modern Quantum Mechanics 2nd ed., Addison-Wesley, Reading Massachusetts, (1994).

Schneider, P. & Schmid-Burgk, J., A & A, **148**, 369, (1985).

Schneider, P. & Weiss, A., A & A, **164**, 237, (1986).

Schneider, P., Ehlers, J. & Falco, E.E., Gravitational Lenses, 1992, (New York : Springer).

Seto, N., Phys. Rev. D, **66**, 122001, (2002).

Seto, N., Kawamura, S. & Nakamura, T., Phys. Rev. Lett., **87**, 221103, (2001).

Seto, N., astro-ph/0305605, (2003).

Takahashi, R. & Nakamura, T., ApJ, **595**, 1039, (2003).

Thorne, K.S., in *Gravitational Radiation*, edited by Deruelle, N. & Piran, T., (North-Holland, Amsterdam), p28, (1983).

Thorne, K.S., in 300 Years of Gravitation, ed. Hawking, S.W. & Israel, W., (Cambridge: Cambridge Univ. Press), 697, (1987).

Turner, E.L., Ostriker, J.P. & Gott, J.R., ApJ, **284**, 1, (1984).

Varvella, M.A., Angonin, M.C., & Tourrenc, P., gr-qc/0312028, (2003).

Vecchio, A. & Cutler, C., in Folkner, W.M., editor, *Laser Interferometer Space Antenna, Second International LISA Symposium on the Detection and Observation of Gravitational Waves in Space*, AIP Conference Proceedings, Vol.456, p101, (1998).

Vecchio, A., astro-ph/0304051, (2003).

Wang, Y., Stebbins, A., & Turner, E.L., Phys. Lev. Lett., **77**, 2875, (1996).

Wilkinson, P.N., *et al.* , Phys. Rev. Lett., **86**, 584, (2001).

Wyithe, J.S.B. & Loeb, A., ApJ, **590**, 691, (2003).

Yamamoto, K., astro-ph/0309696, (2003).

Zakharov, A.F. & Baryshev, Y.V., Class. Quantum Grav., **19**, 1361, (2002).